


5-31-2022

Investigation of topological phonons in acoustic metamaterials

Wenting Cheng
New Jersey Institute of Technology

Follow this and additional works at: <https://digitalcommons.njit.edu/dissertations>

 Part of the [Acoustics, Dynamics, and Controls Commons](#), [Condensed Matter Physics Commons](#), and the [Engineering Science and Materials Commons](#)

Recommended Citation

Cheng, Wenting, "Investigation of topological phonons in acoustic metamaterials" (2022). *Dissertations*. 1597.

<https://digitalcommons.njit.edu/dissertations/1597>

This Dissertation is brought to you for free and open access by the Electronic Theses and Dissertations at Digital Commons @ NJIT. It has been accepted for inclusion in Dissertations by an authorized administrator of Digital Commons @ NJIT. For more information, please contact digitalcommons@njit.edu.

Copyright Warning & Restrictions

The copyright law of the United States (Title 17, United States Code) governs the making of photocopies or other reproductions of copyrighted material.

Under certain conditions specified in the law, libraries and archives are authorized to furnish a photocopy or other reproduction. One of these specified conditions is that the photocopy or reproduction is not to be “used for any purpose other than private study, scholarship, or research.” If a user makes a request for, or later uses, a photocopy or reproduction for purposes in excess of “fair use” that user may be liable for copyright infringement,

This institution reserves the right to refuse to accept a copying order if, in its judgment, fulfillment of the order would involve violation of copyright law.

Please Note: The author retains the copyright while the New Jersey Institute of Technology reserves the right to distribute this thesis or dissertation

Printing note: If you do not wish to print this page, then select “Pages from: first page # to: last page #” on the print dialog screen

The Van Houten library has removed some of the personal information and all signatures from the approval page and biographical sketches of theses and dissertations in order to protect the identity of NJIT graduates and faculty.

ABSTRACT

INVESTIGATION OF TOPOLOGICAL PHONONS IN ACOUSTIC METAMATERIALS

by
Wenting Cheng

Topological acoustics is a recent and intense area of research. It merges the knowledge of mathematical topology, condensed matter physics, and acoustics. At the same time, it has been pointed out that quasiperiodicity can greatly enhance the periodic table of topological systems. Because quasiperiodic patterns have an intrinsic global degree of freedom, which exists in the topological space called the hull of a pattern, where the shape traced in this topological space is called the phason. The hull augments the physical space, which opens a door to the physics of the integer quantum Hall effect (IQHE) in arbitrary dimensions. In this dissertation, acoustic metamaterials that exhibit two-dimensional (2D) and four-dimensional (4D) IQHE physics are demonstrated by laboratory implementation based on these ideas. In the second chapter, the acoustic waveguide generated by a simple quasiperiodic patterning exhibits topological edge modes and interface modes without any additional fine-tuning. In the third chapter, acoustic metamaterials generated by incommensurate bilayers present dynamic energy transfer in adiabatic cycles across the crystal via pumping of topological edge modes without any external intervention or assistance. In the fourth chapter, a re-configurable 2D quasiperiodic acoustic crystal with a phason living on a 2-torus displays 4D quantum Hall physics. The topological boundary spectrum assembles in a Weyl singularity when mapped as the function of the quasi-momenta. Topological wave steering enabled by the Weyl physics of the three-dimensional (3D) boundaries is also demonstrated experimentally. All acoustic systems mentioned previously are characterized experimentally by standard acoustic measurements, and via a finite element analysis utilizing COMSOL

Multiphysics. The experimental measurements and simulations reproduce the theoretical predictions with high fidelity.

**INVESTIGATION OF TOPOLOGICAL PHONONS IN ACOUSTIC
METAMATERIALS**

**by
Wenting Cheng**

**A Dissertation
Submitted to the Faculty of
New Jersey Institute of Technology
in Partial Fulfillment of the Requirements for the Degree of
Doctor of Philosophy in Materials Science and Engineering
Materials Science Option**

Interdisciplinary Program in Materials Science and Engineering

May 2022

Copyright © 2022 by Wenting Cheng

ALL RIGHTS RESERVED

APPROVAL PAGE

**INVESTIGATION OF TOPOLOGICAL PHONONS IN ACOUSTIC
METAMATERIALS**

Wenting Cheng

Dr. Camelia Prodan, Dissertation Advisor Date
Associate Professor of Physics, NJIT

Dr. John Federici, Committee Member Date
Distinguished Professor of Physics, NJIT

Dr. Keun Hyuk Ahn, Committee Member Date
Associate Professor of Physics, NJIT

Dr. Michael Siegel, Committee Member Date
Professor of Mathematical Sciences, NJIT

Dr. Smitha Vishveshwara, Committee Member Date
Professor of Physics, University of Illinois at Urbana-Champaign

BIOGRAPHICAL SKETCH

Author: Wenting Cheng
Degree: Doctor of Philosophy
Date: May 2022

Undergraduate and Graduate Education:

- Doctor of Philosophy in Materials Science and Engineering, New Jersey Institute of Technology, Newark, NJ, 2022
- Bachelor of Engineering in Materials Science and Engineering, North China Electric Power University, Beijing, China, 2017

Major: Materials Science and Engineering

Publications:

- Cheng, W., Prodan, E., & Prodan, C. (2022). Topological D-Class Physics with Passive Acoustic Elements. arXiv:2204.03613
- Cheng, W., Prodan, E., & Prodan, C. (2021). Revealing the Boundary Weyl Physics of the Four-Dimensional Hall Effect via Phason Engineering in Metamaterials. *Physical Review Applied*, 16(4), 225501.
- Cheng, W., Prodan, E., & Prodan, C. (2020). Experimental Demonstration of Dynamic Topological Pumping across Incommensurate Bilayered Acoustic Metamaterials. *Physical Review Letters*, 125(22), 224301.
- Apigo, D. J., Cheng, W., Dobiszewski, K. F., Prodan, E., & Prodan, C. (2019). Observation of Topological Edge Modes in a Quasiperiodic Acoustic Waveguide. *Physical Review Letters*, 122(9), 095501.

Presentations:

- Cheng, W. (2022, March 14-18). *Revealing the Boundary Weyl Physics of the Four-Dimensional Hall Effect via Phason Engineering in Metamaterials*. [Paper presentation]. American Physical Society March Meeting, Chicago, IL, United States.
- Cheng, W. (2021, September 20-25). *Experimental Demonstration of Dynamic Topological Pumping across Incommensurate Bilayered Acoustic Metamaterials*. [Paper presentation]. Metamaterials 2021 Conference, Virtual, United States.

- Cheng, W. (2021, March 15-19). *Experimental Demonstration of Dynamic Topological Pumping across Incommensurate Bilayered Acoustic Metamaterials*. [Paper presentation]. American Physical Society March Meeting, Virtual, United States.
- Cheng, W. (2020, December 4-6). *Experimental Demonstration of Dynamic Topological Pumping across Incommensurate Bilayered Acoustic Metamaterials*. [Paper presentation]. American Physical Society Mid-Atlantic Section Fall Meeting, Virtual, United States.
- Cheng, W. (2019, March 4-8). *Observation of Topological Edge Modes in a Quasiperiodic Acoustic Waveguide*. [Paper presentation]. American Physical Society March Meeting, Boston, MA, United States.

This dissertation is dedicated to my family and many friends who offered support and encouragement and have always been there for me.

ACKNOWLEDGMENT

Writing a significant scientific dissertation is hard work and it would be impossible without support of various people. First of all, I wish to express my sincere appreciation to my advisor, Prof. Camelia Prodan for the continuous support of my Ph.D. study and research. It has been an honor to be her Ph.D. student. Dr. Prodan convincingly guided and encouraged me to be professional and do the right things even when the road got tough. She has been very supportive and patient since the first days I began working on topological acoustic systems. She often pointed out the incompleteness of my work and assisted me in improving my understanding on each problem. I would like to thank her for all her contributions of time and ideas during my Ph.D. study.

I also want to thank Prof. Emil Prodan, who provided me the opportunities to do the collaboration work. He has wide knowledge and accurate physical intuition. Without his precious support and help, it would have been impossible to conduct my research projects.

I sincerely thank all of my committee members: Profs. John Federici, Keun Hyuk Ahn, Michael Siegel, and Smitha Vishveshwara, for their time to attend my final defense, and for their insightful comments and the hard questions which motivated me to widen my research from various perspectives. Additionally, I also want to thank Prof. Gordon Thomas, who was a member of my committee but retired in 2020, for being one of the kindest people I know.

I would like to thank the W. M. Keck Foundation, National Science Foundation grant DMR-1823800 for the financial support of my research and Research Assistant position and the Department of Physics for the financial support of my research and my Teaching Assistant position, respectively.

I would like to express my sincere gratitude to my colleague and friend, Dr. David J. Apigo, for his guidance and assistance at every stage in my Ph.D. study, and for teaching me how to conduct acoustic simulation and measurements and cleanroom nanofabrication.

I also want to thank Dr. Kyle Dobiszewski for his contributions of ideas in design of my experiments.

My time at New Jersey Institute of Technology was made enjoyable in large part due to many friends. I want to thank Ssu-Ying Chen for her encouragement and friendship. I am also grateful to Megan T. Sweeney, Orion Wilchinsky, Jonathan O'Buckley and Siying Wang for all the fun that we have had in the past five years.

Last but not the least, I would like to express my gratitude to my family, especially my parents, Weijun Cheng and Lihong Xu, for raising me and supporting me in all my pursuits unconditionally, and to my loving, encouraging, and supportive husband, Kai Qian, whose faithful company during my entire Ph.D. life is really appreciated.

TABLE OF CONTENTS

Chapter	Page
1 INTRODUCTION	1
1.1 Acoustic Metamaterials and the Analog of Topological Insulator	1
1.2 Dissertation Framework	7
2 OBSERVATION OF TOPOLOGICAL EDGE MODES IN A QUASI-PERIODIC ACOUSTIC WAVEGUIDE	13
2.1 Introduction	13
2.2 Construction of the Continuous Hull of the Waveguide	14
2.3 The Quasi-periodic Acoustic Waveguide Experimental Platform	17
2.4 Effect of Patterning	18
2.5 Experimental Results	19
2.5.1 Experimental Protocol	19
2.5.2 Bulk Spectrum and Measurement	20
2.5.3 Topological Edge Spectrum and Measurement	21
2.5.4 Topological Interface Mode Measurement	23
2.6 Summary	24
3 EXPERIMENTAL DEMONSTRATION OF TOPOLOGICAL PUMPING ACROSS INCOMMENSURATE BILAYERED ACOUSTIC METAMATERIALS	26
3.1 Introduction	26
3.2 Computing the Phason Space	30
3.3 Origin of the Topological Gaps	32
3.4 Coupled Incommensurate Chains Experimental Platform	34
3.4.1 Numerical Simulations	34
3.4.2 Fabrication	34
3.4.3 Experimental Protocols	35
3.5 Experimental Results	36
3.5.1 The Numerically Simulated Topological Pumping Process	36

TABLE OF CONTENTS
(Continued)

Chapter	Page
3.5.2 Un-assisted Dynamical Energy Pumping via Topological Edge Modes	37
3.5.3 Experimental Mapping of the Bulk and Edge Resonant Spectrum . . .	38
3.5.4 Dynamical Pumping additional experiments	40
3.5.5 Topological Edge Spectrum under Full Phason Cycle	42
3.6 Summary	43
4 REVEALING THE WEYL PHYSICS OF THE FOUR-DIMENSIONAL HALL EFFECT VIA PHASON ENGINEERING IN METAMATERIALS	44
4.1 Introduction	44
4.2 Experimental Set-up and Results	47
4.3 Methods	58
4.3.1 Fabrication	58
4.3.2 Experimental Protocols	58
4.4 Simulation	60
4.5 Phason Engineering	60
4.6 QHE via Phason Engineering	63
4.7 Visualizing the Topological Invariants	66
4.8 Summary	72
5 SUMMARY	74
REFERENCES	78

LIST OF FIGURES

Figure	Page
<p>1.1 Energy spectrum of topological insulator. <i>Source: [Qi and Zhang, 2011]</i></p>	3
<p>1.2 (a) Schematic of the hexagonal lattice. The blue and grey spheres represent concentrated masses $m_1 = m_2$. The red and black straight rods represent massless linear springs with stiffness k_1 and $k_2 = k_1/20$. The dashed cell is the primitive cell of the lattice. (b) Schematic of the square lattice. The blue and grey spheres represent concentrated masses $m_1 = m_2$. The black and red straight rods represent massless linear springs with stiffness k_1 and $k_2 = 2k_1$. (c) Band structure of the hexagonal lattice in (a) showing bulk bands (black dots) and edge bands (colored lines). Red solid lines represent edge modes bound to the top boundary, while blue dashed lines represent edge modes bound to the bottom boundary. (d) Band structure of the square lattice in (b) showing bulk bands (black dots) and two topological edge bands (red solid lines) bound to the top boundary. <i>Source: [Wang et al., 2009]</i></p>	8
<p>1.3 (a) A pattern consist of a finite number of points generated by the algorithm $x_n = nl_0 + r \sin(n\theta)$, with the particular values $l_0 = 1$, $r = 0.4$ and $\theta = \frac{2\pi}{\sqrt{15}}$. (b) A geometric algorithm to generate the same pattern.(c) Bulk spectrum as function of parameter θ. <i>Source: [Apigo et al., 2018]</i></p>	9
<p>1.4 Experimental observation of static adiabatic pumping (a) An illustration of the adiabatically modulated photonic quasicrystal, constructed by slowly varying the spacing between the waveguides along the propagation axis z. (b) The specthm of the model as a function of the adiabatic parameter ϕ. (c) The measured intensity distributions as a function of the position are presented at different propagation distance of the adiabatic evolution. It is evident that along the adiabatic evolution the light crossed the lattice from right to left. <i>Source: [Kraus et al., 2012]</i></p>	10

**LIST OF FIGURES
(Continued)**

Figure	Page
<p>1.5 (a) Unit-cell of the magneto-mechanical system, comprises of two mechanical resonators that are coupled through magnetic interaction. Angular rotation ϕ of the modulation shaft simultaneously induces coupling modulation (CM) and on-site potential modulations (OPM). CM is generated with an off-axis high-permeability metal alloy sheet while OPM utilizes permanent magnets. (b) All experiments use an array of four unit-cells. Rotation of the shaft is motorized, though in principle a crank handle (illustrated) could be used to activate the pump. (c) Calculated band-structure for an array composed of 100 sites, as a function of the pump phase ϕ. EMU and EML are the upper and lower trajectories over which the two edge modes evolve during the pump cycle. At $\phi = 0, 2\pi$ the system is in the topologically non-trivial phase while at $\phi = \pi$ the system is in the topologically trivial phase pump. (d) The measured and simulated band structure. <i>Source: [Grinberg et al., 2020]</i></p>	11
<p>2.1 The virtual manifold associated to the patterned waveguide is a 2-torus.</p>	15
<p>2.2 Top: photograph of the waveguide configuration used to measure topological interface modes. Bottom: Cross-section and geometrical parameters. The waveguide consists of interlocking 3D printed PLA parts as shown in the insert and it is mirrored relative to the domain wall indicated by the dashed line. For experimentation, a speaker is placed at portholes accessible in each chamber and a piezoelectric microphone is inserted into an opposite porthole. The portholes that are not in use are sealed. The lengths L_n were generated with Equation (2.1) and their average was fixed at $L_{\text{avg}} = 40$ mm. The parameters in Equation (2.1) were fixed at $\Delta L = 0.2L_{\text{avg}}$ and $\theta = \frac{2\pi}{\sqrt{117}}$. This particular irrational fraction of 2π accepts a good rational approximation $\theta = \frac{9\pi}{48} + \mathcal{O}(10^{-3})$, which was used in some of the numerical calculations. The system was also run without a domain wall, for bulk and edge measurements.</p>	17
<p>2.3 (a) Dispersion of the acoustic modes for the un-patterned waveguide, for $m = 0$ sector. (b) The band structure of a periodically patterned waveguide (<i>i.e.</i> $\theta = 0$), for $m = 0$ sector. (c,d) Resonant spectrum of a patterned waveguide as function of θ, for $m = 0, 1$ sectors, respectively.</p>	18
<p>2.4 Bulk resonant spectrum for the geometry described in Figure 2.2. Left: Theoretical resonant spectrum reproduced from Figure 2.3(c), with arrows indicating the topological gaps. The vertical marking identifies $\theta = \frac{2\pi}{\sqrt{117}}$, used in experiments. Center: Normalized microphone readings from the center of 48 chambers, recorded over a wide frequency interval. Right: Collapse on the frequency axis of the intensity plot reported in the mid panel. Three spectral gaps can be clearly identified in the experimental data and seen to be well aligned with the theoretical calculations. The values of the Chern numbers for the two topological gaps are also indicated. .</p>	20

**LIST OF FIGURES
(Continued)**

Figure	Page
<p>2.5 Topological edge spectrum. (a) Theoretical prediction of the spectral flow against the phason parameter ϕ, demonstrating the existence of chiral bands. The red/blue marks relate to the left/right edge of the waveguide, respectively. (b) Experimental mapping of the spectral flow, confirming the existence of chiral bands. (c) The measurements for bulk spectrum, reproduced from Figure 2.4, indicating the position of the bulk gap edges.</p>	22
<p>2.6 (a) Topological interface mode, measured for a waveguide configuration similar to that in Figure 2.2. The spatial localization of the interface mode was mapped by moving the speaker and microphone away from the domain wall. (b) The topological interface mode is also observed in COMSOL simulations. Red, blue and green colors represent high, low and zero pressure variations, respectively.</p>	23
<p>3.1 (a) Photograph of a fully assembled acoustic bilayer consisting of top/bottom periodic arrays of cylindrical acoustic resonators with incommensurate lattice constants. The labels S_i and M_i indicate the positioning of the speaker and microphone during various experiments referenced in the text. The middle red bar indicates the presence of an inner chamber, which connects the top and bottom resonators and is referred to as the spacer. For dynamical pumping, additional resonators are mounted on the top left side. (b) Photograph of the inner structure, with the spacer now fully visible. (c) Cross-section showing only the domain of wave propagation, together with relevant parameters. Note that the very left resonator is completely decoupled from the main structure. (d) Bulk resonant spectrum as function of top-bottom relative alignment, when the top and bottom lattice constants are equal. In this case, all spectral gaps are trivial. (e) Bulk resonant spectrum as function of d_2/d_1. In this case, additional gaps open in the spectrum, which are all topological. (f) Schematic of the pumping process as well as a simulation of the air pressure at the beginning of the pumping cycle. (g) Microphone reading when the source frequency is adjusted in a topological gap. (h) Microphone reading when the source frequency is adjusted in a non-topological gap.</p>	29
<p>3.2 Phason Space consists of steps of length θ on the smooth and non self-intersecting loop shown on the left. The right diagram shows a view from the top.</p>	31
<p>3.3 Elementary resonant modes.</p>	32

LIST OF FIGURES
(Continued)

Figure	Page
3.4 (a) The configuration of the system at the beginning of a pumping cycle. The top array is uniformly displaced to the right and, after a total displacement d_2 , the system returns in its original configuration and completes a full pumping cycle. A speaker is inserted in resonator S1 and is kept on at all times, while a microphone is inserted in the resonator M0. (b) Simulation of the resonant spectrum as function of displacement. Chiral left and right edge bands are observed, which both connect two disjoint parts of the bulk spectrum. (c-h) Rendering of pumping mechanism: The left edge mode is loaded when the source frequency matches the mode frequency (c); The mode self-oscillates while its frequency is pushed up (d); The character of the mode changes from left-localized to delocalized (e); The character of the mode changes again from delocalized to right-localized (f); The mode self-oscillates as its frequency is pushed down (g); The cycle repeats itself as the top array is further pushed to the right (h). The microphone starts to pick signal after the event (e). The simulations in panels (c-h) show the spatial profile of the resonant mode highlighted in the sub-panel below it. The shown microphone outputs are not from real measurements. The pumping parameter is φ in all panels.	36
3.5 (a) Simulated resonant spectrum reproduced from Figure 3.1(e), with arrows indicating the topological gaps. The vertical marking identifies $d_1 = 20$ mm and $d_2 = 16$ mm used in experiments. (b) Measurement of the spaced-resolved density of states. (c) Collapse of the data in panel (b) on the frequency axis. Two spectral gaps can be clearly identified in the experimental data, which are well aligned with the theoretical calculations.	38
3.6 (a) Simulated resonant spectrum for the finite acoustic meta-crystal shown in Figure 3.1(a), as function of the pumping parameter. The latter is the ratio between the displacement x , shown in Figure 3.1(c), and d_2 . (b) Experimental measurement of the resonant spectrum as function of the pumping parameter. (c) Bulk-spectrum measurements reproduced from Figure 3.5(c), used here to pin-point the position of the bulk bands shown by dashed lines.	39
3.7 Adjusting the number of cycles same as Figure 3.1(g) but with 4, 6 and 10 added resonators.	40
3.8 Adjusting the pumping cycle speed same as Figure 3.1(g) but for different duration of the total ten cycles.	41
3.9 Adjusting the length of the meta-crystal same as Figure 3.8 but for a longer meta-crystal which contains five additional resonators at the top and four additional resonators at the bottom.	41
3.10 Full pumping cycle.	42
3.11 (a-c) Same as Figure 3.6 but this time with the phason driven over its full space Ω	43

**LIST OF FIGURES
(Continued)**

Figure	Page
<p>4.1 (a) Photograph of a fully assembled acoustic 2D sinusoidal pattern consisting of top/bottom cylindrical resonators. The middle red bar indicates the presence of an inner chamber, which connects the top and bottom resonators and is referred to as the spacer. (b) Photograph of the inner structure, with the spacer now fully visible. (c) The wave propagation domain. (d) Illustration of the algorithm which supplies the position of the resonators. (e) COMSOL simulated bulk resonant spectrum against θ, together with labels for the topological and non-topological gaps. (f) Left: COMSOL simulated resonant spectrum for hard wall termination, shown against the phason parameters ϕ_1 and ϕ_2. The Weyl singularity is the spectral surface connecting the the indicated bulk bands. Right: Experimental measurement of the density of states, with the phason space sampled in several directions. (g,h) Comparison between the experimentally measured density of states and the simulated spectrum (blue dots) for the traces $\phi_1 = 0.5$ and $\phi_1 = \phi_2$, respectively. The theoretical spectra have been stretched by a small factor to overlay the experimental data. The bright dispersive modes in the left side are part of the spectral dome. The right side displays the raw density of states data for the bulk, from where we read the edges of the bulk gap.</p>	48
<p>4.2 Square root of the spectrum of the dynamical matrix Equation (4.2) with (a) $\Lambda = 3D/4$, (b) $\Lambda = D/5$, and (c) $\Lambda = D/3$. The spectrum in panel (c) reproduces qualitatively the resonant spectrum of the experimental crystal.</p>	50
<p>4.3 (a) COMSOL simulated resonant spectrum for the experimental set-up from Figure 4.1, with arrows indicating the topological gaps. The vertical box identifies $\theta = 0.25$, used in experiments. (b) Measured local density of states, assembled from microphone readings on 42 bulk resonators. (c) Collapse on the frequency axis of the intensity plot reported in panel (b). Two spectral gaps can be clearly identified and seen to be well aligned with the theoretical predictions.</p>	51
<p>4.4 Profiles of the edge and corner modes for $\phi_x = \phi_y = 3/16$. (a) Comsol simulation shows the pressure distribution of a corner mode. (b)-(c) Comsol simulation shows the pressure distribution for 2 edge modes. (d) Experimental verification of the corner mode in (a), (e) Experimental verification of the 2 edge modes in (b)-(c).</p>	52
<p>4.5 Weyl singularity and mode steering. (a) COMSOL simulated spectrum as function of the phason $\phi = (\phi_1, \phi_2)$, revealing the Weyl singularity. (b) Cross-section of the Weyl singularity at 5910 Hz. (c) Acoustic pressure field distribution for the eight phasons marked in panel (b), revealing circular mode steering around the crystal's boundary.</p>	53

LIST OF FIGURES
(Continued)

Figure	Page
<p>4.6 Comsol simulations of corner to corner pumping. (a) Evolution of the resonant spectrum inside the topological bulk gap along the trajectory $\phi_x = \phi_y$, with the modes localized along an edge and in a corner modes separated out; (b) Experimentally measured bulk response shown as a reference for revealing the upper and lower bulk bands for the gap in panel (a); (c) Pressure distribution of modes (1)-(5) from panel (a), revealing corner-to-corner pumping via the bulk. . .</p>	56
<p>4.7 Stability of the spectral dome. (a) A crystal cut as a square and (b) its resonant energy spectrum. (c) A crystal cut as an octagon and (d) its resonant energy spectrum. In both cases, the spectra have been resolved by ϕ_1 and ϕ_2 and a spectral dome can be clearly identified. The spectra were computed with the model (c) from Figure 4.8.</p>	57
<p>4.8 Panels (a)-(c) correspond to the patterns in Figure 4.9(a)-(c), respectively. The spectra were computed with the model dynamical matrix $D_{\mathbb{P}} = \sum_{\mathbf{x}, \mathbf{y} \in \mathbb{P}} e^{-1.5 \mathbf{x}-\mathbf{y} ^2} \mathbf{x}\rangle\langle\mathbf{y}$, with the distance measured in units of D. The marked spectral gaps are related to bulk spectral gaps mapped in the experiments.</p>	61
<p>4.9 Dynamically generated patterns. (a) Same as the pattern of resonators in Figure 4.1 but with the simplified $F(\phi) = \epsilon D(\sin(2\pi\phi_1), \sin(2\pi\phi_2))$. (b) Same as (a) but with the lattice \mathbb{L}' rotated by 45° relative to \mathbb{L}. (c) Same as a but with F replaced by $G \circ F$ with $G(x, y) = (x + y, y - x)$. All three patterns were generated with $\theta = 1/2\sqrt{2}$.</p>	61
<p>4.10 Visualizing the topological invariants. a, b, c Integrated density of states (IDS) as computed from the spectra in Figure 4.8(a,b,c), respectively. The IDS values inside the spectral gaps can be identified by the abrupt changes in color. d, e, f Fittings of the IDS values inside the spectral gaps, seen in panels a, b, c, with Equation (4.29). Each curve is determined by the six topological invariants associated to each spectral gaps. The marked curves correspond to the marked gaps in Figure 4.8 and they can be fitted with $1 - \theta^2$, indicating $n_{\{1,2,3,4\}} = -1$, hence a 2nd Chern number -1. .</p>	65

CHAPTER 1

INTRODUCTION

1.1 Acoustic Metamaterials and the Analog of Topological Insulator

Acoustic metamaterials are fabricated structures with novel properties arising from their macroscopic design. Through the deliberate design of the material structure, the sound wave is purposefully controlled and modulated when passing through such materials, so as to obtain macroscopic material parameters that are not easy to obtain in conventional materials. For example, the sound absorption frequency of the material can be controlled within a specific range by designing the structure of the acoustic resonator [Yang et al., 2017]. And acoustic diode can rectify sound waves like current flow of electrical diode [Liang et al., 2009]. There are other research directions of acoustic metamaterials including acoustic focusing [Al Jahdali and Wu, 2016], acoustic imaging [Zhu et al., 2011], acoustic tweezers [Shi et al., 2009], etc. Our research focuses on a relatively new application of acoustic metamaterials, namely topological acoustic metamaterials. It is the acoustic analog of topological materials in condensed matter physics. The major interest in topological acoustic metamaterials based on ingenious design in acoustic metamaterials to investigate those topological phenomena that are difficult to observe in mathematics or condensed matter physics. Another field application is came from the new ways of conveying energy through topological waveguides or binding wave states to topological defects. Acoustic Metamaterials are a perfect playground to test and study these properties.

The purpose of studying the topological properties of materials is to find an intrinsic invariant property that is not disturbed by external forces. This immutability is very valuable in practical applications. Because there is no truly perfect crystal in reality, no matter how pure the crystal is, there will be impurities and the periodicity of the crystal lattice will also be disturbed. In many cases, in order to make the material have certain characteristics, it

is necessary to destroy its lattice periodicity to a certain extent, and doping is necessary at this time. If this intrinsic invariant property is embodied in the energy band spectrum, it can be mathematically described by topological invariants. There are many ways to define topological invariants, the most commonly used is Chern number.

The most common way to calculate the Chern number is by calculating the Berry phase.

$$\vec{\mathcal{A}}_n = i\langle\phi_{nk}|\nabla_{\vec{k}}|\phi_{nk}\rangle \quad (1.1)$$

\mathcal{A}_n is called Berry connection, and its curl is called Berry curvature Ω_n . From Green's theorem and Stokes' theorem, the closed loop integral of the Berry connection is equivalent to the area integral of the Berry curvature, which is Berry phase [Bernevig, 2013]. These two quantities are the description of the geometric structure and characteristics of the object. One can take the famous Foucault pendulum as an example. A simple pendulum should swing in the same plane, but due to the curvature of the ground and the rotation of the earth, this plane rotates slowly. This rotation angle is an example of Berry phase, which can reflect the geometric properties of the space, in which the pendulum is located. In the energy band problem, the Berry phase of each energy level is given by the specific expression of the energy level according to the above theorem.

$$\text{Ch} = \frac{1}{(2\pi)} \oint_P \vec{\mathcal{A}}_n d\lambda \quad (1.2)$$

According to Chern theorem, the integral of the Berry connection over a closed curve line is always equal to $2\pi\text{Ch}$, where Ch is an integer, which characterizes the topological properties of the energy bands. As you may have heard, the study of topology is counting the "number of holes". Structures with the same number of holes are considered to have the same properties (or "homeomorphism" in professional terms). For example, coffee cups

and doughnuts have only one hole. Therefore, they are the same from a topological point of view. It can be understood as to how many "holes" are in the band structure. Although we can't see it intuitively, we know that the number of holes must be an integer. The Chern number here does not change due to small changes in the energy band. If the Chern number of a certain energy band is zero, it is called topologically trivial, and if the Chern number is not zero, it is called topologically nontrivial. The topologically nontrivial energy band structure will produce relatively special material properties at a macroscopic level, and this property has strong stability due to its connection with the topological structure and is not affected by impurities and the macroscopic shape of the material.

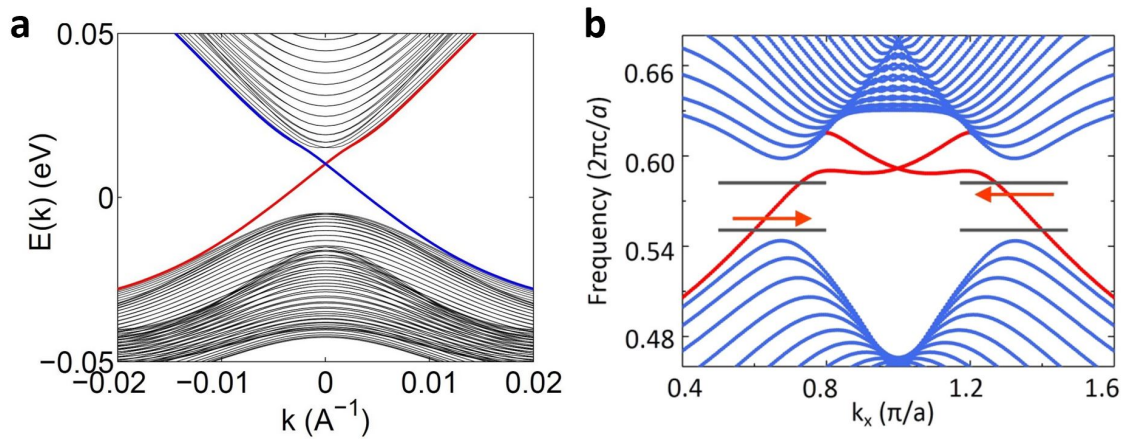


Figure 1.1 Energy spectrum of topological insulator.
Source: [Qi and Zhang, 2011]

Topological insulators are a kind of material with topologically nontrivial band structures, discovered by Shou-cheng Zhang [Qi et al., 2008] and others in quantum wells composed of HgTe and CdTe. A major feature of a topological insulator is that its internal energy band is topologically trivial, consistent with ordinary insulators, and there is a topologically non-trivial energy band structure on its surface. The reason for this difference is that the boundary of the crystal cuts off the periodic potential of the electron. Combine these two energy bands together as shown in Figure 1.1: The black energy bands indicate the energy inside the materials. The electrons completely fill the valence band below, which obviously is an insulator. The blue and red bands are the energy bands on the boundary,

or edge states [Qi and Zhang, 2011]. We notice that these two energy bands connect the conduction band and the valence band, and the electrons occupying these two energy levels can be easily accelerated by the external electric field to generate a macroscopic current. Therefore, the surface of the topological insulator is a conductor. Moreover, due to the dispersion of the boundary state, the direction of the momentum obtained by the electron after being accelerated is limited, which causes unidirectional conductivity in the two-dimensional case. This is the magic of topological insulators. Again, this boundary state is very stable and will not be affected by impurities due to topological protection.

If we introduce such topological properties to acoustic systems, then we can get topological acoustic metamaterials. The principle of topological acoustic metamaterials is simple: the wave equation of the acoustic wave as shown in Equation (1.3) and the stationary Schrödinger equation of the electronic wave are both second-order linear partial differential equations:

$$[(\nabla - i\vec{A}_{eff})^2 + V(x, y)]\Psi = 0. \quad (1.3)$$

In Equation 1.3, \vec{A}_{eff} represents the effective vector potential and $V(x, y)$ represents the scalar potential [Yang et al., 2015]:

$$\vec{A}_{eff} = \frac{\omega \vec{v}_0(x, y)}{c^2}, \quad (1.4)$$

$$V(x, y) = \frac{-1}{4} |\nabla \ln \rho|^2 - \frac{1}{2} \ln \rho + \frac{\omega^2}{c^2}. \quad (1.5)$$

As one can see, Equation (1.3) maps onto the Schrödinger equation for a spinless charged quantum particle in nonuniform vector and scalar potentials [Yang et al., 2015]. Since we can calculate the energy band of electrons in the periodic potential field, we can also define something similar for sound waves. At this time, what is used as the "periodic potential field" is the predesigned metamaterial. The energy spectrum calculated as shown in Figure 1.1 is very similar to the real topological insulator mentioned earlier.

However, in aperiodic systems, K-Theory is one of the best tools for establishing bulk boundary correspondences, such as quasi-periodic systems. For example, if we have an aperiodic pattern, we collect all the distances between the near neighbor points and project this data as coordinates into an infinite-dimensional space R^∞ space. In this case, we treat the pattern as a point in a topological space. Then, if we rigidly shift the pattern and project into the R^∞ space, it leads to a process: as the point starts to move under rigidly shifting, it traces a shape $C(\Xi)$ in the R^∞ space. If we normalize the maximum distance between near-neighbor points to 1, this shape, together with the action of rigidly shifting form a dynamical system inside an infinite cube of side length 1, is called the hull of the pattern. Here we define the shape traced by this process as the phason.

According to the fact that any commutative C^* -algebra is isomorphic to the algebra of continuous functions over a topological space. The algebra \mathcal{A} which is the C^* -algebra generated by commuting diagonal operators T_f and shift operator is isomorphic to the algebra of continuous functions over the hull of the pattern $C(\Xi)$. The algebra of commuting diagonal operators T_f as shown in Equation (1.6), where f is defined over the topological space.

$$T_f = \sum_n f(\tau_n P) |n\rangle \langle n|, \quad (1.6)$$

The algebra of physical observables reads:

$$\mathcal{A} = C^*(u, C^{(\Xi)}), \quad (1.7)$$

where u is the unitary operator. $C^{(\Xi)}$ is generated by the function:

$$v(x) = e^{i2\pi x}. \quad (1.8)$$

Then if we take the Fourier decomposition, we can see \mathcal{A} is the non-commutative 2-torus

$$v_i u_j = e^{i2\pi\theta_{i,j}} u_j v_i \quad (1.9)$$

$$\theta_{i,j} = -\theta_{j,i}, \quad (1.10)$$

The equivalent class of a projection (supposing we use the gap projection) P_G is usually denoted by $[P_G]_0$:

$$[P_G]_0 = P'_G \in \mathcal{M}_\infty \otimes \mathcal{A}, P'_G \sim P_G, \quad (1.11)$$

for any gap projection P_G from $\mathcal{M}_\infty \otimes \mathcal{A}$, one has

$$[P_G]_0 = \sum_j c_j [e_j]_0, c_j \in \mathbb{Z}. \quad (1.12)$$

The coefficient c_j represents all independent numerical invariants associated with the projection P_G , which defines a class $[P_G]_0 \in K_0$. Every gap can be uniquely labeled by a set of such coefficients c_j . If \mathcal{A} is equipped with a normalized trace \mathcal{T} , then the relation:

$$\mathcal{T}[P_G]_0 = \sum_j c_j \mathcal{T}[e_j]_0 \quad (1.13)$$

gives a homomorphism between K_0 and a countable sub-group of the real axis. Since every gap is uniquely labeled by an element of the K_0 group, when we look at a spectrum, we see the image of the K_0 group. The values of the Chern number on the K_0 group can be solved using the Equation (1.14). The result would be an integer.

$$\text{Ch}(P_G) = \frac{1}{(2i\pi)} \mathcal{T}\left(P_G[\partial_1 P_G, \partial_2 P_G]\right) \quad (1.14)$$

This K-theory method will be used in the following chapters of this dissertation to characterize the topological properties of the energy bands of the acoustic systems.

1.2 Dissertation Framework

In this dissertation, we first experimentally investigated the topological properties of two 1D acoustic systems, in which the topological edge modes and Thouless pumping were realized by quasiperiodic patterning. Then we studied the topological phenomena in a 2D acoustic system. The boundary Weyl singularity of the 4D Hall effect was successfully mapped via phason engineering.

In Chapter 2, we study the topological boundary and interface modes in an acoustic quasi-periodic waveguide. Recently, experimental demonstrations of topological effects on classical phononic systems have attracted a lot of attention. The phononic analog of quantum anomalous Hall effect was realized in proposed hexagonal and square gyroscopic

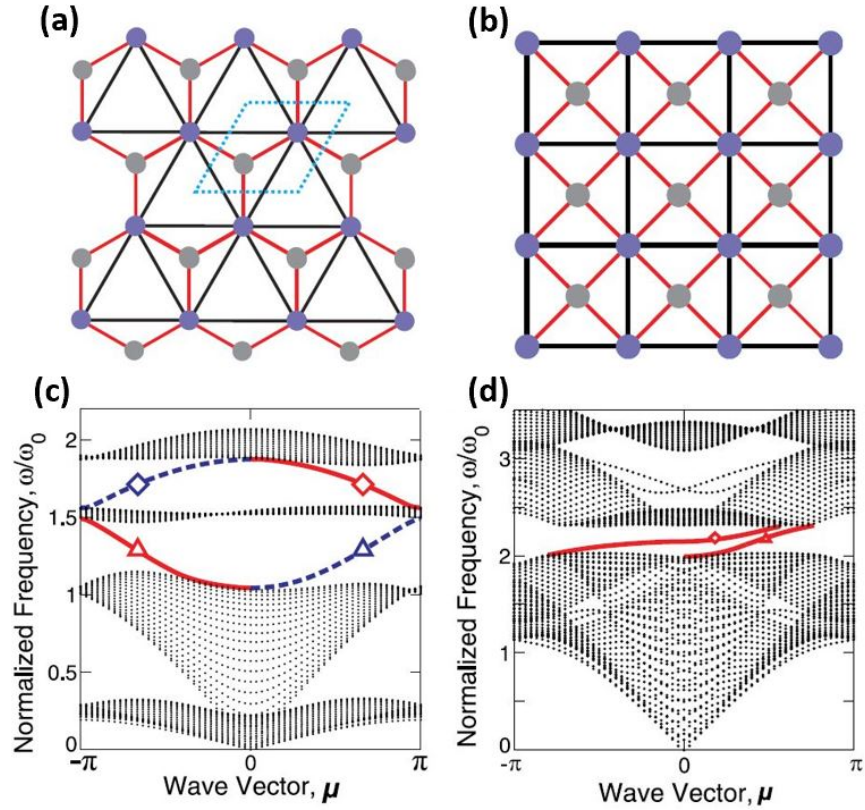


Figure 1.2 (a) Schematic of the hexagonal lattice. The blue and grey spheres represent concentrated masses $m_1 = m_2$. The red and black straight rods represent massless linear springs with stiffness k_1 and $k_2 = k_1/20$. The dashed cell is the primitive cell of the lattice. (b) Schematic of the square lattice. The blue and grey spheres represent concentrated masses $m_1 = m_2$. The black and red straight rods represent massless linear springs with stiffness k_1 and $k_2 = 2k_1$. (c) Band structure of the hexagonal lattice in (a) showing bulk bands (black dots) and edge bands (colored lines). Red solid lines represent edge modes bound to the top boundary, while blue dashed lines represent edge modes bound to the bottom boundary. (d) Band structure of the square lattice in (b) showing bulk bands (black dots) and two topological edge bands (red solid lines) bound to the top boundary.

Source: [Wang et al., 2009]

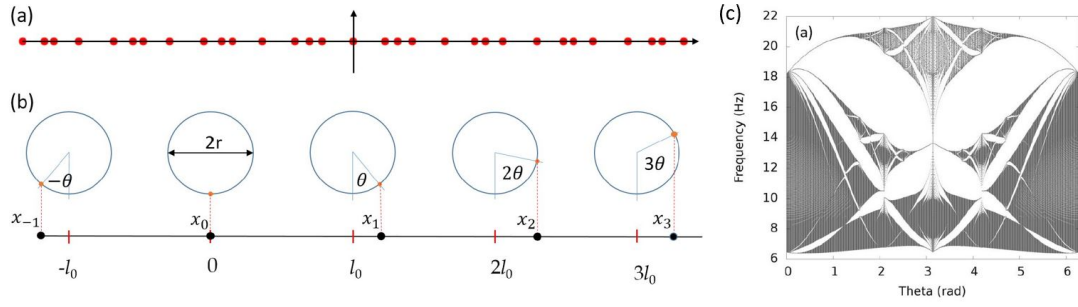


Figure 1.3 (a) A pattern consist of a finite number of points generated by the algorithm $x_n = nl_0 + r \sin(n\theta)$, with the particular values $l_0 = 1$, $r = 0.4$ and $\theta = \frac{2\pi}{\sqrt{15}}$. (b) A geometric algorithm to generate the same pattern.(c) Bulk spectrum as function of parameter θ .
Source: [Apigo et al., 2018]

phononic crystals and topologically nontrivial band gaps and one-way elastic edge waves were theoretically and experimentally investigated [Wang et al., 2009, Nash et al., 2015] as shown in Figure 1.2. Besides the periodic system, the quasiperiodic system could enhance the topological properties as the quasiperiodic Hamiltonians display a large number of gaps and the gap in the bulk resonant spectrum is topological [Apigo et al., 2018]. At the same time, acoustic resonators have been successfully used to generate topological edge modes and even to map the Hofstadter butterfly [Richoux and Pagneux, 2002, Ni et al., 2018] as shown in Figure 1.3. However, these types of acoustic structures are coupled using discrete resonators and are not breathable, which is a key requirement for many practical applications. Our goal is to generate topological edge and interface modes by quasiperiodic patterning of an acoustic waveguide without impeding the airflow. In the simulations, we optimized the geometric parameters to open large topological gaps and compute the topological invariants. Then we mapped the bulk and edge spectrum and compared it with experimental observations.

In Chapter 3, we designed an incommensurate lattice to realize the first un-assisted adiabatic pumping via pumping of the topological edge modes. In the previous chapter, a static Thouless pump was introduced, the adiabatic parameter is the phason. To change the adiabatic parameter, the measurement must be interrupted and cannot be changed

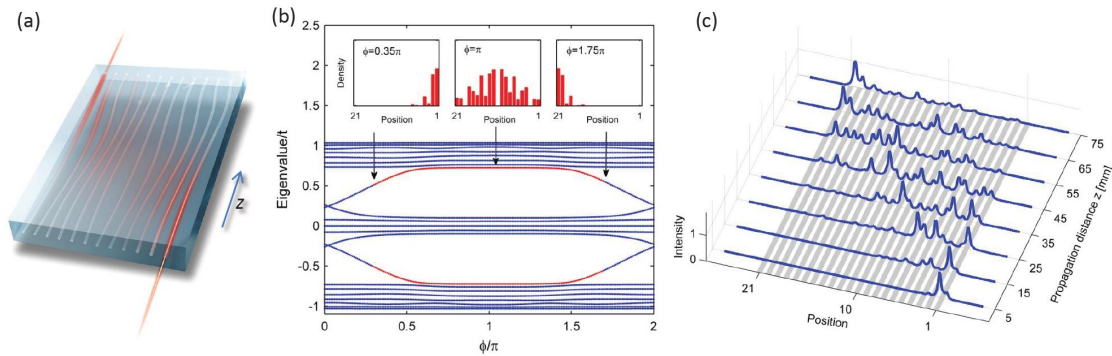


Figure 1.4 Experimental observation of static adiabatic pumping (a) An illustration of the adiabatically modulated photonic quasicrystal, constructed by slowly varying the spacing between the waveguides along the propagation axis z . (b) The spectrum of the model as a function of the adiabatic parameter ϕ . (c) The measured intensity distributions as a function of the position are presented at different propagation distance of the adiabatic evolution. It is evident that along the adiabatic evolution the light crossed the lattice from right to left.

Source: [Kraus et al., 2012]

continuously, and manually or other ways to adjust the system to get the next parameter value. Another way to realize the Thouless pumping is using coupling systems with different adiabatic parameters in space, which is shown in Figure 1.4 [Kraus et al., 2012]. However, these experiments failed to achieve a truly dynamic Thouless pump. In Grinberg's experiment as shown in Figure 1.5, dynamic side-to-side pumping technology is realized by adding active components for control. [Grinberg et al., 2020]. However, this work still has some limitations, such as the need for external intervention of active components to maintain energy, and this external intervention is complicated and expensive. Without this external intervention, the pumping would succumb to dissipation, and nothing would be picked up at the receiving end of the system. Therefore, in Chapter 3, we report the first unassisted dynamic energy transfer on acoustic metamaterials. The system is a topological aperiodic acoustic crystal whose phason can be driven quickly and periodically in an adiabatic cycle. When one edge of the metamaterial is excited within the forbidden frequency range of the topology, the microphone placed at the other end of the pumping process will start to pick up the signal. Conversely, when the prohibited frequency range is non-topological, the microphone will not pick up any signal.

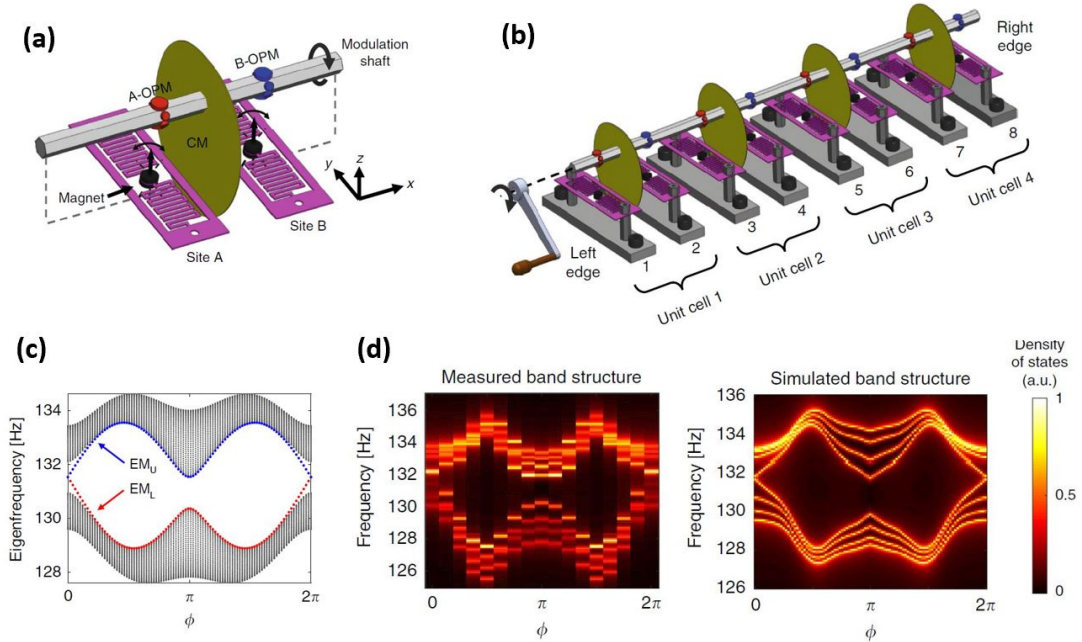


Figure 1.5 (a) Unit-cell of the magneto-mechanical system, comprises of two mechanical resonators that are coupled through magnetic interaction. Angular rotation ϕ of the modulation shaft simultaneously induces coupling modulation (CM) and on-site potential modulations (OPM). CM is generated with an off-axis high-permeability metal alloy sheet while OPM utilizes permanent magnets. (b) All experiments use an array of four unit-cells. Rotation of the shaft is motorized, though in principle a crank handle (illustrated) could be used to activate the pump. (c) Calculated band-structure for an array composed of 100 sites, as a function of the pump phase ϕ . EMU and EML are the upper and lower trajectories over which the two edge modes evolve during the pump cycle. At $\phi = 0, 2\pi$ the system is in the topologically non-trivial phase while at $\phi = \pi$ the system is in the topologically trivial phase pump. (d) The measured and simulated band structure.

Source: [Grinberg *et al.*, 2020]

In Chapter 4, quantum Hall physics has been theoretically predicted in 4D and higher. In hypothetical $2n$ -dimensions, the topological characters of both bulk and boundary are manifested as quantized non-linear transport coefficients that connect, respectively, to the n -th Chern number of the bulk gap projection and to the n -th winding number of the Weyl spectral singularities on the $(2n - 1)$ -dimensional boundaries. In this chapter, we introduce the concept of phason engineering in 2D metamaterials and use it as a vehicle to access and apply quantum Hall physics in arbitrary dimensions. Using these specialized design principles, we fabricate a re-configurable 2D aperiodic acoustic crystal with a phason living on a 2-torus, giving us access to 4D quantum Hall physics. Also, we supply direct experimental confirmation that the topological boundary spectrum assembles in a Weyl singularity when mapped as the function of the quasi-momenta. We also demonstrate topological wave steering enabled by the Weyl physics of the 3D boundaries.

CHAPTER 2

OBSERVATION OF TOPOLOGICAL EDGE MODES IN A QUASI-PERIODIC ACOUSTIC WAVEGUIDE

In this chapter, topological boundary and interface modes can be generated in an acoustic waveguide by simple quasi-periodic patterning of the walls. The work was in collaboration with Dr. David J. Apigo, Dr. Kyle Dobiszewski and Prof. Camelia Prodan from the Department of Physics at New Jersey Institute of Technology, and Prof. Emil Prodan from the Department of Physics at Yeshiva University.

2.1 Introduction

The ideas based on topological concepts [Thouless et al., 1982, Haldane, 1988] have revolutionized the field of condensed matter physics and led to the discovery of topological insulators and superconductors. The latter have been classified at the end of the previous decade [Schnyder et al., 2008, Qi et al., 2008, Kitaev, 2009, Ryu et al., 2010] and a table of strong topological phases has been conjectured. One of their common characteristics is the emergence of disorder-immune boundary modes whenever a sample is halved. Physics akin to that of topological condensed matter systems has been also predicted in classical wave-supporting materials [Haldane and Raghu, 2008, Prodan and Prodan, 2009] and many examples of topological metamaterials have been reported in the literature [Wang et al., 2009, Nash et al., 2015, Hafezi et al., 2013, Wu and Hu, 2015, Süsstrunk and Huber, 2015, Kane and Lubensky, 2014, Paulose et al., 2015, Prodan et al., 2017, Slobozhanyuk et al., 2017, Mousavi et al., 2015, Miniaci et al., 2017, Chaunsali et al., 2018, Chen et al., 2018, Pal et al., 2016].

At the same time, it has been pointed out that the periodic table of topological systems is highly enhanced if more complex systems are considered, such as the quasi-periodic or quasi-crystalline ones [Kraus et al., 2012, Verbin et al., 2013, Prodan, 2015, Baboux

et al., 2017]. In [Apigo et al., 2018], K -theoretic arguments [Bellissard, 1986, Prodan and Schulz-Baldes, 2016] were applied for quasi-periodically coupled discrete mechanical resonators. The finding was that, if these are single-mode resonators, then every gap in the bulk resonant spectrum is topological, in the sense that it will be completely filled by boundary spectrum under any boundary condition. The practical value of the finding is that the quasi-periodic Hamiltonians display a large number of topological gaps, hence one can generate localized wave-modes in both space and energy by simply halving the system.

In this work, we put these general principles to the test in a completely different regime and we implement them for the first time using sound waves. Acoustic setups have been successfully used in the past to generate topological edge modes [Xiao et al., 2015, He et al., 2016, Ni et al., 2018] and even to map the Hofstadter butterfly [Richoux and Pagneux, 2002]. In particular, [Ni et al., 2018, Richoux and Pagneux, 2002] introduced re-configurable acoustic resonant structures where the building blocks are sealed acoustic chambers connected via thin bridges. They have isolated resonant modes; hence these structures fall under the umbrella of patterned resonators introduced in [Apigo et al., 2018] and they can be analyzed by similar methods. However, these types of acoustic structures are not breathable, which is a key requirement for many practical applications. As such, here we ask the question: Can one generate topological edge and interface modes by patterning the walls of an acoustic waveguide without impeding the air flow?

2.2 Construction of the Continuous Hull of the Waveguide

As we shall see, the answer is yes, but the methods of analysis are very different from those introduced in [Apigo et al., 2018]. Indeed, the picture of coupled discrete resonators is no longer applicable and a full continuum medium treatment must be employed for the theoretical analysis. Furthermore, the topological character of the spectral gaps cannot be taken for granted because the waveguide supports many overlapping modes. As such, a new assessment of the topological character is introduced based on the continuum version of the

lattice non-commutative Chern number proposed in [Prodan, 2015], achieved in [Bourne and Rennie, 2018]. This invariant is here evaluated numerically using the methods developed in [Prodan, 2017a, Bourne and Prodan, 2018].

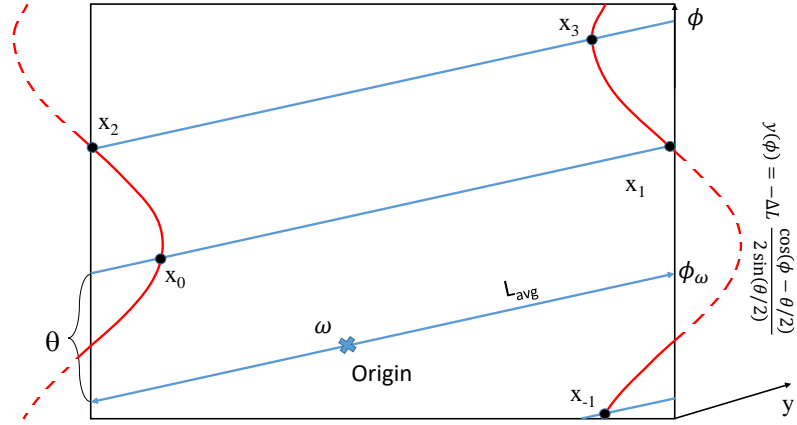


Figure 2.1 The virtual manifold associated to the patterned waveguide is a 2-torus.

The aperiodic continuum systems are quite different from the discrete aperiodic ones for the following reasons: They can be halved at any point of their axis. Hence, the phason ϕ alone does not specify completely the configuration of the waveguide, for we also need to know where the origin of the Euclidean space is located relative to the walls of the patterned waveguide. This is so because, by convention, it is at this origin where the cut is made and the edge modes emerge. The bulk topological invariant, while still a formal Chern number, is defined on a different algebra of observables. The proof [Bourne and Rennie, 2018] of the quantization and stability of the topological invariants for continuum models also proceeds quite differently from the one for discrete models [Prodan and Shmalo, 2019].

The continuous hull Ω of the patterned waveguide is the topological space traced by the pattern when one continuously translates the waveguide along the axis [Bellissard, 1986]. Here we show that Ω is a 2-torus. With the elements introduced in Figure 2.1, let $\omega \in \mathbb{T}^2$ be an arbitrary point and imagine the blue line as being a physical rope wound around the torus. Let the red line, whose equation is supplied in the diagram, be soaked with ink so that, every time when the rope crosses the red line, a mark is imprinted. Let us

label these marks as shown in the diagram. Then, after we unwind the rope and lay it flat and parallel to axis of the tube, one will find that:

$$x_{n+1} - x_n = L_{\text{avg}} + y((n+1)\theta + \phi_\omega) - y(n\theta + \phi_\omega) = L_{\text{avg}} + \Delta L \sin(n\theta + \phi_\omega). \quad (2.1)$$

The marks x_n will overlay perfectly over the centers of the walls if the origin of the Euclidean space is fixed at x_ω (the position of ω on the rope)!

The conclusion is that every rigidly translated waveguide configuration can be uniquely characterized by a point $\omega \in \mathbb{T}^2$, hence the continuous hull is the 2-torus. Furthermore, the group of translations parallel to the waveguide's axis induces an action τ of \mathbb{R} on \mathbb{T}^2 , which amounts to shifting ω along the winded rope. As such, the hull becomes a topological dynamical system $(\Omega, \tau, \mathbb{R})$.

Let us recall from [Apigo et al., 2018] that the role of aperiodicity in this type of applications is to generate virtual dimensions, the Chern number mentioned above is defined on a 3-dimensional non-commutative manifold, while for discrete patterns is on a 2-dimensional manifold.

At the experimental level, challenges exist because some of the spectral bands are very narrow and this, together with the aperiodicity, can lead to irregular mode profiles, although the bulk states are extended. As such, the only way to accurately map the bulk spectrum is to collect data from a large number of points along the waveguide. Following this protocol, we map not only the frequency but also the spatial profile of the bulk modes. Furthermore, inside the topological bulk gaps, we were able to detect sharp edge modes, which flow with the phason degree of freedom in a manner consistent with the computed Chern numbers.

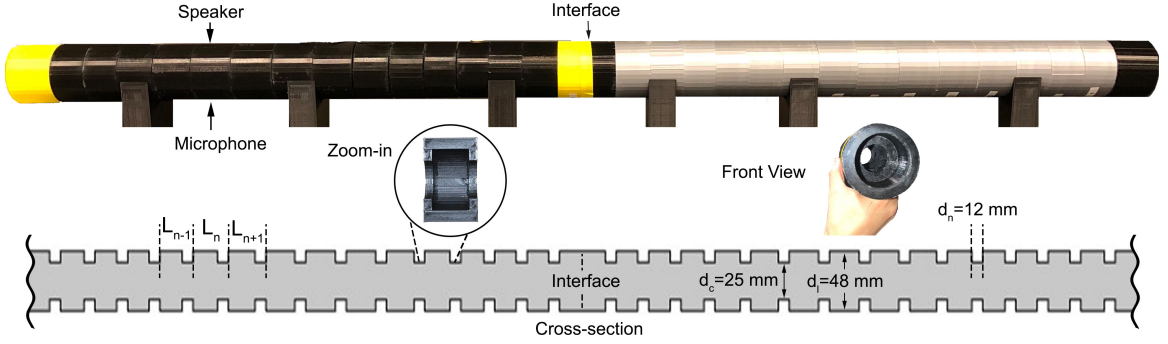


Figure 2.2 Top: photograph of the waveguide configuration used to measure topological interface modes. Bottom: Cross-section and geometrical parameters. The waveguide consists of interlocking 3D printed PLA parts as shown in the insert and it is mirrored relative to the domain wall indicated by the dashed line. For experimentation, a speaker is placed at portholes accessible in each chamber and a piezoelectric microphone is inserted into an opposite porthole. The portholes that are not in use are sealed. The lengths L_n were generated with Equation (2.1) and their average was fixed at $L_{\text{avg}} = 40$ mm. The parameters in Equation (2.1) were fixed at $\Delta L = 0.2L_{\text{avg}}$ and $\theta = \frac{2\pi}{\sqrt{117}}$. This particular irrational fraction of 2π accepts a good rational approximation $\theta = \frac{9\pi}{48} + \mathcal{O}(10^{-3})$, which was used in some of the numerical calculations. The system was also run without a domain wall, for bulk and edge measurements.

2.3 The Quasi-periodic Acoustic Waveguide Experimental Platform

The quasi-periodic acoustic waveguide consists of a uniform cylindrical tube decorated with walls. The parts were 3D-printed out of polylactic acid (PLA) using an Ultimaker 3 and then assembled as in Figure 2.2. The walls have identical thickness but the spacing between adjacent walls are modulated according to the algorithm:

$$L_n = L_{\text{avg}} + \Delta L \sin(n\theta + \phi), \quad n \in \mathbb{Z}. \quad (2.1)$$

The geometric parameters used in the experiments are supplied in Figure 2.2. To make the above labels meaningful, we assume that the waveguide is centered at a point inside L_0 . In Equation (2.1), θ is an angle incommensurate with 2π , which will be kept fixed during the measurements, and ϕ is the phason, which should be let to vary. For example, a simple relabeling $n \rightarrow n + m$, which corresponds to re-centering the waveguide, will change ϕ into $(\phi + m\theta) \bmod 2\pi$. Since θ is incommensurate, these relabelings alone will sample the

phason densely in the $[0, 2\pi]$ interval. L_{avg} in Equation (2.1) is the average distance between the walls and ΔL sets the magnitude of the fluctuations in L_n .

In the inset of Figure 2.2, we show a front view of the waveguide, confirming that air can flow freely through the structure. It is then somewhat striking that, with the proposed patterning, we can stop sound propagation over several intervals of frequencies and, furthermore, we can generate, very much on demand, topological sound modes localized at any desired location along the tube. As opposed to an ordinary resonant mode produced in a fully sealed acoustic chamber, the interface modes produced in the present work have less contact with the boundary, hence they are expected to have very high Q-factors, a much desired characteristic for practical applications.

2.4 Effect of Patterning

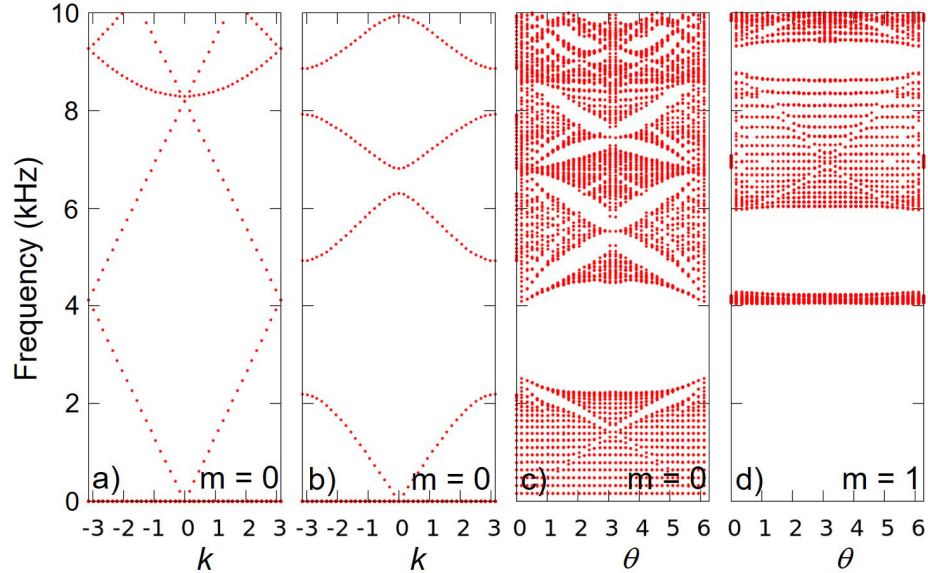


Figure 2.3 (a) Dispersion of the acoustic modes for the un-patterned waveguide, for $m = 0$ sector. (b) The band structure of a periodically patterned waveguide (*i.e.* $\theta = 0$), for $m = 0$ sector. (c,d) Resonant spectrum of a patterned waveguide as function of θ , for $m = 0, 1$ sectors, respectively.

To understand the effect of the patterning, we report in Figure 2.3 the dispersion of the acoustic modes for clean and periodically ($L_n = L_{\text{avg}}$) patterned waveguides, as well as the resonant spectrum of the aperiodically patterned waveguide (L_n set by Equation(2.1)).

As expected for quasi 1-dimensional wave propagation, the periodic pattern opens spectral gaps in the gapless spectrum of the clean tube. These gaps, however, are not topological. The role of aperiodicity is to open additional gaps in the spectrum that, as one can see, resemble quite closely the Hofstadter butterfly [Hofstadter, 1976], when mapped as function of θ . As we shall see, these are the gaps that carry non-trivial bulk topological invariants prompting the topological edge and interface modes. Let us mention that the spectra in Figure 2.3 were produced with an in-house Fortran code, which diagonalizes the Laplace operator expressed in the cylindrical coordinates (ρ, z) and resolved over the azimuthal symmetry sectors. In appropriate units, the operator reads:

$$\Delta_m = -\frac{1}{\rho} \frac{\partial}{\partial \rho} \rho \frac{\partial}{\partial \rho} + \frac{m^2}{\rho^2} - \frac{\partial^2}{\partial z^2}, \quad m = 0, \pm 1, \dots, \quad (2.2)$$

and von Neumann condition is considered at the boundary. Recall that the latter is set by θ and ϕ , hence Δ_m depends in a fundamental way on these parameters. The Laplace operator was discretized using finite differences.

2.5 Experimental Results

2.5.1 Experimental Protocol

The protocol for acoustic data acquisition was as follows. Sinusoidal signals of duration 1 s and amplitude of 0.5 V were produced by a Rigol DG1022 function generator, amplified by a Crown XLS 2502 power amplifier with the gain set to 6, and then applied on a CUI Inc. GF0501 speaker, placed at one of the portholes. A PCB Piezotronics Model-378C10 microphone and a PCB Piezotronics Model-485B12 power conditioner acquired the acoustic signals at a porthole opposite the speaker (see Figure 2.2). To account for the frequency-dependent response of the components, a separate measurement is performed with the waveguide removed but speaker and microphone kept in the same positions. All readings are normalized by the output of these measurements. The outputs were read by a

custom LabVIEW code via a National Instruments USB-6112 data acquisition box and the ratio of the two measurements is stored on a computer for graphic renderings.

2.5.2 Bulk Spectrum and Measurement

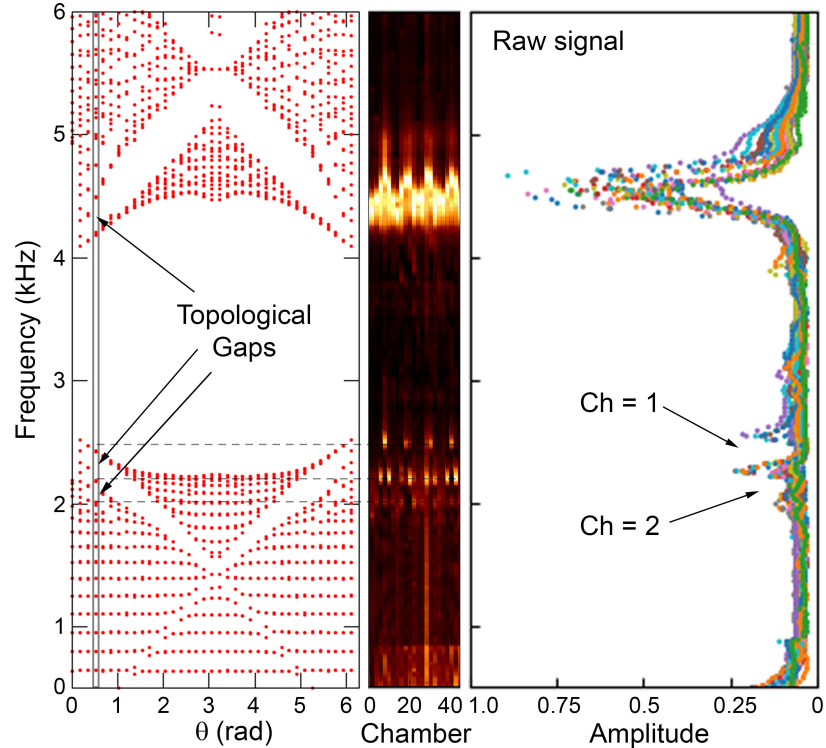


Figure 2.4 Bulk resonant spectrum for the geometry described in Figure 2.2. Left: Theoretical resonant spectrum reproduced from Figure 2.3(c), with arrows indicating the topological gaps. The vertical marking identifies $\theta = \frac{2\pi}{\sqrt{117}}$, used in experiments. Center: Normalized microphone readings from the center of 48 chambers, recorded over a wide frequency interval. Right: Collapse on the frequency axis of the intensity plot reported in the mid panel. Three spectral gaps can be clearly identified in the experimental data and seen to be well aligned with the theoretical calculations. The values of the Chern numbers for the two topological gaps are also indicated.

For the bulk measurements, the protocol was repeated for all 48 chambers of a patterned waveguide, with frequency scans from 500 to 6000 Hz in 25 Hz steps. The results are reported in Figure 2.4. When the data is rendered as function of frequency and chamber index, clear extended acoustic modes can be identified. Furthermore, when the data is collapsed on the frequency axis, clear spectral gaps can be identified, two of which are predicted to be topological. Unfortunately, the $m = 0, 1$ spectra overlap above the

non-topological gap (see Figure 2.3) and the higher frequency topological gaps could not experimentally resolved. Let us note that the agreement between experiment and theory in Figure 2.4 is less than 5%.

To assess the topological character of the gaps, we employ the bulk-boundary correspondence for continuum models established in [Bourne and Prodan, 2018]. The bulk-topological invariant is supplied by the non-commutative Chern number of the gap projection $P_G = \chi_{(-\infty, G]}(\Delta_m(\phi) - G)$:

$$\text{Ch}(P_G) = \text{Tr}_L(P_G[\partial_\phi P_G, [Z, P_G]]), \quad (2.2)$$

where Z is the position operator parallel to the tube and Tr_L is the trace per length. The invariant can be computed at any arbitrary but fixed phason value, which is a consequence of Birkhoff ergodic theorem [Birkhoff, 1931]. With the Laplacian discretized on a lattice via finite differences, Equation (2.2) was evaluated using methods which are by now standard [Prodan, 2017a, Prodan and Shmalo, 2019]. The results are reported in Figure 2.4, confirming that the smaller gaps are topological. Furthermore, [Bourne and Prodan, 2018] established the existence of a boundary topological invariant which counts the number of chiral boundary bands, as well as the equality between the bulk and boundary invariants.

2.5.3 Topological Edge Spectrum and Measurement

The presence of chiral modes, in accordance to the above bulk-boundary principle, is confirmed by our numerical simulations reported in Figure 2.5a. To map the boundary modes experimentally, the acquisition protocol was applied on the second chamber from the left physical edge, which was plugged. The frequency was swept from 2.0 to 2.6 kHz in steps of 25 Hz and the value of the phason was modified by moving the physical edge sequentially to the right, hence from L_0 to L_n , $n = 1, 2, \dots$. The results are presented in Figure 2.5b and they indeed confirm the existence of one chiral band in the upper topological

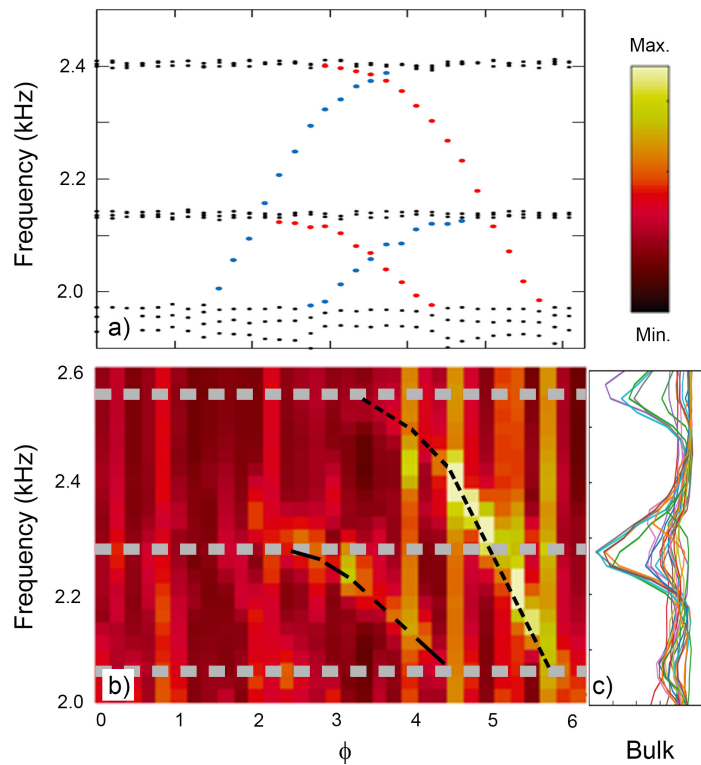


Figure 2.5 Topological edge spectrum. (a) Theoretical prediction of the spectral flow against the phason parameter ϕ , demonstrating the existence of chiral bands. The red/blue marks relate to the left/right edge of the waveguide, respectively. (b) Experimental mapping of the spectral flow, confirming the existence of chiral bands. (c) The measurements for bulk spectrum, reproduced from Figure 2.4, indicating the position of the bulk gap edges.

gap and two such bands in the lower topological gap. For reference, we reproduced in panel c) the experimental data from Figure 2.4, from where the exact position of the bulk edges can be inferred. As one can see, the boundary resonances occur inside the bulk gaps and the dispersion with ϕ is consistent with the theoretical prediction.

2.5.4 Topological Interface Mode Measurement

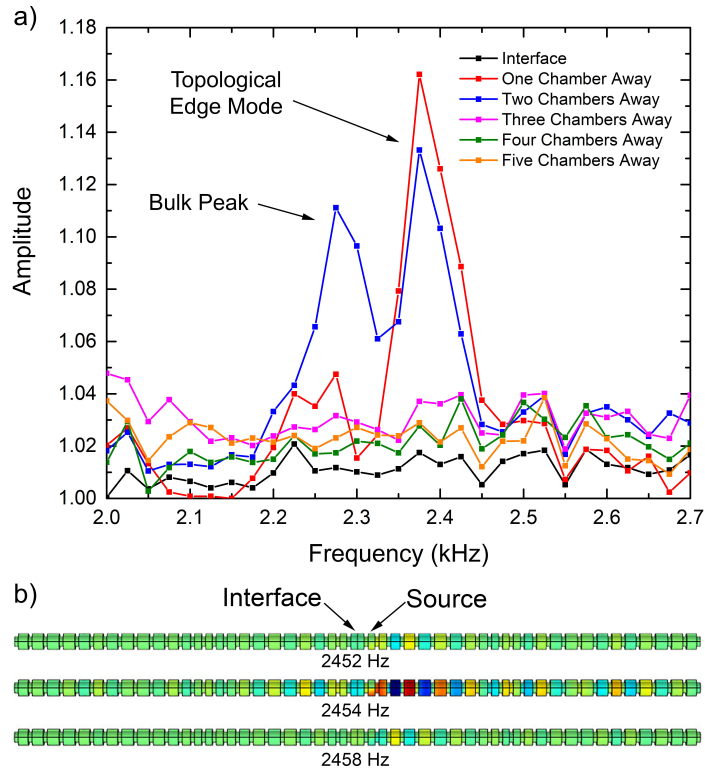


Figure 2.6 (a) Topological interface mode, measured for a waveguide configuration similar to that in Figure 2.2. The spatial localization of the interface mode was mapped by moving the speaker and microphone away from the domain wall. (b) The topological interface mode is also observed in COMSOL simulations. Red, blue and green colors represent high, low and zero pressure variations, respectively.

We now demonstrate that a localized topological edge mode can be created without the assistance of any plug. For this, we consider a domain wall configuration:

$$\dots |L_{31}|L_{30}|L_{29}|L_{29}|L_{30}|L_{31}| \dots$$

where the waveguide is mirror-reflected relative to left edge of L_{29} chamber. This particular index was chosen because moving the origin to that chamber generates a phason $\phi = (29\theta) \bmod 2\pi$, which coincides with the value where strong mid-gap edge modes were observed in the first topological gap. Since Equation 2.2 is odd under reflection, with this patterning, an interface between topological systems with opposite Chern numbers is created. As such, the bulk-boundary principle predicts the emergence of $2 \times \text{Ch}$ acoustic modes localized at the interface.

The experimental measurements are reported in Figure 2.6(a). The frequencies were swept as in Figure 2.5 and, in order to probe the localization of the acoustic modes, the speaker and microphone were placed at several portholes at and away from the interface. A strong and sharp resonance was detected in the first topological gap ($\text{Ch} = 1$), when the measurements were performed one and two chambers away from the interface. The resonance was not detectable further away from the interface or at the interface itself. A similar resonance can be detected at the other side of the interface, leading to a full confirmation of the topological bulk-boundary prediction. The interface mode is also observed in a standard COMSOL simulation, as shown in Figure 2.6(b).

2.6 Summary

In conclusion, we have demonstrated that topological edge and interface modes can be created by a simple quasi-periodic patterning of an acoustic waveguide. The topological gaps can be easily identified when the resonant spectrum is mapped as function of modulation parameter θ . Furthermore, a topological invariant was computed and shown to be in agreement with the number of observed topological chiral edge modes.

As we have seen, quasi-periodicity opens topological gaps inside the bands of the periodic structure, which resemble the Hofstadter butterfly when mapped as function of θ . Optimization over ΔL in Equation (2.1) and the geometric parameters of the tube, as well as improvements in materials (*e.g.* by replacing the polymer with metal), can highly enhance

these topological gaps and the Q-factors of the topological boundary and interface modes. Other than that, the procedure requires no further fine tuning and, due to its simplicity, we believe it can be easily incorporated in practical applications. The present analysis can also serve as a model for acoustic implementations of many other promising aperiodic structures [Prodan and Shmalo, 2019].

CHAPTER 3

EXPERIMENTAL DEMONSTRATION OF TOPOLOGICAL PUMPING ACROSS INCOMMENSURATE BILAYERED ACOUSTIC METAMATERIALS

In this chapter, the first un-assisted dynamic energy transfer across a metamaterial has been experimentally demonstrated, via pumping of such topological edge modes. The system is a topological aperiodic acoustic crystal, with a phason that can be fast and periodically driven in adiabatic cycles. The work was in collaboration with Prof. Emil Prodan from the Department of Physics at Yeshiva University and Prof. Camelia Prodan from the Department of Physics at New Jersey Institute of Technology.

3.1 Introduction

More than 35 years ago, Thouless asked himself what happens with a filled sea of fermions when the underlying potential is slowly and periodically modulated in time [Thouless, 1983]. He predicted that a precise non-fluctuating number of particles will be effectively transported from one side of the system to the other and that this number is determined by a topological invariant computed for a virtual system of one dimension higher than the original. The effect has been directly demonstrated recently, with both fermions and bosons [Nakajima et al., 2016, Lohse et al., 2016]. It is now well established [Xiao et al., 2010, Prodan, 2015] that augmentation of a parameter space to a d -dimensional quantum or classical system can give access to topological effects that, in normal conditions, are observed in $d + 1$ or higher dimensions. The prototypical example is the periodic one-dimensional Rice-Mele model [Rice and Mele, 1982], where an adiabatic deformation of the parameters leads to a virtual two-dimensional system whose energy bands support non-trivial Chern numbers [Xiao et al., 2010]. As a result, the system displays chiral edge bands when driven in an adiabatic cycle and edge-to-edge topological pumping becomes possible.

The existing experimental works on edge-to-edge topological pumping can be classified in three groups. The ones in the first group [Apigo et al., 2018, Apigo et al., 2019, Ni et al., 2019, Voss and Ballon, 2020, Hafezi et al., 2013, Xia et al., 2020] report only renderings of the resonant spectra as functions of the adiabatic parameters. The parameters are not varied continuously but rather the measurements are interrupted and the systems are adjusted by hand or other means to achieve the next parameter values. Acquisition of the spectra for a single adiabatic cycle can take days. In the experimental works from the second group [Kraus et al., 2012, Rosa et al., 2019, Riva et al., 2020, Shen et al., 2019, Zilberberg et al., 2017, Lustig et al., 2019, Verbin et al., 2015], the systems with different adiabatic parameters are rendered and coupled in space and the profiles of the resonant modes are mapped in space rather than time. The connection with a real dynamical Thouless pump is done through a mathematical argument that involves simplifications and assumptions [Kraus et al., 2012]. Lastly, the experimental works in the third group [Grinberg et al., 2020, Xia et al., 2021] report assisted dynamical edge-to-edge pumping. We call it *assisted* primarily because energy was pumped into the mode to keep it alive as it traversed from one edge to another. Without such external intervention, the pumping would have succumbed to the dissipation and nothing would have been observed at the receiving end of the system. These experiments also contain a large number of active components controlled by an expensive layer of electronics, whose complexity grows with the size of the system. For this reason, the system in [Grinberg et al., 2020] had only eight unit cells. While valuable demonstrations, these approaches do not offer yet a path towards practical implementations.

We demonstrate an un-assisted edge-to-edge topological pumping of sound, where the human intervention is completely absent once the mode is loaded at one end of the system. The key innovation is the use of an aperiodic meta-material structure that has a simple built-in mechanism that implements global structural changes resulting in rapid and repeated cyclings of its phason. This mechanism is simply the relative sliding of two coupled incommensurate periodic acoustic crystals. All the previous experimental

works based on aperiodic structures employ the quasi-periodic pattern originally proposed in [Kraus et al., 2012], where the dynamical matrices can be directly connected with the Aubry-André and Harper models [Aubry and André, 1980, Harper, 1955]. This is not the case for an incommensurate bilayered acoustic crystal, yet we show in the following section that its dynamical matrix belongs to an algebra isomorphic to that of magnetic translations. As such, the spectral gaps carry Chern numbers and the bulk-boundary correspondence principle is the same as for the Chern insulators. However, our topological system is distinct from the standard Chern mechanical crystals [Prodan and Prodan, 2009, Wang et al., 2015, Nash et al., 2015] because one dimension is virtual.

Using the phason of a quasi-periodic structure to generate topological edge modes is an appealing strategy because the bulk resonant spectrum is independent of the phason, hence *all* the bulk spectral gaps are preserved during the phason cycles. This remarkable characteristic is unmatched by any other design principle. Furthermore no fine-tuning of the systems is required [Apigo et al., 2018], because the presence of topological edge modes stems from the aperiodic pattern alone. In [Prodan and Shmalo, 2019], we supplied an algorithmic method to generate aperiodic system with phasons living on generic topological spaces. In particular, [Prodan and Shmalo, 2019] identified the phason space for incommensurate bilayered patterns. The principles discovered in [Apigo et al., 2018] and [Prodan and Shmalo, 2019] made the present work possible.

Our main results are summarized in Figure 3.1, where we present direct evidence of energy transfer from one end of a bulk structure to the other end, even though the frequency of the source falls in a forbidden wave-propagation range. This energy transfer happens in pumping conditions and when the source frequency is in a topological spectral gap of the metamaterial. In contradistinction, when the frequency is adjusted in a non-topological spectral gap, there is no energy transfer even though same conditions of pumping are applied. Our experimental platform consists of the two incommensurate periodic arrays of acoustic resonators described in Figure 3.1(a-c). The dimensions have been optimized to

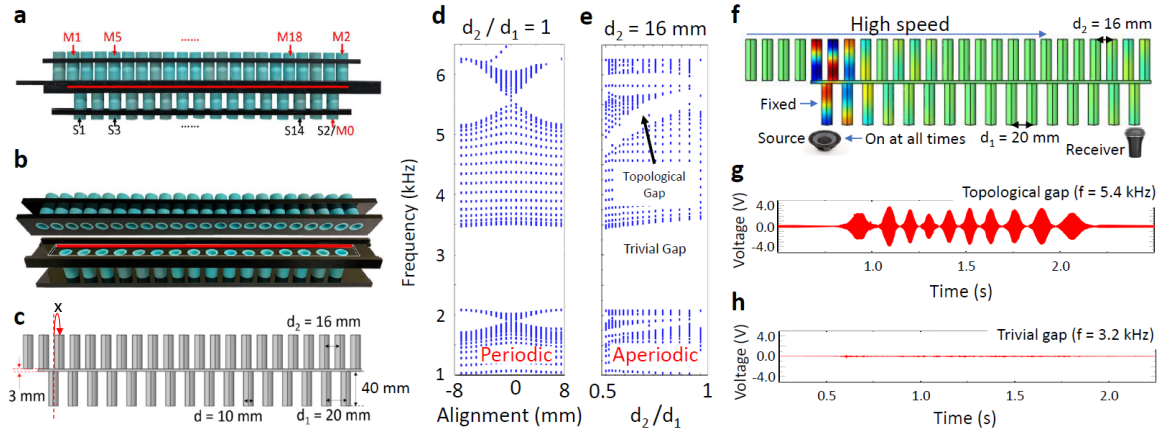


Figure 3.1 (a) Photograph of a fully assembled acoustic bilayer consisting of top/bottom periodic arrays of cylindrical acoustic resonators with incommensurate lattice constants. The labels S_i and M_i indicate the positioning of the speaker and microphone during various experiments referenced in the text. The middle red bar indicates the presence of an inner chamber, which connects the top and bottom resonators and is referred to as the spacer. For dynamical pumping, additional resonators are mounted on the top left side. (b) Photograph of the inner structure, with the spacer now fully visible. (c) Cross-section showing only the domain of wave propagation, together with relevant parameters. Note that the very left resonator is completely decoupled from the main structure. (d) Bulk resonant spectrum as function of top-bottom relative alignment, when the top and bottom lattice constants are equal. In this case, all spectral gaps are trivial. (e) Bulk resonant spectrum as function of d_2/d_1 . In this case, additional gaps open in the spectrum, which are all topological. (f) Schematic of the pumping process as well as a simulation of the air pressure at the beginning of the pumping cycle. (g) Microphone reading when the source frequency is adjusted in a topological gap. (h) Microphone reading when the source frequency is adjusted in a non-topological gap.

maximize the size of the topological gap. This type of patterned resonators was theoretically studied in [Prodan and Shmalo, 2019], where it was found to support topological spectral gaps and topological edge modes. However, to our knowledge, this is the first time when coupled incommensurate chains are experimentally used to engineer chiral edge bands for topological pumping.

Key to our experimental design was the replacement of any elaborate interconnections between acoustic resonators with a thin uniform spacer, extending from one end of the structure to the other. The resonators are attached to and coupled through this spacer. Note that this type of coupling does not allow fine-tuning but, as we mentioned, that is not necessary when using aperiodic principles, as long as the coupling is strong [Apigo et al., 2018]. Furthermore, edges can be created by simply filling the spacer with solid material. The adiabatic parameter of the system is $\varphi = x/d_2$, where x and d_2 are specified in Figure 3.1(c). Note that φ lives on the circle, which is only a part of the total phason space. The advantages of our design are: a) φ can be driven in an adiabatic cycle by simply sliding the top array while holding the bottom one fixed; b) Since the bottom array is fixed, we can continuously pump energy at one edge (and only on that edge) by placing a source on the first bottom resonator; c) The left and right edges can be independently adjusted to achieve the optimal dispersion of the edge modes.

3.2 Computing the Phason Space

We recall from [Prodan and Shmalo, 2019] how any finite piece of the incommensurate bilayer can be generated from a simple dynamical process over the non self-intersecting loop Ω shown in Figure 3.2(a). When viewed from above, Ω appears as a figure eight as in Figure 3.2(b), made out of two circles of perimeters d_1 and $d_2 < d_1$. We call this the projected Ω . While walking on Ω in the positive direction indicated by the arrow in Figure 3.2, one passes from the large circle to the small circle at point J , and then from the small circle back to the large circle at point J' . Consider now the group action

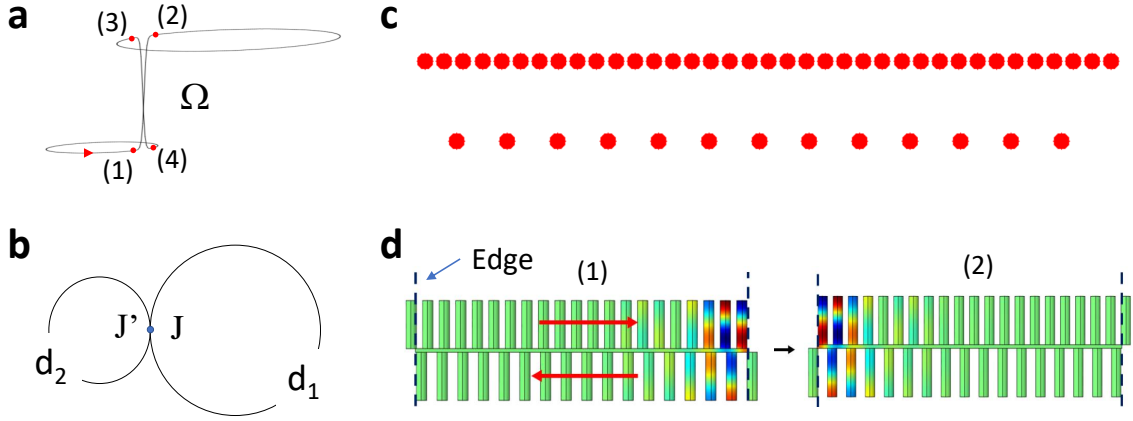


Figure 3.2 Phason Space consists of steps of length θ on the smooth and non self-intersecting loop shown on the left. The right diagram shows a view from the top.

$\tau : \mathbb{Z} \rightarrow \text{Homeo}(\Omega)$ such that τ_n moves a point ω by $n d_2$ along the projected Ω in the positive direction. On the real Ω , this action also changes the vertical coordinate of the point. For $\omega \in \Omega$, let $d_{+/-}(\omega)$ be the distance from ω to J' as moving on the projected Ω in the positive/negative direction. The vertical coordinate of a point $\omega \in \Omega$ will be denoted by $Y(\omega)$. Then the algorithm for producing the incommensurate bilayer can be described as follows. We put our pencil on an arbitrary $\omega \in \Omega$ and, in the same time, we center a resonator at coordinates $(0, Y(\omega))$ of the physical space \mathbb{R}^2 . Then we move ω in the positive direction by d_2 on the projected Ω , and we center another resonator at horizontal and vertical coordinates $\Delta_x(\omega) = \min\{d_2, d_{\pm}(\tau_1\omega)\}$ and $\Delta_y(\omega) = Y(\tau_1\omega) - Y(\omega)$, relative to the previous resonator. By repeating this step, we generate an iterative process $\mathbf{p}_{n+1} = \mathbf{p}_n + \Gamma(\tau_n\omega)$, with Γ a continuous function from Ω to \mathbb{R}^2 defined by $\Gamma(\omega') = (\Delta_x(\omega'), \Delta_y(\omega'))$ for any $\omega' \in \Omega$. In Figure 3.2(c), we show a pattern $\{\mathbf{p}_n\}$ of 100 resonators generated with this algorithm and with the equation for Ω taken from [Prodan and Shmalo, 2019]. As one can see, it indeed reproduces a finite incommensurate bilayer.

When ω happens to land in the interval (1-2) between points (1) and (2) or the interval (3-4) between points (3) and (4) shown in Figure 3.2(a), the algorithm will produce a point which is in between the bilayers. These are very rare events if the transitions between the top and bottom sections of Ω are made very sharp. Nevertheless, these transitions can be

interpreted experimentally in the following way. In Figure 3.2(d), we show the patterns generated with ω sitting at point (1) and at point (2). If we switch continuously between these two resonator configurations, the bottom resonator disappears beyond the edge while the top resonator gradually appears. Experimentally, we will associate these resonator configurations with an ω running continuously from location (1) to location (2) on Ω . A similar correspondence can be worked out when ω runs in the interval (3-4).

The algorithm can be seeded from any point ω of the loop Ω and this will result in different patterns of resonators. The difference between these patterns can be assessed as follows. First, note that if we start from $\tau_n\omega$ instead of ω , we rigidly shift the pattern such that point p_n sits at the origin. Equivalently, we can think that an observer has been moved from resonator p_0 to p_n . Now, as the observer moves from one resonator to another, he/she will see different patterns of resonators and attributes this phenomenon to the existence of a degree of freedom, which, by definition, is the phason itself. Certainly the phason takes the values $\tau_n\omega$ and, if d_2 and d_1 are incommensurate, then these values fill Ω densely as n is varied in \mathbb{Z} . The conclusion is that Ω parametrizes all the patterns seen by the observer, hence the phason leaves on the set Ω described Figure 3.2.

3.3 Origin of the Topological Gaps

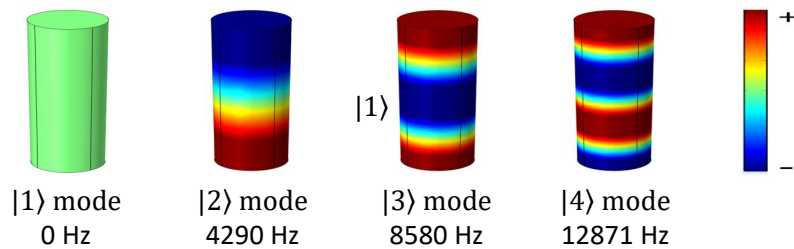


Figure 3.3 Elementary resonant modes.

Resolving the spectral and topological properties of aperiodic patterns of resonators starts with the computation of the algebra of observables [Bellissard, 1986]. The K -theory of this algebra then supplies the unique topological labels for the spectral gaps [Bellissard,

1992]. In Figure 3.3 we report the first four elementary modes supported by the individual capped resonators. By examining their frequencies, it becomes clear that the collective modes reported in Figure 3.5, practically involve only these four modes. As such, the dynamical matrix of the collective resonant modes takes a discrete form:

$$\widehat{D}_\omega = \sum_{n,n'} w_{n',n}(\omega) \otimes |n'\rangle\langle n|, \quad (3.1)$$

where $w_{n',n} \in M_{4 \times 4}(\mathbb{C})$ is the matrix which couples the elementary modes supported by resonators n and n' . The index ω reflects the dependence on the choice of the origin, where the edge will be placed, and consistency requires the following covariant relations:

$$w_{n'+a,n+a}(\omega) = w_{n',n}(\tau_a\omega), \quad \forall n, n', a \in \mathbb{Z}. \quad (3.2)$$

Choosing $a = -n$ and replacing ω by $\tau_n\omega$, we find $w_{n',n}(\omega) = w_{n'-n,0}(\tau_n\omega)$, hence we can drop one index and using $q = n' - n$, as well as the shift operator:

$$S|n\rangle = |n+1\rangle, \quad S^\dagger|n\rangle = |n-1\rangle, \quad SS^\dagger = S^\dagger S = I, \quad (3.3)$$

the generic dynamical matrix becomes:

$$\widehat{D}_\omega = \sum_q S^q \sum_n w_q(\tau_n\omega) \otimes |n\rangle\langle n|. \quad (3.4)$$

As one can see, the generic dynamical matrices belong to the algebra generated by the shift operator S and by diagonal operators of the form $\sum_n f(\tau_n\omega) |n\rangle\langle n|$ with f a continuous

function over Ω . Since any such function can be Fourier decomposed, we find that the algebra is in fact generated by just two operators, namely, S and $V = \sum_n \exp\left(2\pi i \frac{\tau_n \omega}{d_1 + d_2}\right) |n\rangle\langle n|$. Furthermore, a direct computation shows that:

$$VS = e^{2\pi i \phi} SV, \quad \phi = \frac{d_2}{d_1 + d_2}. \quad (3.5)$$

This is the commutation relation of the magnetic translations in 2-dimensions, provided we take the flux per unit cell to be ϕ in the quantum units of flux. Hence, the fragmentation of the bands seen in Figure 3.4 is as in the Hofstadter butterfly [Hofstadter, 1976]. In particular, the gaps can be labeled by Chern number.

3.4 Coupled Incommensurate Chains Experimental Platform

3.4.1 Numerical Simulations

All numerical simulations were performed with COMSOL Multiphysics. This commercially available software was used to map the self-sustained acoustic wave-modes for different resonator configurations under hard boundary conditions.

3.4.2 Fabrication

All resonators were fabricated with an Anycubic Photon 3D printer which uses UV resin and has 47 μm XY-resolution and 10 μm Z-resolution. The dimensions of the resonators are supplied in Figure 3.1. The resonators were mounted in laser-cut acrylic plates, such that their open ends were perfectly flushed. The spacer was also laser-cut from an acrylic plate and glued to the plate where the bottom resonators were mounted. Its dimensions are supplied in Figure 3.1. The spacer was fitted with lateral guiding rails to hold in place the acrylic plate which supports the top resonators. For all laser-cutting, we used the Boss Laser-1630 Laser Engraver. The thickness of all the walls was large enough ($\geq 2\text{mm}$) to justify rigid boundaries in our numerical simulations.

3.4.3 Experimental Protocols

The protocol for the acoustic bulk measurements reported in Figure 3.6 was as follow. Sinusoidal signals of duration 1 s and amplitude of 0.5 V were produced with a Rigol DG 1022 function generator and applied on a speaker placed in a porthole opened in a resonator of the bottom row. A dbx RTA-M Reference Microphone with a Phantom Power was inserted in a porthole opened in a resonator of the top row and acquired the acoustic signals. To account for the frequency-dependent response of the components, several separate measurements were performed with the structure removed but speaker and microphone kept at the same positions. All our microphone readings are normalized by these reference measurements. The signals were read by a custom LabVIEW code via National Instruments USB-6122 data acquisition box and the data was stored on a computer for graphic renderings. To generate the data in Figure 3.5, the microphone was placed on 14 different resonators, starting with the 5th and ending with the 18th top resonators, marked as M5 and M18 in Figure 3.1(a). The speaker was placed on the resonator immediately below the microphone and, as a result, it was moved between the bottom resonators marked as S3 and S14 in Figure 3.1(a). For each speaker-microphone configuration, the frequency was scanned from 3200 Hz to 6500 Hz in 25 Hz steps.

For the left edge acoustic measurements reported in Figure 3.6, the same instrumentation was used but the speaker was inserted in the resonator marked as S1 in Figure 3.1(a) and the microphone in the resonator marked as M1 in the same figure. For the right edge acoustic measurements, the speaker was inserted in the resonator marked as S2 in Figure 3.1(a) and the microphone in the resonator marked as M2 in the same figure. For both left and right edges, the frequency was swept from 5.1 kHz to 5.8 kHz in steps of 25 Hz. The measurements were repeated with the relative position of the top row of resonators adjusted in steps of 1 mm.

3.5 Experimental Results

3.5.1 The Numerically Simulated Topological Pumping Process

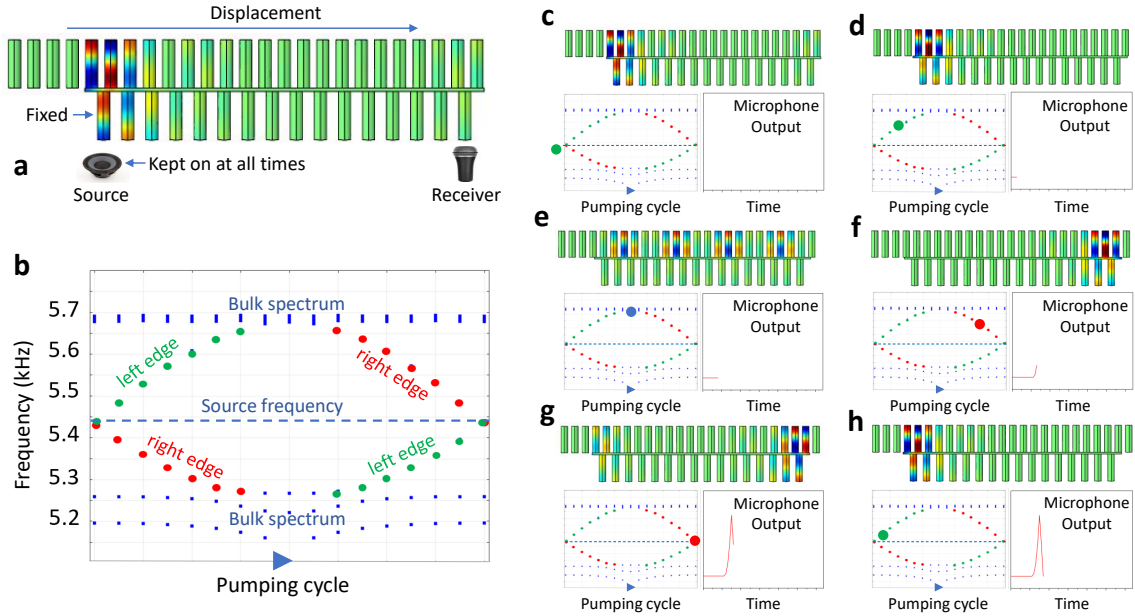


Figure 3.4 (a) The configuration of the system at the beginning of a pumping cycle. The top array is uniformly displaced to the right and, after a total displacement d_2 , the system returns in its original configuration and completes a full pumping cycle. A speaker is inserted in resonator S1 and is kept on at all times, while a microphone is inserted in the resonator M0. (b) Simulation of the resonant spectrum as function of displacement. Chiral left and right edge bands are observed, which both connect two disjoint parts of the bulk spectrum. (c-h) Rendering of pumping mechanism: The left edge mode is loaded when the source frequency matches the mode frequency (c); The mode self-oscillates while its frequency is pushed up (d); The character of the mode changes from left-localized to delocalized (e); The character of the mode changes again from delocalized to right-localized (f); The mode self-oscillates as its frequency is pushed down (g); The cycle repeats itself as the top array is further pushed to the right (h). The microphone starts to pick signal after the event (e). The simulations in panels (c-h) show the spatial profile of the resonant mode highlighted in the sub-panel below it. The shown microphone outputs are not from real measurements. The pumping parameter is φ in all panels.

The numerically simulated topological pumping process is reported in Figure 3.4, where we also explain its mechanism. Sure enough, the left and right chiral edge bands are present in the topological gap. Note their particular and optimal dispersion, which made the dynamical pumping possible. Indeed, it is important that the right chiral edge band emerges from the top bulk-band shortly after the left chiral edge dived into the same band. This is because the non-adiabatic effects cannot be prevented when the pumping of energy

is through the bulk states. As such, one has to optimize the pumping cycle such that there is a rapid change of the mode character from left-localized to extended and to right-localized, exactly as it can be seen in Figure 3.4(c-h), where our pumping cycle was broken down into steps. In a standard topological edge-to-edge pumping, the mode self-oscillates after being loaded at the left edge, hence the pumping cycle must be performed fast enough to overcome dissipation.

3.5.2 Un-assisted Dynamical Energy Pumping via Topological Edge Modes

Given the particular engineering of our system, the pumping cycle can be performed extremely fast and repetitively, even without any external intervention. This enabled us to achieve the first un-assisted dynamical energy pumping via topological edge modes. Its dramatic manifestation is documented in Figure 3.1(g), where a receiver placed opposite to an acoustic source is shown to pick up acoustic signal when the excitation frequency is in a topological resonant gap. In this experiment, 10 resonators were added beyond the edge to the left side of the top array, which resulted in the 10 pumping cycles visible in Figure 3.1(g). The time period of the pumping cycle is approximately 0.12 seconds in Figure 3.1(g). We have experimented with the time period of the cycle and found that the energy transfer is completely cut out when the period is about 1 second. This demonstrates that the pumping process is indeed essential for the energy transfer across the acoustic meta-crystal. Furthermore, when the source frequency is adjusted in a non-topological spectral gap, the receiver picks no signal whatsoever. We have experimented with different source frequencies inside the non-topological gap and we can confirm that the receiver does not pick any signal even when the frequency is very close to the bulk spectrum. This demonstrates that the chiral edge bands, formed inside the topological spectral gap, play an essential role for the energy transfer phenomena detected in our experiments.

The sound of the pumping reported in Figure 3.1(h) As one can see, there is stark difference between the two pumpings reported in Figure 3.1. Taking into account all the

above facts, there can be no doubt that the energy transfer across the meta-crystal was through a classic topological pumping process.

3.5.3 Experimental Mapping of the Bulk and Edge Resonant Spectrum

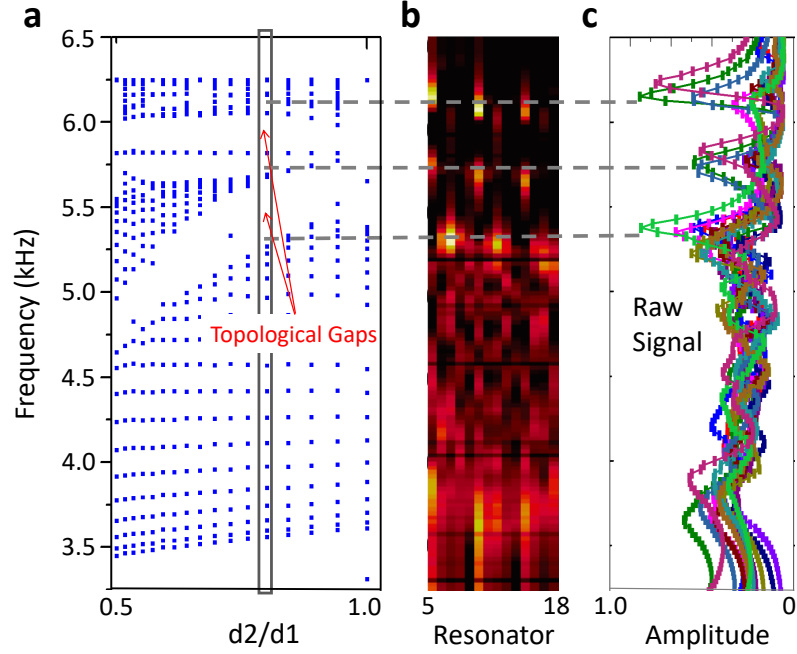


Figure 3.5 (a) Simulated resonant spectrum reproduced from Figure 3.1(e), with arrows indicating the topological gaps. The vertical marking identifies $d_1 = 20$ mm and $d_2 = 16$ mm used in experiments. (b) Measurement of the spaced-resolved density of states. (c) Collapse of the data in panel (b) on the frequency axis. Two spectral gaps can be clearly identified in the experimental data, which are well aligned with the theoretical calculations.

As we already mentioned, the resonator coupling through the spacer does not allow fine-tuning but that is not necessary when using aperiodic principles, as long as the coupling is strong [Apigo et al., 2018]. To understand the mechanism of topological gap generation in our system, we show first in Figure 3.1(d) the evolution of the simulated resonant spectrum with respect to the relative alignment of two identical arrays of resonators. As expected in any 1-dimensional periodic system, gaps appear in the resonant spectrum and, as the system switches between period-one and period-two, some of these spectral gaps close while other remain open. Regardless of that behavior, all these gaps are topologically trivial because the resonant bands seen in Figure 3.1(d) result from dispersion-induced thickening of the

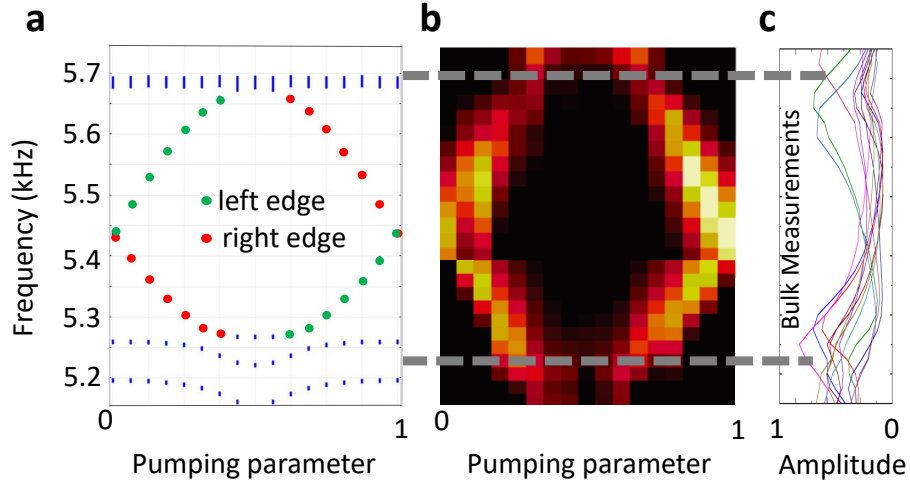


Figure 3.6 (a) Simulated resonant spectrum for the finite acoustic meta-crystal shown in Figure 3.1(a), as function of the pumping parameter. The latter is the ratio between the displacement x , shown in Figure 3.1(c), and d_2 . (b) Experimental measurement of the resonant spectrum as function of the pumping parameter. (c) Bulk-spectrum measurements reproduced from Figure 3.5(c), used here to pin-point the position of the bulk bands shown by dashed lines.

discrete resonances of the individual resonators. However, when the lattice constant of the bottom array is varied and the system becomes aperiodic, these trivial bands are seen in Figure 3.1(e) to become fragmented in sub-bands, exactly as it happens when a magnetic field is turned on a two dimensional electronic system [Hofstadter, 1976]. The dynamical matrix behind the resonant spectrum belongs to an algebra of observables generated by two operators obeying the same commutation relations as the magnetic translations. The conclusion is that the spectrum seen in Figure 3.1(e) is a representation of the Hofstadter butterfly [Hofstadter, 1976]. In particular, the sub-bands carry non-zero Chern numbers [Apigo et al., 2018, Prodan and Shmalo, 2019] and the presence of the chiral edge bands can be explained by the standard bulk-boundary correspondence [Kellendonk et al., 2002, Prodan and Schulz-Baldes, 2016].

The simulated bulk spectrum is reproduced with high fidelity by the experimental measurements, as demonstrated in Figure 3.5. In particular, well defined bulk-spectral gaps can be identified in the measured local density of states, which are well aligned with the theoretical predictions. The frequency 5.4 kHz used for topological pumping

in Figure 3.1(g) falls in the middle of one such gap. Furthermore, the signature of the non-zero Chern numbers, that is, the chiral edge bands, are also detected experimentally, as reported in Figure 3.6. By comparing the panels (a) and (b), one can see that the experiment reproduces the simulations with very high fidelity.

3.5.4 Dynamical Pumping additional experiments

For the dynamic pumping measurements reported in Figure 3.1(g,h), ten additional resonators were added to left side of the top array, which was then pushed to right at an average speed that resulted in approximately one pumping cycle per 0.12 s. The speaker was inserted in the bottom resonator marked as S1 in Figure 3.1(a) and was kept on at all times while the microphone was inserted in the bottom resonator marked as M0 in the same figure. The frequency of the acoustic source was first set at 5400 Hz, which corresponds to a topological gap in Figure 3.4, and then at 3200 Hz, which corresponds to a non-topological gap. A low-high pass filter of 2 kHz bandwidth centered on the driving frequency was applied to the recordings.

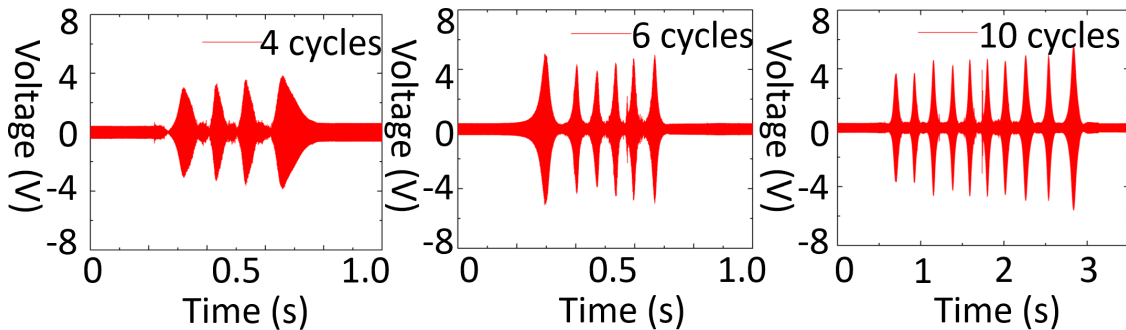


Figure 3.7 Adjusting the number of cycles same as Figure 3.1(g) but with 4, 6 and 10 added resonators.

The number of pumping cycles in our dynamical pumping experiments can be adjusted by changing the number of resonators placed at the left of the top array of resonators. Figure 3.7 reports the microphone output for dynamical pumpings performed with 4, 6 and 10 pumping cycles, demonstrating a perfect correlation between the microphone readings and the adjusted number of cycles.

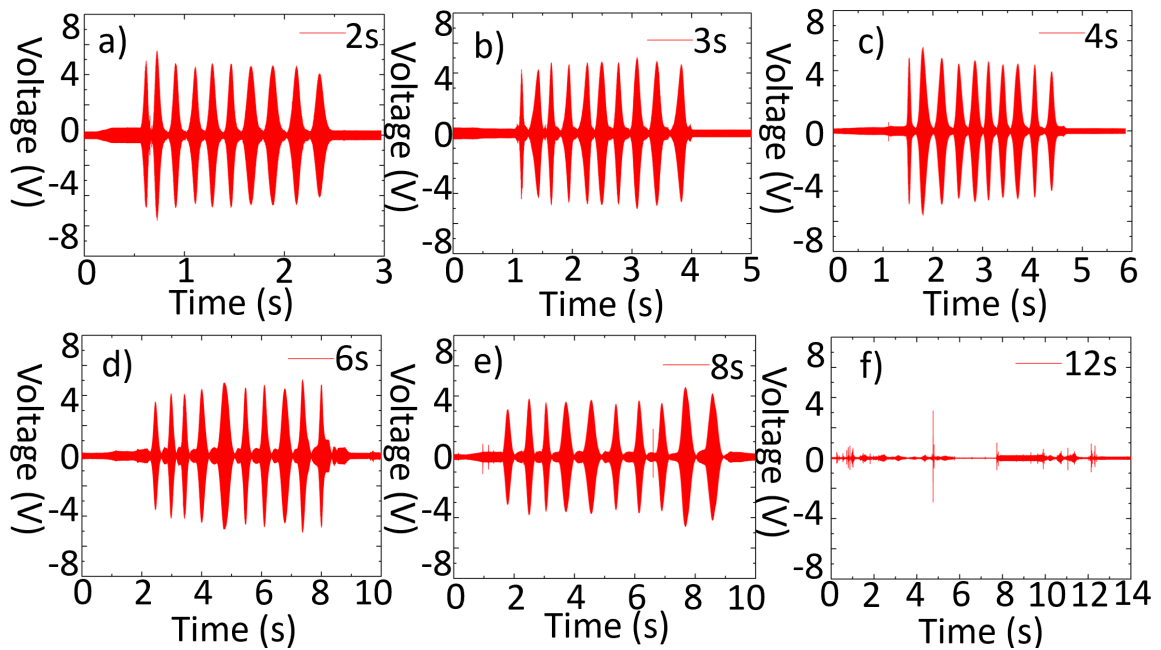


Figure 3.8 Adjusting the pumping cycle speed same as Figure 3.1(g) but for different duration of the total ten cycles.

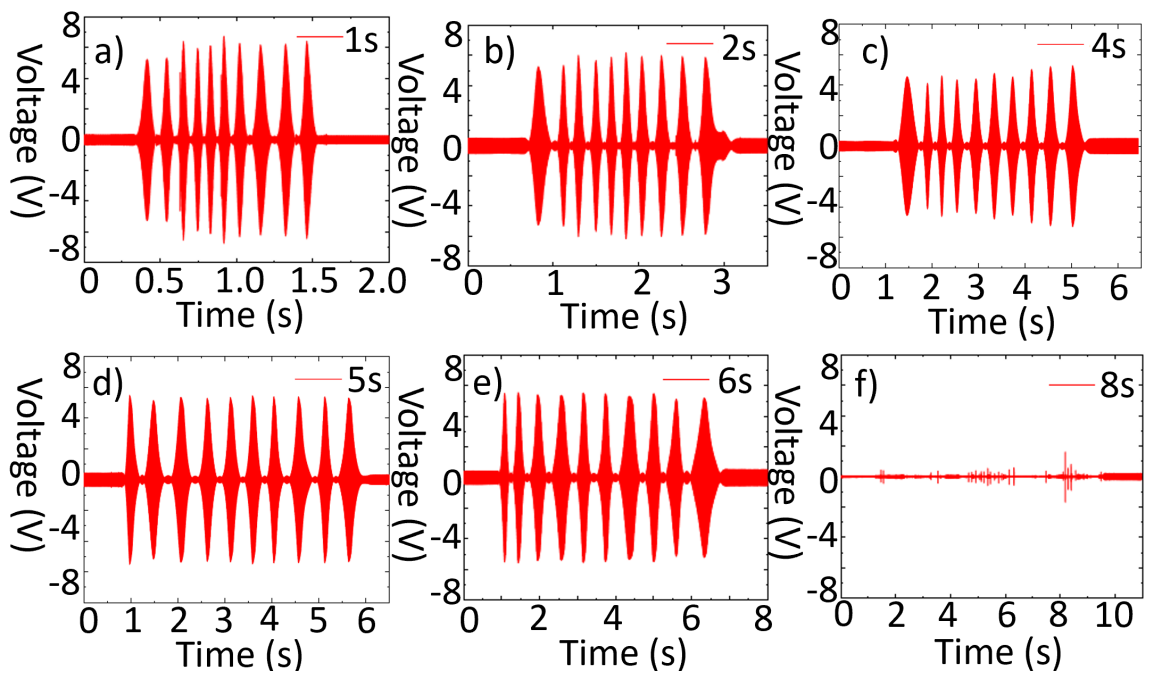


Figure 3.9 Adjusting the length of the meta-crystal same as Figure 3.8 but for a longer meta-crystal which contains five additional resonators at the top and four additional resonators at the bottom.

Keeping the number of resonators fixed, we have adjusted the speed of the adiabatic cycles and the results are reported in Figure 3.8. As one can see, the amplitude of the pumped sound decreases as the speed is decreased and the pumping is fully cut-off when the time period of the pumping is larger than approximately 1 second. This is attributed to dissipation.

We have repeated the experiments reported in Figure 3.8 with a longer meta-crystal and the results are reported in Figure 3.9. As one can see, the speed at which the pumping is cut-off increases with the length of the meta-crystal, an effect which is attributed to a decrease of the Q-factor of the delocalized modes.

3.5.5 Topological Edge Spectrum under Full Phason Cycle

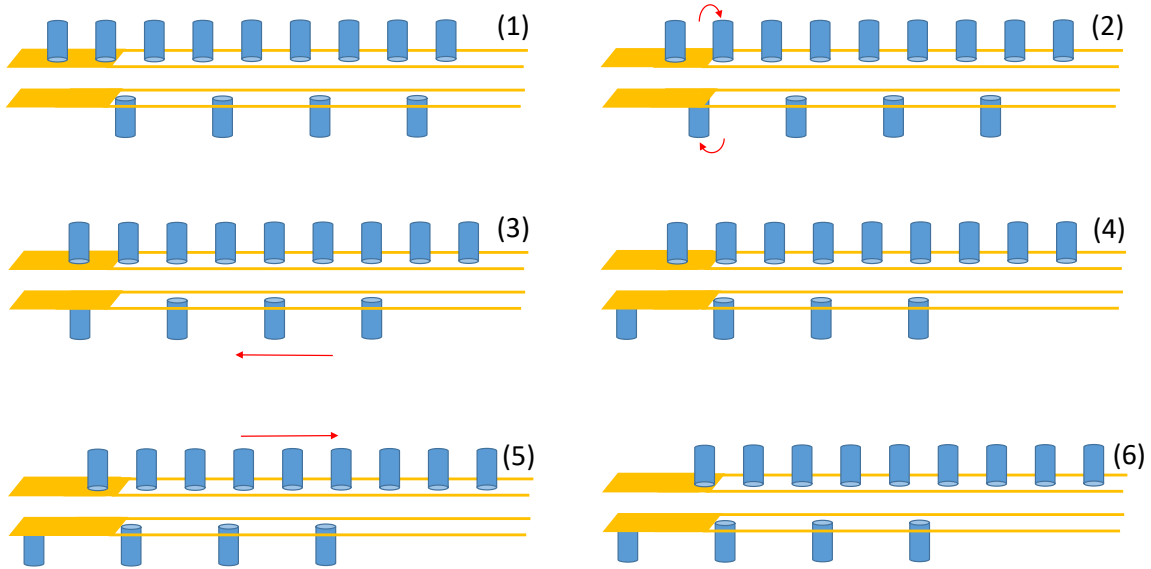


Figure 3.10 Full pumping cycle.

The bulk-boundary correspondence [Kellendonk et al., 2002, Prodan, 2017a] states that the bulk Chern number of a gap equals the number of chiral edge bands traversing that gap when the phason is pumped. Based on the equivalence between the Ω space and the resonator configurations explained above, we produced the physical pumping cycle shown in Figure 3.10, which spends the entire space Ω of the phason. This cycle is more

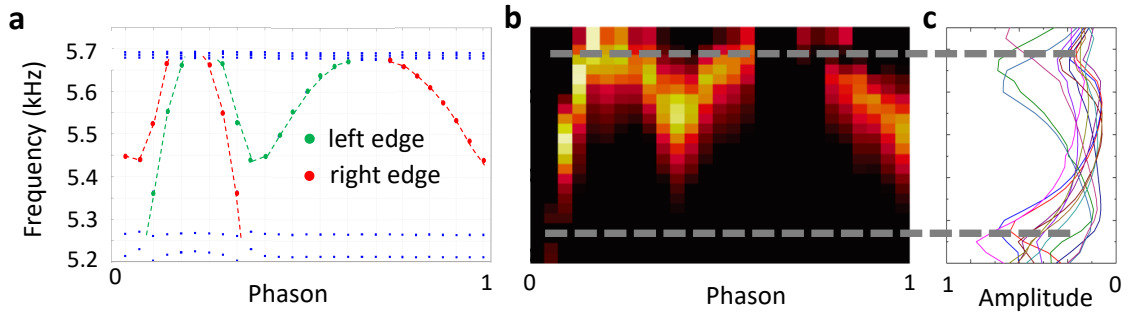


Figure 3.11 (a-c) Same as Figure 3.6 but this time with the phason driven over its full space Ω .

complicated than the cycle shown in Figure 3.4 and involves sliding of both the top and the bottom arrays of resonators. The emergence of chiral bands in a topological gap under this cycle is reported in Figure 3.11. As one can see, the experiment reproduces the simulations with high fidelity. The dispersions seen in Figure 3.11 are relatively complicated when the phason is driven over the entire loop Ω . However, by examining the results in Figure 3.11, we learned that chiral edge bands can be generated by driving the phason on a reduced cycle which involves only the circle of perimeter d_2 . This is the cycle shown in Figure 3.4 and the cycle that was used to achieve the dynamical pumping reported in Figure 3.1.

3.6 Summary

Having demonstrated an un-assisted energy transfer via a topological pumping process, we have laid down a set of specific principles which could facilitate the engineering of the effect in many other contexts. The most important one is that fine-tuning is not necessary which, together with the many different ways of engineering phason spaces [Prodan and Shmalo, 2019], relaxes the design constraints, hence giving scientists better chances with finding optimal and practical meta-structures. While for meta-materials this process is now more or less straightforward, it will be extremely interesting if these aperiodic principles can be successfully applied to mesoscopic systems and achieve electron pumping in conventional insulators.

CHAPTER 4

REVEALING THE WEYL PHYSICS OF THE FOUR-DIMENSIONAL HALL EFFECT VIA PHASON ENGINEERING IN METAMATERIALS

In this chapter, a re-configurable 2-dimensional aperiodic acoustic crystal with a phason living on a 2-torus has been fabricated, giving us access to the 4-dimensional quantum Hall physics. Also, I will supply a direct experimental confirmation that the topological boundary spectrum assembles in a Weyl singularity when mapped as function of the quasi-momenta. I will also demonstrate topological wave steering enabled by the Weyl physics of the three-dimensional boundaries. The work was in collaboration with Prof. Emil Prodan from the Department of Physics at Yeshiva University and Prof. Camelia Prodan from the Department of Physics at New Jersey Institute of Technology.

4.1 Introduction

In 1988, Haldane predicted that quantized Hall physics can be intrinsic to a material [Haldane, 1988]. To generate the effect without an external magnetic field, he had to consider an atomic lattice with at least two degrees of freedom per repeating cell and to rely on complex hopping parameters that break the time-reversal symmetry. Chromium-doped thin films of $(\text{Bi,Sb})_2\text{Te}_3$ produced the experimental validation of Haldane's prediction [Chang et al., 2013b, Chang et al., 2013a]. Two decades after Haldane's seminal work, the quantum Hall physics was predicted to also manifest in systems with electro-magnetic [Haldane and Raghu, 2008] and mechanical [Prodan and Prodan, 2009] degrees of freedom. These predictions became reality in 2009, when confirmed with gyromagnetic photonic crystals [Wang et al., 2009], and in 2015, when confirmed with gyroscope lattices [Nash et al., 2015], respectively. These earlier advances flourished in extremely active fields, where quantum Hall physics is investigated with both quantum materials and classical meta-materials.

Integer quantum Hall effect (IQHE) generalizes in 4-dimensions (4D) and higher, [Zhang and Hu, 2001] and the representative theoretical models that display the effect, intrinsically, have been already enumerated [Ryu et al., 2010] [see also [Prodan and Schulz-Baldes, 2016, Sec. 2.2.4]]. Those representative models assume spatial periodicity and this simplified setting comes at the price of increased complexity in the degrees of freedom per repeating cell. For example, the simplest model in dimension $d = 2n$ requires 2^n degrees of freedom, complex connectivity and a high level of tuning to stabilize a topological phase [Ryu et al., 2010]. One strategy for implementing such higher dimensional models is to see them as supplying labels for and specific connections between the degrees of freedom. As long as these labels and their connections are identically reproduced, the degrees of freedom can be rendered in any dimension, in particular, in our 3-dimensional physical space. Following this strategy, the 4D QHE was recently implemented with classical electric circuit [Wang et al., 2020]. While certainly an impressive demonstration, the outcome was an extremely complex network of connected circuit components.

Starting with the work of [Kraus et al., 2012] a strategy emerged for the emulation of topological effects from higher dimensions. It relies on aperiodicity, specifically, on the fact that any aperiodic pattern has an intrinsic degree of freedom, the phason, which, at least in principle, can be engineered, accessed and controlled experimentally. [Apigo et al., 2018, Prodan and Shmalo, 2019] The phason space augments the physical space and this opens a door to higher dimensional physics. Certainly, the experimental emulations of the 4D QHE were based on these principles. [Lohse et al., 2018, Zilberberg et al., 2018] Working with ultracold atoms, [Lohse et al., 2018] were able to map a cloud's center of mass as it navigated an aperiodically modulated potential and to demonstrate the quantization of the bulk topological invariant via a connection established in an earlier theoretical work. [Price et al., 2015] The bulk-boundary correspondence was not addressed in this study. [Zilberberg et al., 2018] emulated the 4D QHE with spatially modulated arrays of coupled optical wave guides and produced evidence of topological boundary modes. Due to the specific physics

involved, the analysis rested entirely on the spatial profile of the modes and their actual energies were not resolved. As such, no evidence of the hallmark Weyl singularity in the dispersion of the boundary modes was presented, predicted by the *strong* bulk-boundary correspondence of 4D QHE [Ryu et al., 2010]. Instead, other weaker forms of bulk-boundary correspondence were presented, such as the corner-to-corner pumping.

These three works [Lohse et al., 2018, Zilberberg et al., 2018, Wang et al., 2020] are the only experimental emulations of the 4D QHE to date, and many aspects related to the effect remained un-confirmed. Certainly, an experimental setup where both the spatial and frequency domains can be simultaneously resolved is missing. Even with the aperiodic principles at hand, the designs remained challenging, perhaps because it is falsely assumed that the models need to simulate the Hofstadter Hamiltonians as close as possible. However, as pointed out by [Apigo et al., 2018] no fine tuning is actually necessary to open topological gaps. The latter only require strong aperiodicity and strong couplings between the resonators, as well as a reliable strategy for the phason engineering that produces the desired topological phases. [Prodan and Shmalo, 2019] Guided by these principles, we demonstrate here a robust design of a quasi-periodic 2D acoustic crystal that hosts the 4D quantum Hall physics. Reconfigurability and other advantages of the experimental setup enables us to map, the Weyl singularity predicted by the bulk-boundary correspondence. [Prodan and Schulz-Baldes, 2016] Furthermore, we demonstrate ways to control and steer the boundary modes using the phason, that are specific only to 4D QHE.

All the above rely on the concept of phason engineering. Using this strategy, the Hall physics from an arbitrarily high dimension can be access from a physical space of lower dimension $d = 1, 2, 3$. The high throughput of large classes of topological models produced by phason engineering will be essential for our understanding of higher-dimensional bulk-boundary correspondence, of its manifestation in meta-materials and of its possible applications. Phason engineering relies on a specialized algorithm to position the resonators relative to each other to produce phasons that live on arbitrary

d' -dimensional tori. Regardless of the particular couplings of the resonators, the dynamical matrices that determine the collective resonant spectrum of the crystal are Galilean invariant. We show that any such Galilean invariant dynamical matrix is just linear combinations and products of elementary operators that satisfy the commutation relations of the magnetic translations in $(d + d')$ -dimensions. As such, the spectral gaps of the crystals carry higher Chern numbers and they display a bulk-boundary correspondence specific to IQHE in higher dimensions. [Prodan and Schulz-Baldes, 2016] Furthermore, to navigate the complex topology of the states, we devise a K-theoretic visual method to map the large number of topological invariants associated with the bulk gaps, based on the gap labeling technique. [Bellissard, 1986, Bellissard, 1992].

4.2 Experimental Set-up and Results

Our experimental set-up and main results are summarized in Figure 4.1. Photographs of our acoustic crystal can be seen in Figure 4.1(a,b). It consists of identical cylindrical resonators with a geometry specified in Figure 4.1(c). The geometry was chosen to accommodate the microphone and the speaker used for the measurements (see Methods), as well as to ensure a good separation of the discrete resonant modes, in the frequency domain we are interested in. The latter ensures that only basic mode-to-mode couplings occur. Figure 4.1(c) also shows the domain of the acoustic wave propagation and, as one can see, the resonators are connected through a thin domain, which we call the spacer. It is highlighted in red in Figure 4.1(a). By filling this spacer with solid material, we can confine the wave propagation and create a re-configurable boundary, highlighted in red in Figure 4.1(b), to control the phason as explained below. It is important to acknowledge that the use of a spacer as a solution for resonator coupling, and not other complicated means such as bridges, is one of the keys to our results. The spacer, certainly, does not allow any fine tuning but it does enable strong coupling, hence it is of crucial importance that accessing the 4D Hall physics does not rely on fine tuning. [Apigo et al., 2018] Let us specify that, in order to tightly pack

the resonators and increase the strength of the coupling, the nearest neighboring resonators have been placed on opposite sides of the spacer.

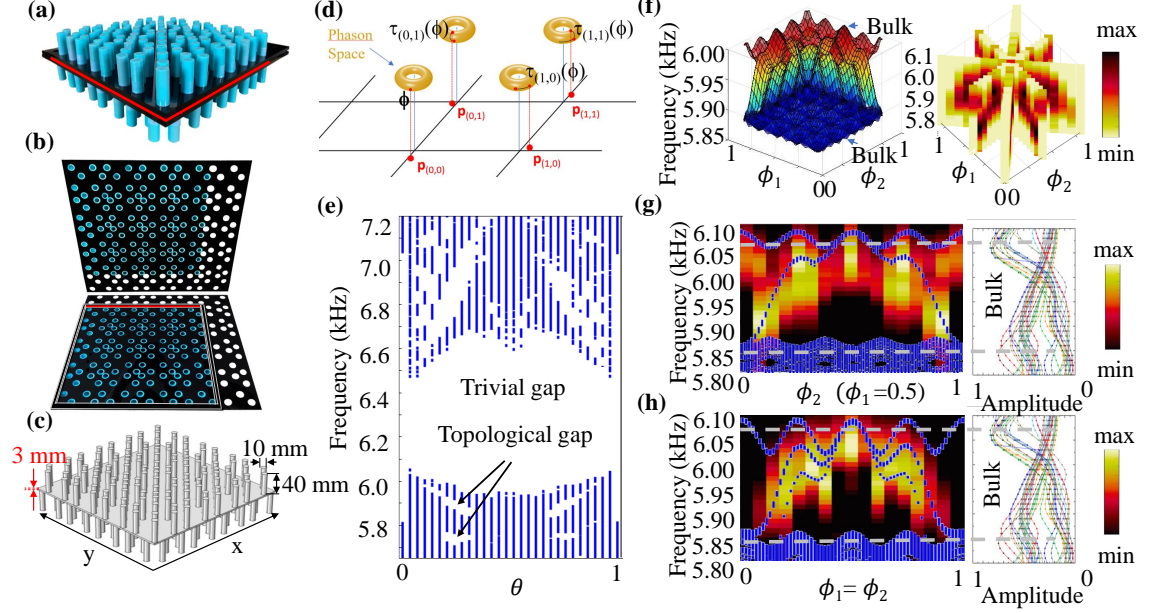


Figure 4.1 (a) Photograph of a fully assembled acoustic 2D sinusoidal pattern consisting of top/bottom cylindrical resonators. The middle red bar indicates the presence of an inner chamber, which connects the top and bottom resonators and is referred to as the spacer. (b) Photograph of the inner structure, with the spacer now fully visible. (c) The wave propagation domain. (d) Illustration of the algorithm which supplies the position of the resonators. (e) COMSOL simulated bulk resonant spectrum against θ , together with labels for the topological and non-topological gaps. (f) Left: COMSOL simulated resonant spectrum for hard wall termination, shown against the phason parameters ϕ_1 and ϕ_2 . The Weyl singularity is the spectral surface connecting the the indicated bulk bands. Right: Experimental measurement of the density of states, with the phason space sampled in several directions. (g,h) Comparison between the experimentally measured density of states and the simulated spectrum (blue dots) for the traces $\phi_1 = 0.5$ and $\phi_1 = \phi_2$, respectively. The theoretical spectra have been stretched by a small factor to overlay the experimental data. The bright dispersive modes in the left side are part of the spectral dome. The right side displays the raw density of states data for the bulk, from where we read the edges of the bulk gap.

The resonators are labeled by $\mathbf{n} = (n_1, n_2) \in \mathbb{Z}^2$ and the (x, y) -coordinates of their centers $\mathbf{p}_{\mathbf{n}}$ are such that

$$\begin{aligned} \mathbf{p}_{\mathbf{n}+(1,0)} &= \mathbf{p}_{\mathbf{n}} + D \left(1 + \epsilon \sin \left(2\pi(\phi_1 + n_1\theta) \right), 0 \right), \\ \mathbf{p}_{\mathbf{n}+(0,1)} &= \mathbf{p}_{\mathbf{n}} + D \left(0, 1 + \epsilon \sin \left(2\pi(\phi_2 + n_2\theta) \right) \right), \end{aligned} \quad (4.1)$$

with $D = 17.0$ mm and $\epsilon = 0.4$. This pattern can be thought as a strongly perturbed ideal lattice with the perturbation produced dynamically, via the specialized algorithm illustrated in Figure 4.1(d) and explained below. Note that the pattern depends on the phason $\phi = (\phi_1, \phi_2)$, which lives on a 2-torus. We place the boundaries along the horizontal axis $x = -D/2$ and vertical axis $y = -D/2$, hence in between the rows and columns of the ideal lattice. Now, if we keep the pattern in place and we move the boundaries at $x = (m_1 - \frac{1}{2})D$ and $y = (m_2 - \frac{1}{2})D$, then this move has the same effect as changing the phason as $\phi \mapsto (\phi_1 + m_1\theta, \phi_2 + m_2\theta)$. As such, by having an adjustable boundary, we can sample the phason space with just one acoustic crystal. In the actual experiments, we used four different acoustic crystals together with the mobile boundary technique to sample 16×16 points of the phason space. Let us acknowledge that Equation (4.1) is just one example of a large class of patterns generated with the specialized algorithm illustrated in Figure 4.1(d), which give access to the 4D quantum Hall physics (see Phason engineering).

The resonant spectrum of the acoustic crystal, as computed with the finite-element based software COMSOL, is reported in Figure 4.1(e) as function of θ . Since the simulations were for a finite crystal, some of the bulk gaps are contaminated by boundary spectrum. Additional model calculations with periodic boundary conditions for larger crystals are reported in Figure 4.2.

The simplest model for the dynamical matrix assumes a coupling through isotropic evanescent tails of the discrete modes supported by the individual resonators. In this case, the overlap coefficients depend only on the distance between the resonators and this dependence is exponentially decaying with the distance. In other words,

$$D_{\mathbb{P}} = \sum_{\mathbf{x}, \mathbf{y} \in \mathbb{P}} e^{-|\mathbf{x}-\mathbf{y}|/\Lambda} |\mathbf{x}\rangle\langle\mathbf{y}|. \quad (4.2)$$

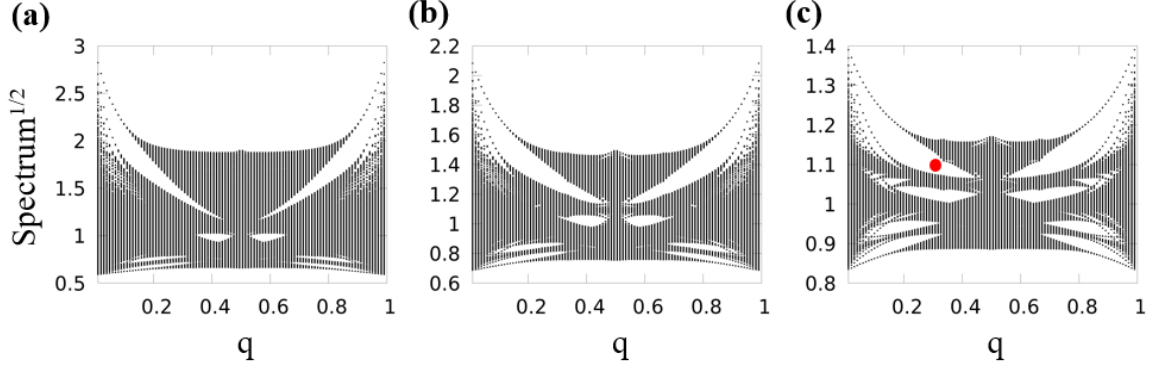


Figure 4.2 Square root of the spectrum of the dynamical matrix Equation (4.2) with (a) $\Lambda = 3D/4$, (b) $\Lambda = D/5$, and (c) $\Lambda = D/3$. The spectrum in panel (c) reproduces qualitatively the resonant spectrum of the experimental crystal.

The parameter Λ relates to the exponential decay of the evanescent modes and is left as an adjustable parameter.

Figure 4.2 reports the spectrum of this dynamical matrix with \mathbb{P} fixed to the pattern of resonators in our experiments and for three values of Λ . As one can see, while the quantitative details of the spectrum change drastically from one graph to another, a group of bulk gaps can be consistently identified in all panels of Figure 4.2, in particular, the top left gap. Furthermore, for $\Lambda = D/3$, the large gaps seen in the spectrum looks qualitatively the same as the spectrum reported in Figure 4.1(e). Therefore, we conclude with great confidence that this model calculations can be used to map the topological invariants. In particular, the spectral gap marked by the red dot can be identified with the spectral gap identified by our experiments.

At $\theta = 0$, the crystal is periodic and, as expected, the spectrum contains bands that evolve from the discrete modes of the individual resonators. These bands don't share any dynamical features, hence the spectral gaps separating them are all trivial [see the label in

Figure 4.1(e)]. As the parameter θ is turned on, the bands of spectrum become fragmented and a large number of spectral gaps develop. Qualitatively, the spectra resembles the Hofstadter butterfly [Hofstadter, 1976] and, as we shall see below, the spectral gaps carry 2^{nd} and 1^{st} Chern numbers.

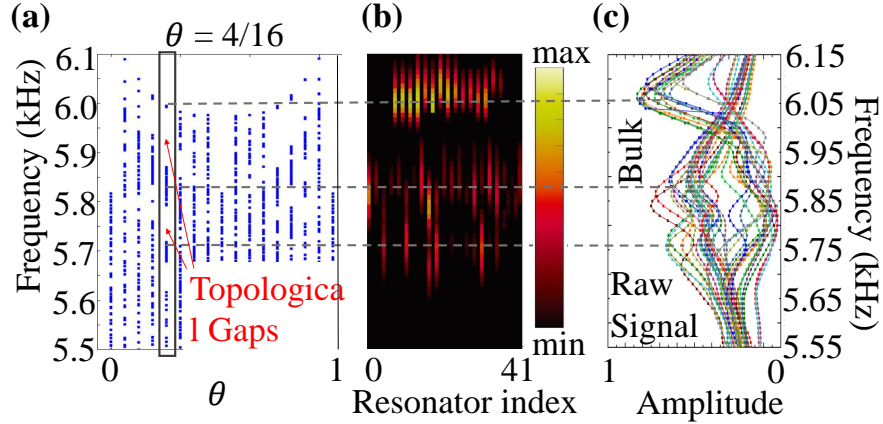


Figure 4.3 (a) COMSOL simulated resonant spectrum for the experimental set-up from Figure 4.1, with arrows indicating the topological gaps. The vertical box identifies $\theta = 0.25$, used in experiments. (b) Measured local density of states, assembled from microphone readings on 42 bulk resonators. (c) Collapse on the frequency axis of the intensity plot reported in panel (b). Two spectral gaps can be clearly identified and seen to be well aligned with the theoretical predictions.

Experimentally, we were able to reproduce with high fidelity the predicted spectra from Figure 4.1(e), as demonstrated in Figure 4.3. Specifically, in Figure 4.3(b), we report the measured local density of states of the crystal, resolved by frequency and resonator index. The data is collapsed on the frequency axis in Figure 4.3(c) and two clear spectral gaps are identified, which are well aligned with the ones in the COMSOL simulated spectrum, shown again in Figure 4.3(a). The resonant spectrum in Figure 4.3(a) does not depend on ϕ_1 and ϕ_2 . In the following, we fix θ at the value identified in Figure 4.3(a) and work with the first bulk gap, counted from the top, which as we shall see, carries a 2^{nd} Chern number $\text{Ch}_2 = -1$.

In Figure 4.1(f), we report on the right the resonant spectrum of a finite crystal as function of ϕ , as computed with COMSOL in a finite frequency domain that covers the

bulk gap identified above. The dominant feature connecting the indicated bulk bands of spectrum is a spectral dome that is hollow inside. A point inside this dome has no escape path since it is completely surrounded by spectrum. Furthermore, using model calculations, we observed that this dome does not disappear or open up under continuous deformations of the crystal. These indicate that the dome has a built in topological protection, which we will associate with the 2nd Chern bulk number and with the Weyl physics expected at the surface of a 4D IQHE system. Let us state that we were able to experimentally reproduce with high fidelity this spectral dome. Indeed, the right side of Figure 4.1(f) reports the experimentally measured density of states, with the phason space sampled in several directions and, as one can see, the outcome reproduces the spectral dome. In Figure 4.1(g,h) we report two sections of these measurements showing quantitative agreement with the COMSOL simulations. The Weyl singularity is further analyzed in Figure 4.5. In particular, it is shown there that the modes associated to that part of the spectrum are localized on the boundary. Experimental measurements of the spatial profiles of these modes, confirming the boundary location, are reported in Figure 4.4.

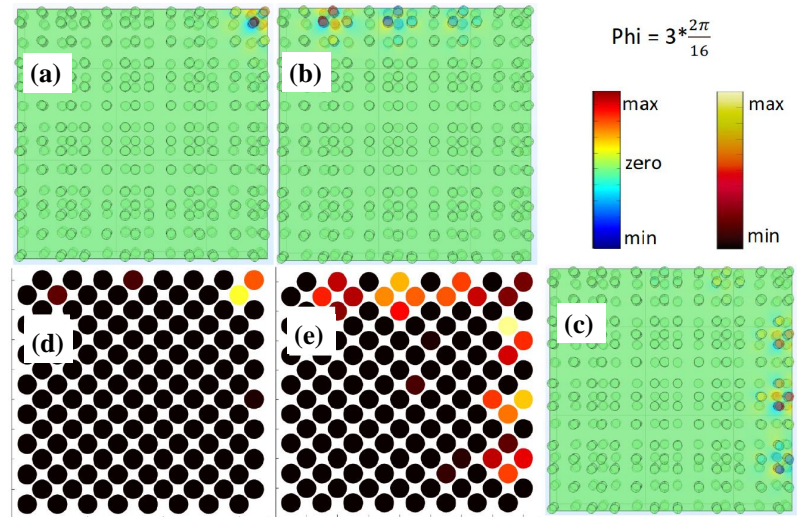


Figure 4.4 Profiles of the edge and corner modes for $\phi_x = \phi_y = 3/16$. (a) Comsol simulation shows the pressure distribution of a corner mode. (b)-(c) Comsol simulation shows the pressure distribution for 2 edge modes. (d) Experimental verification of the corner mode in (a), (e) Experimental verification of the 2 edge modes in (b)-(c).

In panels **d** and **e** of Figure 4.4, we show the experimentally measured local density of states, mapped at the resonant frequencies corresponding to the modes in panels **a**, **b** and **c**. The frequencies of the modes in panels **b** and **c** are too close to be resolved experimentally. Nevertheless, the experimental density of states resembles quite closely the overlap of the two edge modes detected by simulations. Similarly for the corner mode. This remarkable resemblance between simulations and measurements has been observed throughout and, to simplify and speed up our measurements, cues from the COMSOL simulations were used to identify the regions where the pressure field is negligible. These regions were not measured when assembling the data in Figures. 4.1 and 4.3.

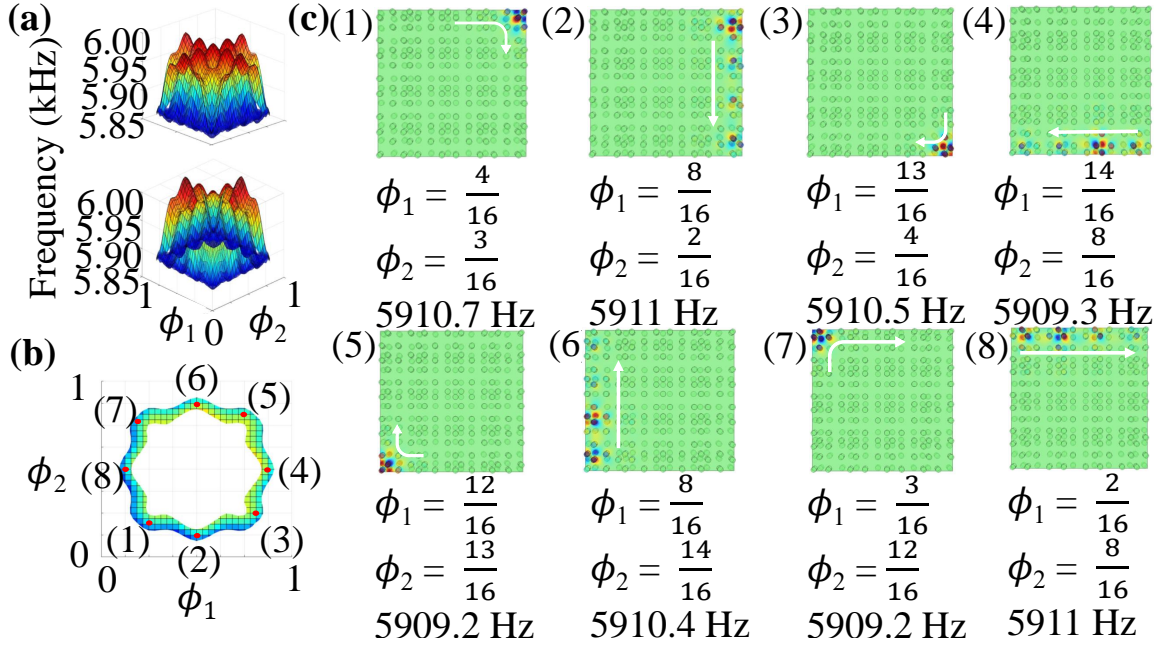


Figure 4.5 Weyl singularity and mode steering. (a) COMSOL simulated spectrum as function of the phason $\phi = (\phi_1, \phi_2)$, revealing the Weyl singularity. (b) Cross-section of the Weyl singularity at 5910 Hz. (c) Acoustic pressure field distribution for the eight phasons marked in panel (b), revealing circular mode steering around the crystal's boundary.

The exactly solved 4D IQHE model in [Prodan and Schulz-Baldes, 2016, Sec. 2.2.4,] was isotropic in all four dimensions and, in the presence of a flat boundary, the dispersion was found to display a Weyl singularity $E(\vec{k}_{\parallel}) = \pm \|\vec{k}_{\parallel} - \vec{k}_0\|$, where \vec{k}_{\parallel} are the three quasi-momenta parallel to the boundary and \vec{k}_0 is the coordinate of the Weyl singularity.

Our acoustic crystal is highly isotropic and the Weyl singularity for a flat boundary is collapsed, in the sense that the boundary spectrum displays dispersion only with respect to ϕ_1 if the boundary is cut perpendicular to the first spatial direction. Nevertheless, the Weyl physics of the boundary is still encoded (see [Prodan and Schulz-Baldes, 2016, Example 5.3.3]) in the boundary topological invariant supplied by the three-dimensional winding number of the gap unitary operator $U_G(\phi) = e^{i2\pi g(D_\phi)}$, where D_ϕ is the dynamical matrix of the crystal with a boundary and g is any continuous real valued function taking 0/1 value above/below the bulk gap. By construction, the spectral decomposition of $U_G - I$ involves only the boundary modes that are spatially localized at the edges of the sample. Now, our sample has four edges instead of just a flat one, hence, for the sake of the argument, it is more appropriate to consider a disk-shaped sample of very large radius R . Then the winding number is computed using the variables ϕ_1, ϕ_2 and the momentum k_{\parallel} parallel to boundary, with the latter treated with the real-space methods. [Prodan, 2017b] Specifically, the derivation $\partial_{k_{\parallel}}(\cdot)$ is replaced by the commutator $i[\cdot, R\hat{\phi}_3]$ and $\int dk_{\parallel}(\cdot)$ is replaced by $\frac{1}{2\pi R}\text{Tr}(\cdot)$, where $\hat{\phi}_3$ is the operator corresponding to the polar angle in the plane of the sample. The radius R cancels out and the 3D winding number takes the form

$$W_3(U_G) = \Lambda_3 \sum_{\sigma \in \mathbb{S}_3} (-1)^\sigma \int d^3\phi \prod_j U_G^{-1} \partial_{\sigma_j} U_G, \quad (4.3)$$

where Λ_3 is the standard normalization constant and \mathbb{S} is the group of permutation of three objects. The bulk-boundary correspondence [Prodan and Schulz-Baldes, 2016, Sec. 5.5,] assures that this boundary invariant equals the 2nd Chern number of the bulk gap projection and, as such, a Weyl singularity is expected if the modes are resolved by ϕ_j 's. The dome observed in Figure 4.1(f) carries the boundary invariant Equation(4.3) and, for this reason, we proclaim that this spectral feature is the manifestation of the Weyl physics expected at the boundary of a 4D IQHE system. In particular, the spectral dome cannot open in any

spatial direction. Such feature is expected for more general boundaries and we have verified this statement for a sample shaped like an octagon (see Figure 4.7).

In [Zilberberg et al., 2018] light was injected in a corner of the ensemble of modulated wave guides and light was observed coming out at the opposite corner. It was inferred that their observation is equivalent to adiabatic pumping along the cycle mapped in Figure 4.1(h) (see also [Petrides and Zilberberg, 2020]). We were indeed able to reproduce this interesting corner-to-corner pumping effect in Figure 4.6. This Figure reports COMSOL simulations of the resonant modes as the phason ϕ was varied along the diagonal $\phi_1 = \phi_2$ of the phason space. The simulations reveal acoustic pumping from one corner of the modulated crystal to the opposite corner. The pumping starts with the configuration of the system for $\phi_1 = \phi_2 = 3/16$. A frequency of 5886 Hz is loaded into the right upper corner (point (1) in panel a)). A change in the configuration to $\phi_1 = \phi_2 = 5/16$ shifts the frequency to 5930 Hz (point (2) in panel a)). As ϕ continuously changes towards $\phi = 0.5$, the corner modes touch the upper bulk band and they disperse over the whole system. The frequency now is 5992 Hz (point (3) in panel a)). As the phason is changed to $\phi_1 = \phi_2 = 11/16$ then $\phi_1 = \phi_2 = 13/16$, the corner modes concentrates to the lower left corner, and the frequency shifts to 5931 and 5885 respectively (point (4) and (5) in panel a)).

But let us point out that this type of pumping occurs through the bulk states. In an actual pumping experiment, this will inherently lead to leakage into the bulk modes. As discussed in the previous section, the boundary spectrum displays an extra structure near the corners of the phason space. This extra-structure shows up as a second spectral band in the simulated spectrum along the diagonal, reported in Figure 4.1h. In Figure 4.6, these bands can also be easily separated, as discussed above. In Figure 4.4, we illustrate the spatial profiles of the modes from Figure 4.6 appearing at $\phi_1 = \phi_2 = 3/16$, hence for the data in the column corresponding to (1). The spatial profiles of the three resonant modes observed in that column are simulated in panels **a**, **b** and **c** of Figure 4.4. We observe that two of these modes are edge modes while the remaining one is a corner mode. This clear

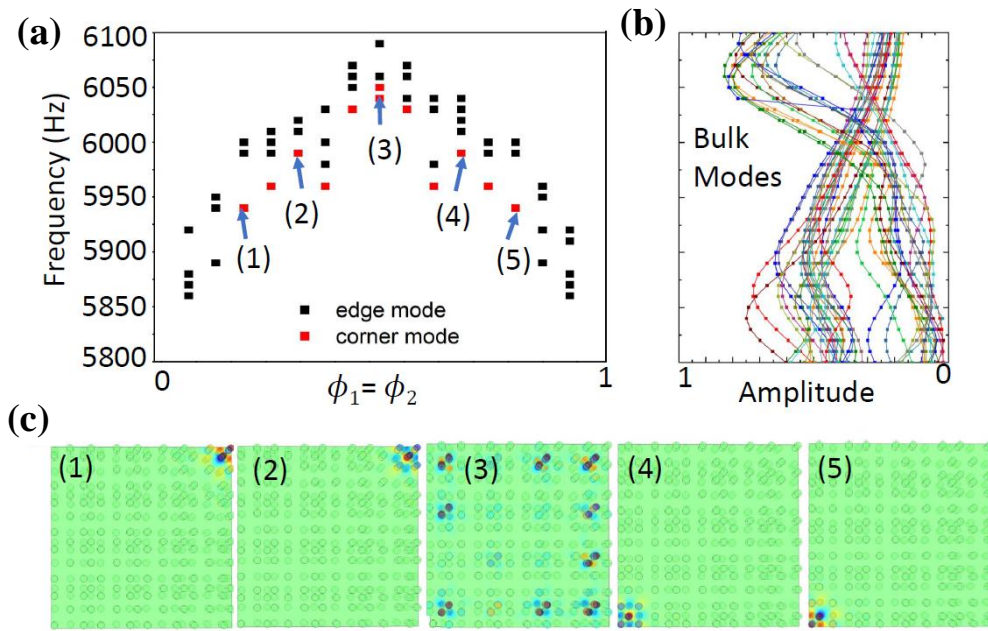


Figure 4.6 Consol simulations of corner to corner pumping. (a) Evolution of the resonant spectrum inside the topological bulk gap along the trajectory $\phi_x = \phi_y$, with the modes localized along an edge and in a corner modes separated out; (b) Experimentally measured bulk response shown as a reference for revealing the upper and lower bulk bands for the gap in panel (a); (c) Pressure distribution of modes (1)-(5) from panel (a), revealing corner-to-corner pumping via the bulk.

separation by mode localization applies throughout the spectrum reported in Figure 4.6. The band corresponding to the corner localized modes is part of the Weyl singularity, hence they originate from the 2nd Chern number. The bands corresponding to the edge localized modes are not part of the Weyl singularity and they originate from weak 1st Chern numbers.

The Weyl singularity, however, gives access to additional pumping cycles that avoid the bulk spectrum. Indeed, one of the special features of a strong topological invariant, such as the 2nd Chern number, is that boundary modes occur regardless of the orientation of the boundary. This feature, together with the full control over the phason, enable a corner-to-corner mode steering that does not proceed through the bulk states but rather goes around the Weyl singularity, as well as around the edges of the sample. The effect is illustrated in Figure 4.5, where a section of the Weyl singularity was sampled at eight points in Figure 4.5(b) and the spatial profiles of the corresponding eigenmodes were mapped in Figure 4.5(c). As one can see, the mode is steered around the boundary of the crystal and completes a full cycle as the phason is cycled over the section of the Weyl singularity.

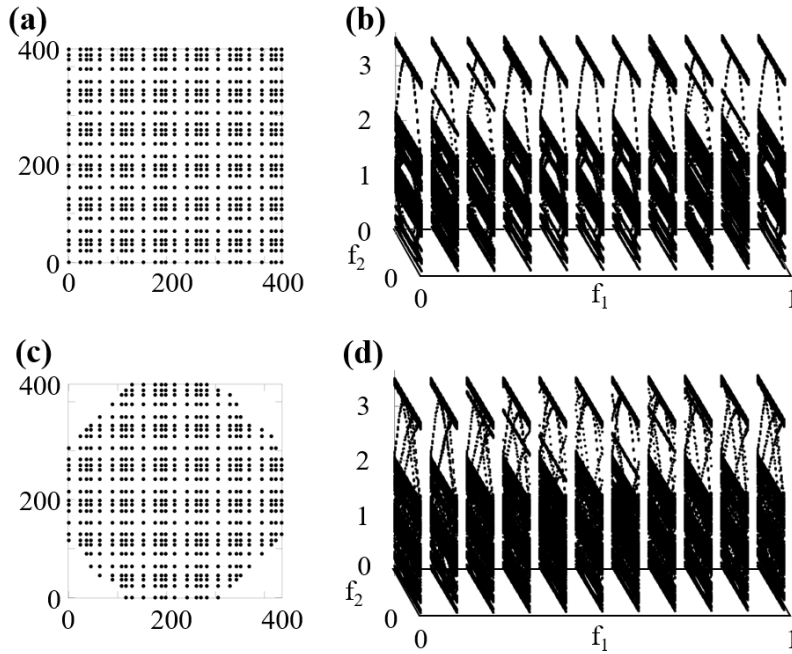


Figure 4.7 Stability of the spectral dome. (a) A crystal cut as a square and (b) its resonant energy spectrum. (c) A crystal cut as an octagon and (d) its resonant energy spectrum. In both cases, the spectra have been resolved by ϕ_1 and ϕ_2 and a spectral dome can be clearly identified. The spectra were computed with the model (c) from Figure 4.8.

4.3 Methods

4.3.1 Fabrication

Our fabrication process is modular and the acoustic crystals are assembled from parts that are independently manufactured with different automated process. This approach enables a high throughput of acoustic crystals, which can be dis-assembled and stored after use.

One leg of the process is the manufacturing of the supporting bases, which are x-mm thick acrylic plates with through holes, laser-cut with the Boss Laser-1630 Laser Engraver. A specialized piece of computer code communicates the pattern (4.6) and the radius of the holes to the machine, hence different phason designs can be efficiently implemented. The nominal tolerance of the laser-cutter is 250 μm .

The resonators were manufactured using an Anycubic Photon 3D printer, which uses UV resin and has 47 μm XY-resolution and 10 μm Z-resolution. The thickness of their walls is 2 mm, to ensure a good quality factor and to justify rigid boundaries in our numerical simulations. The inner dimensions of the resonators are supplied in Figure 4.1. Identical resonators were printed in large quantities and were made ready for the assembling.

The resonators were pushed through the holes of the base plates until flushed with the opposite side of the acrylic plates. After the top and bottom parts were fully assembled, they were pressed against the spacer, which is a 3 mm thick acrylic plate with a large opening cut out to accommodate a total of 16×16 resonators. Let us specify that top and bottom parts accommodate a total of 23×23 resonators, such that spacer can be moved around and generate crystals with different phasons.

4.3.2 Experimental Protocols

The protocol for the acoustic bulk and edge measurements reported in Figure 4.1 h and Figure 4.3 was as follows: Sinusoidal signals of duration 1 s and amplitude of 0.5 V were produced with a Rigol DG 1022 function generator and applied on a speaker placed in a porthole opened in a resonator of the bottom row. A dbx RTA-M Reference Microphone

with a Phantom Power was inserted in a porthole opened in a resonator of the top row and acquired the acoustic signals. To account for the frequency-dependent response of the components, several separate measurements were performed with the structure removed but speaker and microphone kept at the same positions. All our microphone readings are normalized by these reference measurements. The signals were read by a custom LabVIEW code via National Instruments USB-6122 data acquisition box and the data was stored on a computer for graphic renderings.

The local density of states reported in Figure 4.3(b) was acquired with the above protocol, which was repeated for 42 resonators located away from the boundary. For each resonator, the frequency was swept over the shown range of frequency. According to the acoustic pressure field distribution of the upper and lower body modes of the topological gap in the COMSOL simulation, the microphones was placed on 42 different resonators with measurable acoustic pressure. The speaker was placed on the nearest resonator immediately below the microphone and, as a result, it was moved between the bottom resonators.

The density of states reported in Figure 4.1 (g) and (h) was obtain by integrating the local density of states acquired from resonators close to the boundary. Same instrumentation was used but the microphone was inserted in the resonator along the boundary according to the acoustic pressure distribution of the edge modes in the COMSOL simulation, and the speaker was placed on the nearest resonator immediately above the microphone. In Figure 4.1 (g), from 0 to 0.5, the acoustic pressure field distribution of the edge mode is concentrated on the right and upper boundary, and from 0.5 to 1, the acoustic pressure field distribution of the edge mode is concentrated on the left and lower boundary. In Figure 4.1 (h), from 0 to 0.5, the acoustic pressure field distribution of the edge mode is concentrated on the right and upper boundary and upper right corner, and from 0.5 to 1, the acoustic pressure field distribution of the edge mode is concentrated on the left and lower boundary and lower left corner. The measurements were repeated with the change of phason in steps of $1/16$. For each measurement, the frequency was scanned from 5800 Hz to 6100 Hz in

10 Hz steps. The full map of the density of states reported in Figure 4.1 (f) was obtained by the assembling the data from Figure 4.1 (g) and (h) and symmetry considerations to fill in the data for the two additional directions shown in Figure 4.1 (f).

4.4 Simulation

The simulations reported in Figures 4.1, 4.3 and 4.5 were performed with the COMSOL Multiphysics pressure acoustic module. The domain shown in Figure 4.1c was filled with air with a mass density 1.3 kg/m^3 and the sound's speed was fixed at 343 m/s , appropriate for room temperature. Because of the huge acoustic impedance mismatch compared with air, the 3D printing UV resin material was considered as hard boundary.

The spectra reported in Figure 4.8 were computed with the stated model dynamical matrices, which were coded in Fortran and exactly diagonalized using the standard LAPACK library. The simulations assumed 101×101 resonators and θ was sampled as $n/101$ for panels (a,c) and as $\sqrt{2}n/101$ for panel (b), $n = \overline{1, 101}$. This particular sampling enabled us to impose boundary conditions.

4.5 Phason Engineering

We show here that, by using a specialized algorithm to position the resonators relative to each other, we can engineer phasons that live on arbitrary d' -dimensional tori. The algorithm starts from a Bravais lattice \mathbb{L} , generated by acting on the origin \mathbf{p}_0 of the physical space \mathbb{R}^d ($d = 1, 2, 3$) with an abelian group of discrete translations

$$\mathbf{t}_{\mathbf{n}}\mathbf{x} = \mathbf{x} + \sum n_i \mathbf{a}_i, \quad \mathbf{n} = (n_1, \dots, n_d) \in \mathbb{Z}^d. \quad (4.4)$$

The second ingredient is a virtual space $\mathbb{R}^{d'}$ with $d' \geq d$ and with \mathbb{R}^d canonically embedded in $\mathbb{R}^{d'}$. Lastly, \mathbb{L}' is an independent Bravais lattice inside the virtual space $\mathbb{R}^{d'}$, generated by \mathbf{a}'_j , $j = \overline{1, d'}$. With these ingredients in hand, we are going to produce a topologically

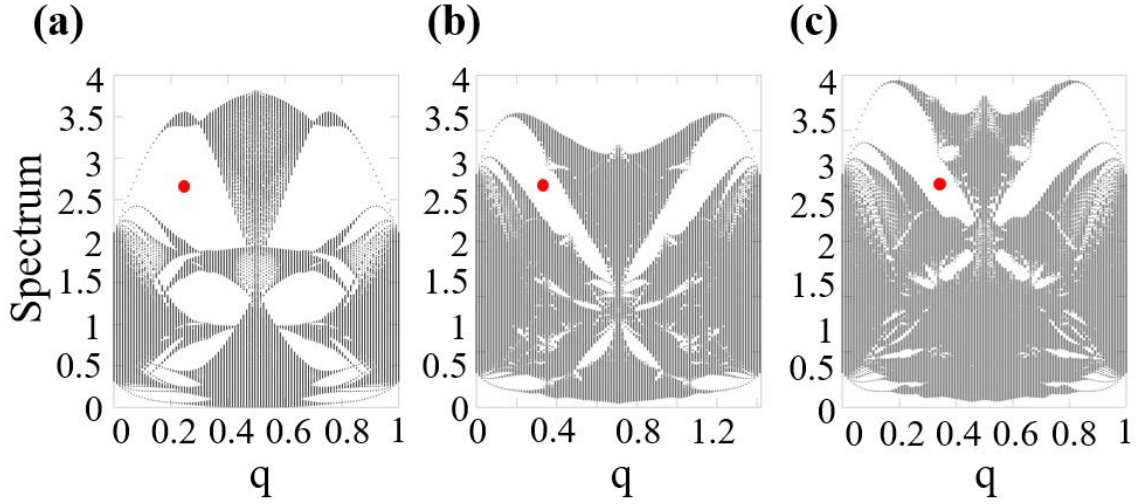


Figure 4.8 Panels (a)-(c) correspond to the patterns in Figure 4.9(a)-(c), respectively. The spectra were computed with the model dynamical matrix $D_{\mathbb{P}} = \sum_{\mathbf{x}, \mathbf{y} \in \mathbb{P}} e^{-1.5|\mathbf{x}-\mathbf{y}|^2} |\mathbf{x}\rangle\langle\mathbf{y}|$, with the distance measured in units of D . The marked spectral gaps are related to bulk spectral gaps mapped in the experiments.

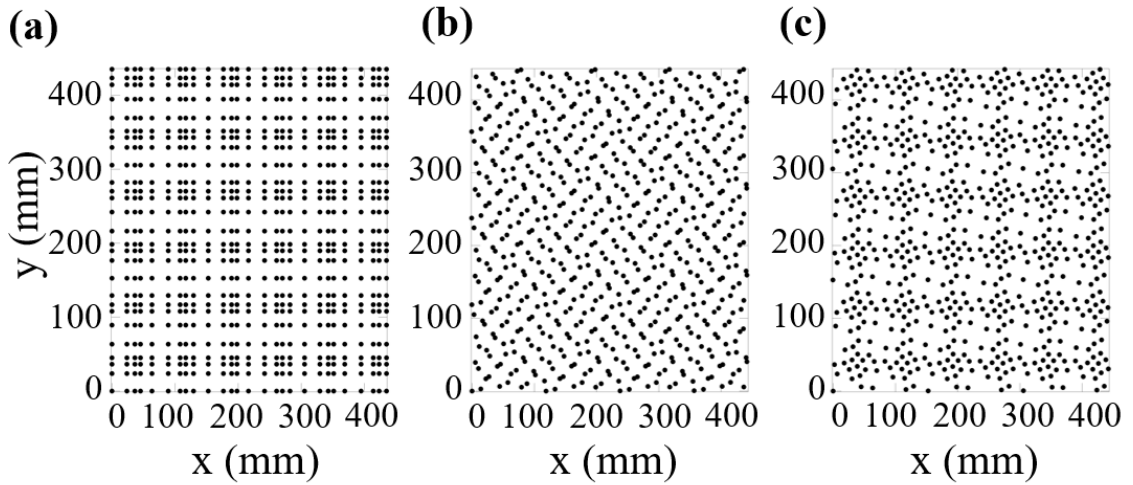


Figure 4.9 Dynamically generated patterns. (a) Same as the pattern of resonators in Figure 4.1 but with the simplified $F(\phi) = \epsilon D(\sin(2\pi\phi_1), \sin(2\pi\phi_2))$. (b) Same as (a) but with the lattice \mathbb{L}' rotated by 45° relative to \mathbb{L} . (c) Same as a but with F replaced by $G \circ F$ with $G(x, y) = (x+y, y-x)$. All three patterns were generated with $\theta = 1/2\sqrt{2}$.

ergodic dynamical system, as the one depicted in Figure 4.1(d). For this, we form the d' -torus $\mathbb{T}^{d'} = \mathbb{R}^{d'} / \mathbb{L}'$ and let the abelian group \mathbb{Z}^d act on it via shifts

$$\tau_{\mathbf{n}}(\phi) = \left(\phi + \sum_{i=1}^d n_i \mathbf{a}_i \right) \bmod \mathbb{L}', \quad \phi \in \mathbb{T}^{d'}, \quad (4.5)$$

exactly as in Figure 4.1(d). Then, if $F :$

$\mathbb{T}^{d'} \rightarrow \mathbb{R}^d$ is any continuous map, such as the projection in Figure 4.1(d), we generate the quasi-periodic pattern $\{\mathbf{p}_{\mathbf{n}}(\phi)\}_{\mathbf{n} \in \mathbb{Z}^d}$ in \mathbb{R}^d using the algorithm

$$\mathbf{p}_{\mathbf{n}}(\phi) = \mathfrak{t}_{\mathbf{n}} \left(\mathbf{p}_0 + F(\tau_{\mathbf{n}}(\phi)) \right), \quad \phi \in \mathbb{T}^{d'}, \quad \mathbf{n} \in \mathbb{Z}^d, \quad (4.6)$$

which is graphically illustrated in Figure 4.1(d). Note, for example, that point $\mathbf{p}_{(1,1)}$ in Figure 4.1(d) can be reached from the origin using many other different paths, such as $(0,0) \mapsto (0,1) \mapsto (1,1)$. For the algorithm to be well defined, all these many different paths must produce the same point $\mathbf{p}_{(1,1)}$. This is indeed ensured by the fact that τ is a group action, that is, $\tau_{\mathbf{n}} \tau_{\mathbf{m}} = \tau_{\mathbf{n}+\mathbf{m}}$. This property is highly non-trivial as, for example, if one chooses to replace the torus with a sphere, then one will find that there are no natural actions of \mathbb{Z}^d on such space, besides the trivial cyclic ones.

The pattern we just designed in the physical space, $\mathbb{P}_{\phi} = \{\mathbf{p}_{\mathbf{n}}(\phi)\}_{\mathbf{n} \in \mathbb{Z}^d}$, depends on the phason ϕ , which marks the point where the algorithm is started. Furthermore, rigid shifts of the pattern result in re-adjustments of the phason, $\mathfrak{t}_{\mathbf{a}}^{-1} \mathbb{P}_{\phi} = \mathbb{P}_{\tau_{\mathbf{a}} \phi}$. Since rigid shifts do not change the resonant spectrum of a crystal, we arrive at the crucial conclusion that the spectrum of the dynamical matrix D_{ϕ} is *independent* of the phason, provided the orbit $\tau_{\mathbf{a}} \phi$ densely fills the d' -torus. As it is well known, this is indeed the case if the lattices \mathbb{L} and \mathbb{L}' are incommensurate. To conclude, we just showed how to engineer a pattern with a phason that lives on a d' -torus. The latter can be used as an adiabatic parameter that keeps

every single bulk spectral gap open, regardless of how the phason is cycled over $\mathbb{T}^{d'}$. This is paramount for the existence and protection of the dispersive boundary modes.

For the acoustic crystal shown in Figure 4.1, the center of the resonators were positioned as in Equation (4.6), with $d = d' = 2$, \mathbf{p}_0 at the lower-left corner and

$$F(\boldsymbol{\phi}) = -\frac{\epsilon D}{2 \sin(\pi\theta)} \left(\cos(2\pi\phi_1 + \pi\theta), \cos(2\pi\phi_2 + \pi\theta) \right), \quad (4.7)$$

where $\boldsymbol{\phi} = \phi_1 \mathbf{a}'_1 + \phi_2 \mathbf{a}'_2$, $\phi_i \in [0, 1]$. Also \mathbb{L} and \mathbb{L}' are square lattices related as $\mathbb{L} = \theta \mathbb{L}'$. The 4D quantum Hall physics, however, can be accessed with any other function F or lattice \mathbb{L}' . Figure 4.9 supplies such examples and, as one can see, the texture of the pattern can change drastically when such adjustments are considered. As we shall see below, as long as a bulk gap remains opened, the topological boundary spectrum shown in Figure 4.1 cannot be removed under smooth deformations of either F or \mathbb{L}' .

4.6 QHE via Phason Engineering

We now demonstrate how the quantum Hall physics emerges in these systems. For mode-to-mode coupling, we can focus on one spectral band at a time, say the k -th one. Then the dynamical matrix corresponding to a generic pattern \mathbb{P} of resonators takes the form

$$D_{\mathbb{P}} = \sum_{\mathbf{m}, \mathbf{n} \in \mathbb{Z}^d} w_{\mathbf{m}, \mathbf{n}}(\mathbb{P}) |\mathbf{m}\rangle \langle \mathbf{n}|, \quad (4.8)$$

where $|\mathbf{n}\rangle$ encodes the k -th discrete resonant mode of the resonator placed at position $\mathbf{p}_{\mathbf{n}}$. As alluded by the notation, the overlap parameters $w_{\mathbf{m}, \mathbf{n}}(\mathbb{P})$ must depend on the pattern in a continuous fashion and they must obey the constraints

$$w_{\mathbf{m}, \mathbf{n}}(\mathbf{t}_{\mathbf{a}}\mathbb{P}) = w_{\mathbf{m}+\mathbf{a}, \mathbf{n}+\mathbf{a}}(\mathbb{P}), \quad \mathbf{a} \in \mathbb{Z}^2. \quad (4.9)$$

It is important to acknowledge that there is no more general expression than (4.8), because \mathbb{P} encodes the entire geometric data of the crystal. Also, Equation (4.9) follows entirely from the Galilean invariance. For our specific patterns, we can pass from \mathbb{P} to ϕ and use Equation 4.9 to reduce

$$D_\phi = \sum_{\mathbf{q}} S_{\mathbf{q}} \left(\sum_{\mathbf{n}} w_{\mathbf{q},\mathbf{0}}(\tau_{\mathbf{n}}(\phi)) |\mathbf{n}\rangle \langle \mathbf{n}| \right), \quad (4.10)$$

where $S_{\mathbf{q}}|\mathbf{n}\rangle = |\mathbf{n} + \mathbf{q}\rangle$ is the shift operator. This shows that any Galilean invariant dynamical matrix over the pattern \mathbb{P}_ϕ is a combination of shift operators and diagonal operators of the form

$$T_f = \sum_{\mathbf{n}} f(\tau_{\mathbf{n}}(\phi)) |\mathbf{n}\rangle \langle \mathbf{n}|, \quad (4.11)$$

for some continuous function f over d' -torus. Furthermore, the following commutation relations are obvious

$$T_f S_{\mathbf{q}} = S_{\mathbf{q}} T_{f \circ \tau_{\mathbf{q}}}, \quad T_f T_g = T_g T_f = T_{f \cdot g}. \quad (4.12)$$

Since every function over a torus can be Fourier decomposed, all T_f 's are linear combinations and powers of d' operators T_j corresponding to the elementary functions

$$u_j(\phi) = e^{i2\pi\phi_j}, \quad \iota = \sqrt{-1}, \quad j = 1, \dots, d', \quad (4.13)$$

where the torus $\mathbb{T}^{d'} = \mathbb{R}^{d'}/\mathbb{L}'$ is parameterized as $\phi = \sum \phi_j \mathbf{a}'_j$, $\phi_j \in [0, 1]$. The conclusion is that any Galilean invariant D_ϕ belongs to the algebra generated by $d' + d$ operators,

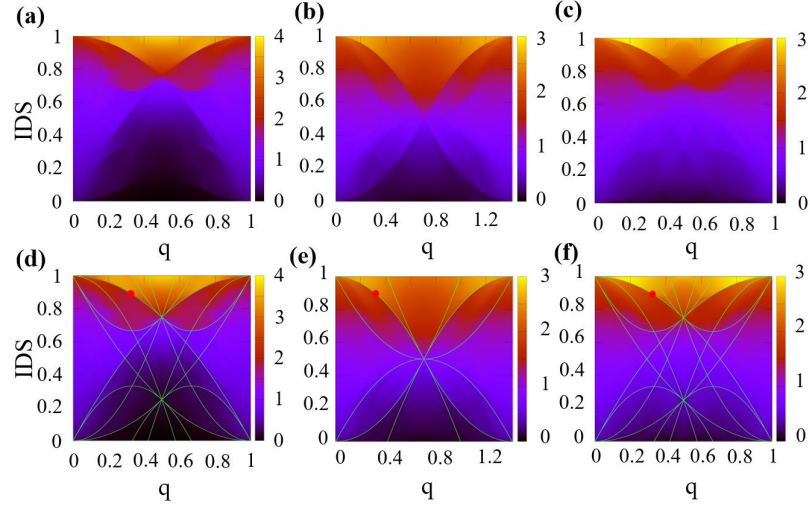


Figure 4.10 Visualizing the topological invariants. **a, b, c** Integrated density of states (IDS) as computed from the spectra in Figure 4.8(a,b,c), respectively. The IDS values inside the spectral gaps can be identified by the abrupt changes in color. **d, e, f** Fittings of the IDS values inside the spectral gaps, seen in panels **a, b, c**, with Equation (4.29). Each curve is determined by the six topological invariants associated to each spectral gaps. The marked curves correspond to the marked gaps in Figure 4.8 and they can be fitted with $1 - \theta^2$, indicating $n_{\{1,2,3,4\}} = -1$, hence a 2nd Chern number -1 .

which are the T_j 's mentioned above together with the elementary shifts $T_{d'+j} = S e_j$, corresponding to the generators e_j of \mathbb{Z}^d . These operators obey the following commutation relations

$$T_i T_j = e^{i2\pi\theta_{ij}} T_j T_i \quad (4.14)$$

with the matrix $\Theta = \{\theta_{ij}\}$ fully determined by the two lattices \mathbb{L} and \mathbb{L}' . Specifically, if A is the transformation matrix, $\mathbf{a}_j = \sum_{i=1}^{d'} A_{ji} \mathbf{a}'_i$, $j = \overline{1, d}$, then

$$\theta_{ij} = -\theta_{ji} = A_{ij}, \quad i = \overline{1, d'}, \quad j = \overline{1, d}, \quad (4.15)$$

and zero for the rest of the indices. In particular, for the acoustic crystal from Figure 4.1, we had $\mathbf{a}_i = \theta \mathbf{a}'_i$, hence $\theta_{13} = -\theta_{31} = \theta_{24} = -\theta_{42} = \theta$. This is also the case for the

pattern **c** from Figure 4.9, but the Θ -matrix for the pattern **b** from Figure 4.9 contain more entries. As a consequence, the non-commutative 4-torus is not just a simple product of two non-commutative 2-tori, as it was the case in the previous experimental works. [Lohse et al., 2018, Zilberberg et al., 2018]

4.7 Visualizing the Topological Invariants

In Figure 4.8, we illustrate the bulk spectrum of the generic dynamical matrix

$$D_{\mathbb{P}} = \sum_{\mathbf{x}, \mathbf{y} \in \mathbb{P}} e^{-1.5|\mathbf{x}-\mathbf{y}|^2} |\mathbf{x}\rangle\langle\mathbf{y}|, \quad (4.16)$$

evaluated on the three patterns shown in Figure 4.9. The fractal nature of the spectra is evident in Figure 4.8. In the Figure 4.2, we demonstrate that model dynamical matrices can indeed reproduce the resonant spectrum of the crystal reported in Figure 4.1. Here, just for illustrative purposes, we chose to work with a model that opens larger gaps. In Figure 4.7, we report the resonant spectrum as computed with open boundary conditions for two shapes, a square and an octagon. Spectral domes can be identified in both cases.

The Chern numbers of the topological bulk gaps can be evaluated directly using existing numerical techniques developed for aperiodic systems. [Prodan, 2017b] However, due to the large number of gaps in Figure 4.8 and to the large number of (strong and weak) topological invariants per gap, an alternative high-throughput method is needed. In fact, the method based on the K-theoretic gap labels [Bellissard, 1986, Bellissard, 1992] explained below enables us to visualize the complete set of invariants associated with a gap. Besides the topological invariants, this method supplies additional predictions that can be tested against the numerical simulations and, as we shall see, this confirms beyond any doubt that the algebra of observables is indeed the non-commutative 4-torus.

In Figure 4.10(a-c), we report the integrated densities of states (IDS) as computed from the spectra Figure 4.8(a-c), respectively, using the usual definition

$$\text{IDS}(E) = \frac{\# \text{ of eigenvalues below } E}{\# \text{ of resonators}}. \quad (4.17)$$

The IDS is plotted as function of θ and energy E , with the latter along the axis coming out of the paper. Since the view point for this graph is from above, we encode the values of the energy in a color map. The abrupt changes in color correspond to the cases when E resides inside the bulk spectral gaps, because in that case the 3-dimensional graph of the IDS shoots straight out of the paper. The striking observation is that these features are not random. Perhaps even more striking is that same patterns are seen if one repeats the calculations with a different dynamical matrix. The reason behind these facts is that the features seen in the IDS plots are not determined by the dynamical matrix but rather by the K-theory of the algebra of observables. Indeed, if P_G represents the gap projection for a gap G , then $\text{IDS}(G)$ can be equivalently computed as the trace per area of P_G , $\text{IDS}(G) = \mathbb{T}(P_G)$. K-theory for operator algebras [Blackadar, 1998] classifies these projections up to stable homotopy and organizes them as an abelian group known as the K_0 -group.

The K_0 -group of complex K -theory of an algebra \mathbb{A} classifies the projections

$$p \in \mathbb{M}_\infty \otimes \mathbb{A}, \quad p^2 = p^* = p, \quad (4.18)$$

with respect to the von Neumann equivalence relation

$$p \sim p' \quad \text{iff} \quad p = vv' \quad \text{and} \quad p' = v'v, \quad (4.19)$$

for some partial isometries v and v' from $\mathbb{M}_\infty \otimes \mathbb{A}$. Above, \mathbb{M} is the algebra of $N \times N$ matrices with complex entries and M_∞ is the direct limit of these algebras. For any projection p from $\mathbb{M}_\infty \otimes \mathbb{A}$, there exists $N \in \mathbb{N}$ such that $p \in \mathbb{M}_N \otimes \mathbb{A}$; hence, we do not really need to work with infinite matrices. However, \mathbb{M}_N can be canonically embedded into \mathbb{M}_∞ and this is convenient, because it enables N to take flexible values.

There are two additional equivalence relations for projections:

- Similarity equivalence:

$$p \sim_u p' \quad \text{iff} \quad p' = upu^* \quad (4.20)$$

for some unitary element u from $\mathbb{M}_\infty \otimes \mathbb{A}$;

- Homotopy equivalence:

$$p \sim_h p' \quad \text{iff} \quad \mathbf{p}(0) = p \quad \text{and} \quad \mathbf{p}(1) = p' \quad (4.21)$$

for some continuous function $\mathbf{p} : [0, 1] \rightarrow \mathbb{M}_\infty \otimes \mathbb{A}$, which always returns a projection.

In general, the three equivalence relations are different, but tensoring \mathbb{A} by \mathbb{M}_∞ makes them entirely equivalent. Note that \sim_h is used in the classification of topological phases of matter.

The equivalence class of a projection p is usually denoted by $[p]_0$, hence $[p]_0$ is the set

$$[p]_0 = \{p' \in \mathbb{M}_\infty \otimes \mathbb{A}, p' \sim p\}. \quad (4.22)$$

If $p \in \mathbb{M}_N \otimes \mathbb{A}$ and $p' \in \mathbb{M}_M \otimes \mathbb{A}$ are two projections, then $\begin{pmatrix} p & 0 \\ 0 & p' \end{pmatrix}$ is a projection from $\mathbb{M}_{N+M} \otimes \mathbb{A}$ and one can define the addition

$$[p]_0 \oplus [p']_0 = \begin{bmatrix} p & 0 \\ 0 & p' \end{bmatrix}_0, \quad (4.23)$$

which provides a semigroup structure on the set of equivalence classes. Then $K_0(\mathbb{A})$ is its enveloping group and, if \mathbb{A} is the non-commutative s -torus,

$$K_0(\mathbb{A}) = \mathbb{Z}^{2^{s-1}}, \quad (4.24)$$

regardless of Θ -matrix. As such, there are 2^{s-1} generators $[e_J]_0$, which can be uniquely labeled by the subsets of indices $J \subseteq \{1, \dots, s\}$ of even cardinality. Throughout, the cardinality of a set will be indicated by $|\cdot|$. Equation (4.24) assures us that, for any projection p from $\mathbb{M}_\infty \otimes \mathbb{A}$, one has

$$[p]_0 = \sum_{J \subseteq \{1, \dots, d\}}^{|J|=\text{even}} n_J [e_J]_0, \quad (4.25)$$

where the coefficients n_J are integer numbers that do not change as long as p is deformed inside its K_0 -class. Specifically, two homotopically equivalent projections will display the same coefficients, hence $\{n_J\}_{|J|=\text{even}}$ represent the *complete* set of topological invariants associated to the projection p . Furthermore, two projections that display the same set of coefficients are necessarily in the same K_0 -class. Let us point out that the coefficient n_J corresponding to $J = \{1, 2, \dots, d\}$ is called the top coefficient and is equal to the strong Chern number associated to the projection p

For the non-commutative s -torus, the K_0 -group is generated by 2^{s-1} projections $[e_J]$, where J is a subset of indices drawn from $\{1, \dots, s\}$ and the cardinal of J is even. Now, the gap projection defines a class inside the K_0 -group and we have the decomposition $[P_G] = \sum_J n_J [e_J]$ into the generators. The integer numbers n_J , known as the gap labels, [Bellissard, 1986, Bellissard, 1992] represent the complete set of topological invariants that can be associated to a gap projection. They are related to the weak and strong Chern numbers.

We will use the uniform notation from [Prodan and Schulz-Baldes, 2016] for the weak and the strong Chern numbers of a gap projection, namely, $\text{Ch}_J(P_G)$, where $J \subset \{1, \dots, d\}$ is a subset of directions. The values of the Chern numbers on the K_0 -generators can be found in [Prodan and Schulz-Baldes, 2016]

$$\text{Ch}_{J'}[e_J]_0 = \begin{cases} 0 & \text{if } J' \not\subseteq J, \\ 1 & \text{if } J' = J, \\ \text{Pf}(\Phi_{J \setminus J'}) & \text{if } J' \subset J, \end{cases} \quad J, J' \subset \{1, \dots, d\}. \quad (4.26)$$

Since the Chern numbers are group homomorphisms between $K_0(\mathbb{A})$ and \mathbb{R} , their values on the gap projection $[P_G]_0 = \sum_J n_J [e_J]_0$ can be straightforwardly computed from (4.26):

$$\text{Ch}_{J'}[P_G]_0 = n_{J'} + \sum_{J' \subsetneq J} n_J \text{Pf}(\Phi_{J \setminus J'}). \quad (4.27)$$

Let us point out that the top Chern number corresponding to $J' = \{1, \dots, d\}$ is always an integer, but the lower Chern numbers may not be.

We established that all Galilean invariant dynamical matrices belong to the non-commutative $(d + d')$ -torus. As such, any gap projection P_G can be decomposed as in Equation (4.25). As such, there are $2^3 = 8$ topological invariants that can be associated

to any spectral gap, of which one is the strong 2nd Chern number, six are proportional to weak 1st Chern numbers, and the remaining one connects to the unit element of the algebra. In particular, $n_{\{1,2,3,4\}}$ equals the 2nd-Chern number. Our task is to extract the gap labels for the patterned acoustic crystals and that information is already contained in Figure 4.10. Indeed,

$$\text{IDS}(G) = \mathbb{T}(P_G) = \sum_J n_J \mathbb{T}(e_J), \quad (4.28)$$

and, by using the value of the trace per area on the generators, we obtain the following prediction for the features seen in Figure 4.10

$$\text{IDS}(G) = \sum_{J \subseteq \{1, \dots, s\}} n_J \text{Pfaffian}(\Theta_J), \quad |J| = \text{even}, \quad (4.29)$$

where Θ_J is the Θ -matrix restricted to the set of indices J . As demonstrated in Figure 4.10(d,e,f), this expression (with $s = d + d'$) fits ALL the features seen in the IDS maps, despite the vast difference between the textures of the corresponding patterns (see Figure 4.9). This serves as our proof that the dynamical matrices for the patterns in Figure 4.9 indeed belong to the non-commutative 4-torus and that we are witnessing the 4D quantum Hall physics.

Using the fittings from Figure 4.10, we were also able to extract the topological invariants associated to the gaps seen in the spectra from Figure 4.8, together with the fitting with the expression derived from the K-theoretic arguments. The IDS inside the spectral gap used in our experiments can be fitted with the curve $1 - \theta^2$. This indicates that $\text{Ch}_2 = -1$ for the spectral gap analyzed experimentally.

4.8 Summary

We found that the boundary physics of aperiodic crystals emulating 4D IQHE is much more interesting and complex than previously believed. While the bulk-boundary correspondence for the virtual higher-dimensional systems is well understood, its manifestation in the lower physical dimensions is not. The phason engineering introduced by our work will be a very effective tool for this research because it supplies a high throughput of topological systems, which is absolutely needed for a systematic investigation of the boundary Weyl physics of these systems. The principles behind the emergence of IQHE in these systems are extremely general and robust, in particular, they do not require fine tuning, hence they can be easily implemented in laboratories or embedded in different applications.

As demonstrated in Figure 4.5, the higher dimensional topological phases supply fundamentally ways of topological wave steering, whose possible applications remain to be discovered. Nevertheless, we already envision radically directions in mode steering, which can be useful for information processing. Indeed, the phason trajectory reported in Figure 4.5 is special in two respects: it has non-trivial topology and it occurs at constant frequency. As such, a coherent drive of the phason along that trajectory will not only steer the mode around the sample, as seen in Figure 4.5, but will also generate temporal de-phasings that can be computed as Berry phases. In fact, the bulk modes can be also manipulated in a similar way, by driving the phason along topologically distinct loops inside the phason space. As already envisioned in [Barlas and Prodan, 2019,] such controlled temporal de-phasings could be used for certain forms of information processing.

We believe that the principles revealed in this work exhaust the many ways one can engineer the phason spaces. They show that, in principle, there is not limit on how high in the virtual dimensions one can go. However, in practice, we expect that the actual laboratory designs to become increasingly challenging and the quality of the topological gaps to wear off as higher virtual dimensions are being conquered. Of course, the next in line is the 6D IQHE, which can be accessed with linear, planar or 3-dimensional meta-material structures.

The latter will require a straightforward generalization of the algorithms used in the present work. Let us recall that the bulk-boundary correspondence principle was worked out in arbitrary dimension in [Prodan and Schulz-Baldes, 2016,] where one can find explicitly solved models as well as an explanation of quantized physical responses.

CHAPTER 5

SUMMARY

In this dissertation, new topological acoustic models have been proposed and analyzed experimentally. Starting from numerical simulations in the field of topological acoustics, we developed principles and protocols for the design and fabrication of quasiperiodic topological acoustic metamaterials. These topological properties originate from the structures solely. Our results can apply to any coupled resonator system regardless of its nature. Following the purpose of this dissertation, we have designed models with different topological properties. These systems either perform functions that have never been achieved before, or greatly improve the performance of existing acoustic metamaterials.

In the main text of this dissertation, I present our contribution to the field of quasiperiodic acoustic metamaterials. Topological properties of quasiperiodic crystals can be characterized by Chern number using K-theory. Having demonstrated these topological acoustic metamaterials, we have laid down a set of specific principles which could facilitate the engineering of these topological effects in many other contexts. First, we describe and design a 1D acoustic waveguide in Chapter 2. The topological gaps can be easily identified when the measured resonant spectrum is mapped as the function of the modulation parameter. Next, we design an incommensurate acoustic bilayer and a new method to transfer energy via a topological pumping process in Chapter 3. We test our predictions for Thouless pumping by sliding the top array of the bilayer whose phason can be driven quickly and periodically in an adiabatic cycle. Finally, we study the higher dimensional topological phases in Chapter 4. We propose a 2D re-configurable quasiperiodic acoustic crystal with 4D quantum Hall effect. We demonstrate that the higher dimensional topological phases supply fundamental methods of topological wave steering, which can be useful for information processing.

These acoustic metamaterials have some common features. First, it has non-trivial topology and the topology arises in these cases related to quasiperiodicity, which can be explained using K-theory. Quasiperiodicity opens topological gaps inside the bands of the periodic structure, which resemble the Hofstadter butterfly when mapped as the function of the modulation parameter. These topological gaps can be characterized by Chern numbers. And the calculated Chern numbers are in agreement with the number of observed topological chiral edge modes. Second, fine-tuning is not necessary in these cases, together with the many different ways of engineering phason spaces, relaxes the design constraints.

Recently, the principle of our 1D quasiperiodic waveguide has been expanded to higher-order acoustic Chern insulator [Chen et al., 2021c] and nonlinear modulated phononic lattices [Rosa et al., 2022]. Experimental studies also demonstrate the feasibility of generating topological edge or interface modes out of patterning in different regimes, such as in elastic beams [Pal et al., 2019], electromechanical waveguides [Xia et al., 2021], and cold atoms chain [Wang and Zhao, 2021]. Inspired by our acoustic Thouless pump, Qidong Fu et al. report that the nonlinear topological pumping of matter waves has been realized in two overlaid optical lattices by moving respect to each other [Fu et al., 2021]. Besides, Non-Abelian Thouless pump has been realized in acoustic waveguide by introducing multi-band non-abelian topology into pumping [You et al., 2021]. Our proposal for 2D reconfigurable acoustic crystal inspires amplitude-induced eigenstate transitions in nonlinear modulated phononic lattices [Rosa et al., 2022]. Furthermore, Similar topological acoustic structure has also been proposed to investigate the sound transport using phason engineering [Chen et al., 2021a].

A few thoughts for improvements of current experimental setups are discussed here. First, the resonators can be fabricated using metals for achieving higher Q factors. In higher dimensional topological systems, the topological gaps are relatively narrow. Therefore, it is necessary to increase the Q factor of the system to measure related topological phenomena. Second, the concept of synthetic couplings inspires us to adjust the coupling by conversion

between sound and electricity for reversible and real-time control of topological phases and topological transitions rather than rearrange the positions of the resonators. The measurement time can be greatly shortened, and dynamic topological phenomena such as topological braiding can be realized. A recent and interesting study has shown adiabatic modulation of hopping coefficient by continuously varying the position of the air sheets which connects the top or middle or bottom waveguides as a promising and effective way of achieving non-Abelian topological braiding of acoustic modes [Chen et al., 2021b].

To date, we mainly investigate QHE in 1D and 2D topological acoustic systems. The realization of higher order topological metamaterials, which are more complex but appealing, still remains challenging. Essentially, the quasiperiodic patterings provide synthetic dimensions, and acoustic resonators can be coupled horizontally and vertically, it is still difficult for us to fully realize the 6D QHE in 3D quasiperiodic system in a short time. Fortunately, there have been a few recent theoretical studies in other regime that we can learn and use for reference, such as electromagnetic response in 6D quantum Hall system, which potentially can be realized in 3D experimental setups [Lee et al., 2018]. Future work could be also aimed at addressing nonlinear properties of acoustic metamaterials. The combination of nonlinearities and geometrical asymmetries breaks reciprocity and enables unidirectional sound transport along the boundaries [Hadad et al., 2018].

Our results are also benefiting a broad range of applications, including noise control, information transfer, acoustic-based sensing and imaging, and quantum information. We have offered a new way of the implementation and observation of topological excitation modes originating solely from the structure of the materials, which may offer opportunities in topological acoustics to manipulate and control sound in fundamentally new ways. We hope our efforts would inspire others to design more fascinating topological metamaterials based on the same principles. This emerging area of research takes inspiration from groundbreaking advances in condensed matter physics, quantum mechanics, and mathematics and leverages the properties of acoustic metamaterials to enable new forms of

sound transport. We expect the field of topological acoustics to open disruptive directions for sound control, with an impact on basic science and applied technologies.

REFERENCES

- [Al Jahdali and Wu, 2016] Al Jahdali, R. and Wu, Y. (2016). High transmission acoustic focusing by impedance-matched acoustic meta-surfaces. *Applied Physics Letters*, 108(3):031902.
- [Apigo et al., 2019] Apigo, D. J., Cheng, W., Dobiszewski, K. F., Prodan, E., and Prodan, C. (2019). Observation of topological edge modes in a quasiperiodic acoustic waveguide. *Physical Review Letters*, 122(9):095501.
- [Apigo et al., 2018] Apigo, D. J., Qian, K., Prodan, C., and Prodan, E. (2018). Topological edge modes by smart patterning. *Physical Review Materials*, 2(12):124203.
- [Aubry and André, 1980] Aubry, S. and André, G. (1980). Analyticity breaking and anderson localization in incommensurate lattices. *Ann. Israel Phys. Soc*, 3(133):18.
- [Baboux et al., 2017] Baboux, F., Levy, E., Lemaître, A., Gómez, C., Galopin, E., Le Gratiet, L., Sagnes, I., Amo, A., Bloch, J., and Akkermans, E. (2017). Measuring topological invariants from generalized edge states in polaritonic quasicrystals. *Physical Review B*, 95(16):161114.
- [Barlas and Prodan, 2019] Barlas, Y. and Prodan, E. (2019). Topological braiding of majorana-like modes in classical meta-materials. *Preprint at <https://arxiv.org/abs/1903.00463>*.
- [Bellissard, 1986] Bellissard, J. (1986). K-theory of c*-algebras in solid state physics. In *Statistical mechanics and field theory: mathematical aspects*, pages 99–156. Heidelberg, Berlin, Springer.
- [Bellissard, 1992] Bellissard, J. (1992). Gap labelling theorems for schrödinger operators. In *From number theory to physics*, pages 538–630. Heidelberg, Berlin, Springer.
- [Bernevig, 2013] Bernevig, B. A. (2013). *Topological insulators and topological superconductors*. Princeton, NJ, Princeton university press.
- [Birkhoff, 1931] Birkhoff, G. D. (1931). Proof of the ergodic theorem. *Proceedings of the National Academy of Sciences*, 17(12):656–660.
- [Blackadar, 1998] Blackadar, B. (1998). *K-theory for operator algebras*, volume 5. Cambridge, England, Cambridge University Press.
- [Bourne and Prodan, 2018] Bourne, C. and Prodan, E. (2018). Non-commutative chern numbers for generic aperiodic discrete systems. *Journal of Physics A: Mathematical and Theoretical*, 51(23):235202.

- [Bourne and Rennie, 2018] Bourne, C. and Rennie, A. (2018). Chern numbers, localisation and the bulk-edge correspondence for continuous models of topological phases. *Mathematical Physics, Analysis and Geometry*, 21(3):1–62.
- [Chang et al., 2013a] Chang, C.-Z., Zhang, J., Feng, X., Shen, J., Zhang, Z., Guo, M., Li, K., Ou, Y., Wei, P., Wang, L.-L., et al. (2013a). Experimental observation of the quantum anomalous hall effect in a magnetic topological insulator. *Science*, 340(6129):167–170.
- [Chang et al., 2013b] Chang, C.-Z., Zhang, J., Liu, M., Zhang, Z., Feng, X., Li, K., Wang, L.-L., Chen, X., Dai, X., Fang, Z., et al. (2013b). Thin films of magnetically doped topological insulator with carrier-independent long-range ferromagnetic order. *Advanced Materials*, 25(7):1065–1070.
- [Chaunsali et al., 2018] Chaunsali, R., Chen, C.-W., and Yang, J. (2018). Subwavelength and directional control of flexural waves in zone-folding induced topological plates. *Physical Review B*, 97(5):054307.
- [Chen et al., 2018] Chen, H., Nassar, H., and Huang, G. (2018). Topological mechanics of edge waves in kagome lattices. *arXiv preprint arXiv:1802.04404*.
- [Chen et al., 2021a] Chen, H., Zhang, H., Wu, Q., Huang, Y., Nguyen, H., Prodan, E., Zhou, X., and Huang, G. (2021a). Creating synthetic spaces for higher-order topological sound transport. *Nature Communications*, 12(1):1–10.
- [Chen et al., 2021b] Chen, Z.-G., Zhang, R.-Y., Chan, C., and Ma, G. (2021b). Classical non-abelian braiding of acoustic modes. *Nature Physics*, pages 1–6.
- [Chen et al., 2021c] Chen, Z.-G., Zhu, W., Tan, Y., Wang, L., and Ma, G. (2021c). Acoustic realization of a four-dimensional higher-order chern insulator and boundary-modes engineering. *Physical Review X*, 11(1):011016.
- [Fu et al., 2021] Fu, Q., Wang, P., Kartashov, Y. V., Konotop, V. V., and Ye, F. (2021). Nonlinear thouless pumping: solitons and transport breakdown. *arXiv preprint arXiv:2110.14472*.
- [Grinberg et al., 2020] Grinberg, I. H., Lin, M., Harris, C., Benalcazar, W. A., Peterson, C. W., Hughes, T. L., and Bahl, G. (2020). Robust temporal pumping in a magneto-mechanical topological insulator. *Nature Communications*, 11(1):1–9.
- [Hadad et al., 2018] Hadad, Y., Soric, J. C., Khanikaev, A. B., and Alu, A. (2018). Self-induced topological protection in nonlinear circuit arrays. *Nature Electronics*, 1(3):178–182.
- [Hafezi et al., 2013] Hafezi, M., Mittal, S., Fan, J., Migdall, A., and Taylor, J. (2013). Imaging topological edge states in silicon photonics. *Nature Photonics*, 7(12):1001–1005.

- [Haldane and Raghu, 2008] Haldane, F. and Raghu, S. (2008). Possible realization of directional optical waveguides in photonic crystals with broken time-reversal symmetry. *Physical Review Letters*, 100(1):013904.
- [Haldane, 1988] Haldane, F. D. M. (1988). Model for a quantum hall effect without landau levels: Condensed-matter realization of the " parity anomaly". *Physical Review Letters*, 61(18):2015.
- [Harper, 1955] Harper, P. G. (1955). Single band motion of conduction electrons in a uniform magnetic field. *Proceedings of the Physical Society. Section A*, 68(10):874.
- [He et al., 2016] He, C., Ni, X., Ge, H., Sun, X.-C., Chen, Y.-B., Lu, M.-H., Liu, X.-P., and Chen, Y.-F. (2016). Acoustic topological insulator and robust one-way sound transport. *Nature Physics*, 12(12):1124–1129.
- [Hofstadter, 1976] Hofstadter, D. R. (1976). Energy levels and wave functions of bloch electrons in rational and irrational magnetic fields. *Physical Review B*, 14(6):2239.
- [Kane and Lubensky, 2014] Kane, C. and Lubensky, T. (2014). Topological boundary modes in isostatic lattices. *Nature Physics*, 10(1):39–45.
- [Kellendonk et al., 2002] Kellendonk, J., Richter, T., and Schulz-Baldes, H. (2002). Edge current channels and chern numbers in the integer quantum hall effect. *Reviews in Mathematical Physics*, 14(01):87–119.
- [Kitaev, 2009] Kitaev, A. (2009). Periodic table for topological insulators and superconductors. *American Institute of Physics Conference Proceedings*, 1134(1):22–30.
- [Kraus et al., 2012] Kraus, Y. E., Lahini, Y., Ringel, Z., Verbin, M., and Zilberberg, O. (2012). Topological states and adiabatic pumping in quasicrystals. *Physical Review Letters*, 109(10):106402.
- [Lee et al., 2018] Lee, C. H., Wang, Y., Chen, Y., and Zhang, X. (2018). Electromagnetic response of quantum hall systems in dimensions five and six and beyond. *Physical Review B*, 98(9):094434.
- [Liang et al., 2009] Liang, B., Yuan, B., and Cheng, J.-c. (2009). Acoustic diode: rectification of acoustic energy flux in one-dimensional systems. *Physical Review Letters*, 103(10):104301.
- [Lohse et al., 2018] Lohse, M., Schweizer, C., Price, H. M., Zilberberg, O., and Bloch, I. (2018). Exploring 4d quantum hall physics with a 2d topological charge pump. *Nature*, 553(7686):55–58.
- [Lohse et al., 2016] Lohse, M., Schweizer, C., Zilberberg, O., Aidelsburger, M., and Bloch, I. (2016). A thouless quantum pump with ultracold bosonic atoms in an optical superlattice. *Nature Physics*, 12(4):350–354.

- [Lustig et al., 2019] Lustig, E., Weimann, S., Plotnik, Y., Lumer, Y., Bandres, M. A., Szameit, A., and Segev, M. (2019). Photonic topological insulator in synthetic dimensions. *Nature*, 567(7748):356–360.
- [Miniaci et al., 2017] Miniaci, M., Pal, R., Morvan, B., and Ruzzene, M. (2017). Observation of topologically protected helical edge modes in kagome elastic plates. *arXiv preprint arXiv:1710.11556*.
- [Mousavi et al., 2015] Mousavi, S. H., Khanikaev, A. B., and Wang, Z. (2015). Topologically protected elastic waves in phononic metamaterials. *Nature Communications*, 6(1):1–7.
- [Nakajima et al., 2016] Nakajima, S., Tomita, T., Taie, S., Ichinose, T., Ozawa, H., Wang, L., Troyer, M., and Takahashi, Y. (2016). Topological Thouless pumping of ultracold fermions. *Nature Physics*, 12(4):296–300.
- [Nash et al., 2015] Nash, L. M., Kleckner, D., Read, A., Vitelli, V., Turner, A. M., and Irvine, W. T. (2015). Topological mechanics of gyroscopic metamaterials. *Proceedings of the National Academy of Sciences*, 112(47):14495–14500.
- [Ni et al., 2019] Ni, X., Chen, K., Weiner, M., Apigo, D. J., Prodan, C., Alù, A., Prodan, E., and Khanikaev, A. B. (2019). Observation of Hofstadter butterfly and topological edge states in reconfigurable quasi-periodic acoustic crystals. *Communications Physics*, 2(1):1–7.
- [Ni et al., 2018] Ni, X., Weiner, M., Alù, A., and Khanikaev, A. B. (2018). Observation of bulk polarization transitions and higher-order embedded topological eigenstates for sound. *arXiv preprint arXiv:1807.00896*.
- [Pal et al., 2019] Pal, R. K., Rosa, M. I., and Ruzzene, M. (2019). Topological bands and localized vibration modes in quasiperiodic beams. *New Journal of Physics*, 21(9):093017.
- [Pal et al., 2016] Pal, R. K., Schaeffer, M., and Ruzzene, M. (2016). Helical edge states and topological phase transitions in phononic systems using bi-layered lattices. *Journal of Applied Physics*, 119(8):084305.
- [Paulose et al., 2015] Paulose, J., Chen, B. G.-g., and Vitelli, V. (2015). Topological modes bound to dislocations in mechanical metamaterials. *Nature Physics*, 11(2):153–156.
- [Petrides and Zilberberg, 2020] Petrides, I. and Zilberberg, O. (2020). Higher-order topological insulators, topological pumps and the quantum hall effect in high dimensions. *Physical Review Research*, 2(2):022049.
- [Price et al., 2015] Price, H. M., Zilberberg, O., Ozawa, T., Carusotto, I., and Goldman, N. (2015). Four-dimensional quantum hall effect with ultracold atoms. *Physical Review Letters*, 115(19):195303.

- [Prodan, 2015] Prodan, E. (2015). Virtual topological insulators with real quantized physics. *Physical Review B*, 91(24):245104.
- [Prodan, 2017a] Prodan, E. (2017a). *A computational non-commutative geometry program for disordered topological insulators*, volume 23. Heidelberg, Berlin, Springer.
- [Prodan, 2017b] Prodan, E. (2017b). Disordered topological insulators: A brief introduction. In *A Computational Non-commutative Geometry Program for Disordered Topological Insulators*, pages 1–9. Heidelberg, Berlin, Springer.
- [Prodan et al., 2017] Prodan, E., Dobiszewski, K., Kanwal, A., Palmieri, J., and Prodan, C. (2017). Dynamical majorana edge modes in a broad class of topological mechanical systems. *Nature Communications*, 8(1):1–7.
- [Prodan and Prodan, 2009] Prodan, E. and Prodan, C. (2009). Topological phonon modes and their role in dynamic instability of microtubules. *Physical Review Letters*, 103(24):248101.
- [Prodan and Schulz-Baldes, 2016] Prodan, E. and Schulz-Baldes, H. (2016). Bulk and boundary invariants for complex topological insulators. Heidelberg, Berlin, Springer.
- [Prodan and Shmalo, 2019] Prodan, E. and Shmalo, Y. (2019). The k-theoretic bulk-boundary principle for dynamically patterned resonators. *Journal of Geometry and Physics*, 135:135–171.
- [Qi et al., 2008] Qi, X.-L., Hughes, T. L., and Zhang, S.-C. (2008). Topological field theory of time-reversal invariant insulators. *Physical Review B*, 78(19):195424.
- [Qi and Zhang, 2011] Qi, X.-L. and Zhang, S.-C. (2011). Topological insulators and superconductors. *Reviews of Modern Physics*, 83(4):1057.
- [Rice and Mele, 1982] Rice, M. and Mele, E. (1982). Elementary excitations of a linearly conjugated diatomic polymer. *Physical Review Letters*, 49(19):1455.
- [Richoux and Pagneux, 2002] Richoux, O. and Pagneux, V. (2002). Acoustic characterization of the hofstadter butterfly with resonant scatterers. *EPL (Europhysics Letters)*, 59(1):34.
- [Riva et al., 2020] Riva, E., Rosa, M. I., and Ruzzene, M. (2020). Edge states and topological pumping in stiffness-modulated elastic plates. *Physical Review B*, 101(9):094307.
- [Rosa et al., 2022] Rosa, M. I., Leamy, M. J., and Ruzzene, M. (2022). Amplitude-dependent edge states and discrete breathers in nonlinear modulated phononic lattices. *arXiv preprint arXiv:2201.05526*.
- [Rosa et al., 2019] Rosa, M. I., Pal, R. K., Arruda, J. R., and Ruzzene, M. (2019). Edge states and topological pumping in spatially modulated elastic lattices. *Physical Review Letters*, 123(3):034301.

- [Ryu et al., 2010] Ryu, S., Schnyder, A. P., Furusaki, A., and Ludwig, A. W. (2010). Topological insulators and superconductors: tenfold way and dimensional hierarchy. *New Journal of Physics*, 12(6):065010.
- [Schnyder et al., 2008] Schnyder, A. P., Ryu, S., Furusaki, A., and Ludwig, A. W. (2008). Classification of topological insulators and superconductors in three spatial dimensions. *Physical Review B*, 78(19):195125.
- [Shen et al., 2019] Shen, Y.-X., Peng, Y.-G., Zhao, D.-G., Chen, X.-C., Zhu, J., and Zhu, X.-F. (2019). One-way localized adiabatic passage in an acoustic system. *Physical Review Letters*, 122(9):094501.
- [Shi et al., 2009] Shi, J., Ahmed, D., Mao, X., Lin, S.-C. S., Lawit, A., and Huang, T. J. (2009). Acoustic tweezers: patterning cells and microparticles using standing surface acoustic waves (ssaw). *Lab on a Chip*, 9(20):2890–2895.
- [Slobozhanyuk et al., 2017] Slobozhanyuk, A., Mousavi, S. H., Ni, X., Smirnova, D., Kivshar, Y. S., and Khanikaev, A. B. (2017). Three-dimensional all-dielectric photonic topological insulator. *Nature Photonics*, 11(2):130–136.
- [Süsstrunk and Huber, 2015] Süsstrunk, R. and Huber, S. D. (2015). Observation of phononic helical edge states in a mechanical topological insulator. *Science*, 349(6243):47–50.
- [Thouless, 1983] Thouless, D. (1983). Quantization of particle transport. *Physical Review B*, 27(10):6083.
- [Thouless et al., 1982] Thouless, D. J., Kohmoto, M., Nightingale, M. P., and den Nijs, M. (1982). Quantized hall conductance in a two-dimensional periodic potential. *Physical Review Letters*, 49(6):405.
- [Verbin et al., 2013] Verbin, M., Zilberberg, O., Kraus, Y. E., Lahini, Y., and Silberberg, Y. (2013). Observation of topological phase transitions in photonic quasicrystals. *Physical Review Letters*, 110(7):076403.
- [Verbin et al., 2015] Verbin, M., Zilberberg, O., Lahini, Y., Kraus, Y. E., and Silberberg, Y. (2015). Topological pumping over a photonic fibonacci quasicrystal. *Physical Review B*, 91(6):064201.
- [Voss and Ballon, 2020] Voss, H. U. and Ballon, D. J. (2020). Topological modes in radiofrequency resonator arrays. *Physics Letters A*, 384(8):126177.
- [Wang and Zhao, 2021] Wang, B. and Zhao, C. (2021). Topological quantum optical states in quasiperiodic cold atomic chains. *Physical Review A*, 103(1):013727.
- [Wang et al., 2015] Wang, P., Lu, L., and Bertoldi, K. (2015). Topological phononic crystals with one-way elastic edge waves. *Physical Review Letters*, 115(10):104302.
- [Wang et al., 2020] Wang, Y., Price, H. M., Zhang, B., and Chong, Y. (2020). Circuit implementation of a four-dimensional topological insulator. *Nature Communications*, 11(1):1–7.

- [Wang et al., 2009] Wang, Z., Chong, Y., Joannopoulos, J. D., and Soljačić, M. (2009). Observation of unidirectional backscattering-immune topological electromagnetic states. *Nature*, 461(7265):772–775.
- [Wu and Hu, 2015] Wu, L.-H. and Hu, X. (2015). Scheme for achieving a topological photonic crystal by using dielectric material. *Physical Review Letters*, 114(22):223901.
- [Xia et al., 2020] Xia, Y., Erturk, A., and Ruzzene, M. (2020). Topological edge states in quasiperiodic locally resonant metastructures. *Physical Review Applied*, 13(1):014023.
- [Xia et al., 2021] Xia, Y., Riva, E., Rosa, M. I., Cazzulani, G., Erturk, A., Braghin, F., and Ruzzene, M. (2021). Experimental observation of temporal pumping in electromechanical waveguides. *Physical Review Letters*, 126(9):095501.
- [Xiao et al., 2010] Xiao, D., Chang, M.-C., and Niu, Q. (2010). Berry phase effects on electronic properties. *Reviews of Modern Physics*, 82(3):1959.
- [Xiao et al., 2015] Xiao, M., Ma, G., Yang, Z., Sheng, P., Zhang, Z., and Chan, C. T. (2015). Geometric phase and band inversion in periodic acoustic systems. *Nature Physics*, 11(3):240–244.
- [Yang et al., 2017] Yang, M., Chen, S., Fu, C., and Sheng, P. (2017). Optimal sound-absorbing structures. *Materials Horizons*, 4(4):673–680.
- [Yang et al., 2015] Yang, Z., Gao, F., Shi, X., Lin, X., Gao, Z., Chong, Y., and Zhang, B. (2015). Topological acoustics. *Physical Review Letters*, 114(11):114301.
- [You et al., 2021] You, O., Liang, S., Xie, B., Gao, W., Ye, W., Zhu, J., and Zhang, S. (2021). Observation of non-abelian thouless pump. *arXiv preprint arXiv:2110.08789*.
- [Zhang and Hu, 2001] Zhang, S.-C. and Hu, J. (2001). A four-dimensional generalization of the quantum hall effect. *Science*, 294(5543):823–828.
- [Zhu et al., 2011] Zhu, J., Christensen, J., Jung, J., Martin-Moreno, L., Yin, X., Fok, L., Zhang, X., and Garcia-Vidal, F. (2011). A holey-structured metamaterial for acoustic deep-subwavelength imaging. *Nature Physics*, 7(1):52–55.
- [Zilberberg et al., 2017] Zilberberg, O., Huang, S., Guglielmon, J., Wang, M., Chen, K., Kraus, Y. E., and Rechtsman, M. C. (2017). Photonic topological pumping through the edges of a dynamical four-dimensional quantum hall system. *arXiv preprint arXiv:1705.08361*.
- [Zilberberg et al., 2018] Zilberberg, O., Huang, S., Guglielmon, J., Wang, M., Chen, K. P., Kraus, Y. E., and Rechtsman, M. C. (2018). Photonic topological boundary pumping as a probe of 4d quantum hall physics. *Nature*, 553(7686):59–62.